SERDP

FINAL REPORT

Bistatic Acoustic Scattering from Munitions: Interactions with Nearby Clutter and the Water-Sediment Interface

Steven Kargl
Aubrey Espana
Applied Physics Laboratory, University of Washington

August 2023

SERDP Project MR19-1234

REPORT DOCUMENTATION PAGE

Form Approved
OMB No. 0704-0188

1. REPORT DATE *(DD-MM-YYYY)*	2. REPORT TYPE	3. DATES COVERED *(From - To)*
21/08/2023	SERDP Final Report	8/19/2019 - 8/19/2023

4. TITLE AND SUBTITLE

Bistatic Acoustic Scattering from Munitions: Interactions with Nearby Clutter and the Water-Sediment Interface

5a. CONTRACT NUMBER
19-C-0058

5b. GRANT NUMBER

5c. PROGRAM ELEMENT NUMBER

6. AUTHOR(S)
Steven Kargl
Aubrey Espana

5d. PROJECT NUMBER
MR19-1234

5e. TASK NUMBER

5f. WORK UNIT NUMBER

7. PERFORMING ORGANIZATION NAME(S) AND ADDRESS(ES)
Applied Physics Laboratory, University of Washington
1013 NE 40th St
Seattle, WA 98105-6698

8. PERFORMING ORGANIZATION REPORT NUMBER
MR19-1234

9. SPONSORING/MONITORING AGENCY NAME(S) AND ADDRESS(ES)
Office of the Deputy Assistant Secretary of Defense (Energy Resilience & Optimization)
3500 Defense Pentagon, RM 5C646
Washington, DC 20301-3500

10. SPONSOR/MONITOR'S ACRONYM(S)
SERDP

11. SPONSOR/MONITOR'S REPORT NUMBER(S)
MR19-1234

12. DISTRIBUTION/AVAILABILITY STATEMENT
DISTRIBUTION STATEMENT A. Approved for public release: distribution unlimited.

13. SUPPLEMENTARY NOTES

14. ABSTRACT

SERDP MR19-1234 investigated a number of issues with simulations of the acoustic scattering from objects near the water-sediment interface. The initial effort focused on three primary objectives of bistatic scattering, multiple scattering between an object-of-interest and nearby clutter, and simulations for the Multi-Sensor Towbody (MuST) that is being developed under ESTCP MR18-5004. First, full bistatic acoustic scattering capabilities were developed within the Target-in-the-Environment Response model (TIER) framework. Sonar platforms under development for underwater munitions remediation have relatively large spatial separation between acoustic sources and receiving-array elements in comparison to the expected stand-off distances to an object. Second, when a munition is in close proximity to another object (e.g., another munition, scuba tank, boat anchor, ...), the acoustic scattering from the munition and object can interact. The interaction yields a complicate, composite target signature. Second- through fourth-order multiple scattering was integrated into the TIER model. Multiple scattering is inherently a bistatic scattering geometry, so progress on the first objective is a requirement. Third, the TIER model with these new capabilities is used in the generation of simulated data for ESTCP MR18-5004 to aid in the development of detection, classification, and geolocation algorithms. In addition to the first two primary objectives, a few limitations in the TIER model were addressed. These include integration of frequency-dependent beam patterns for a source or receiver, a variable sound speed profile in the water column, and partial/full burial model refinements. Finally, acoustic scattering from lightweight lines used in deployment and recovery of objects in a test bed was investigated in collaboration with SERDP MR21-7211.

15. SUBJECT TERMS
underwater ,unitions, acoustic response, UXO detection and characterization, UXO, bistatic scattering, multiple scattering

16. SECURITY CLASSIFICATION OF:			17. LIMITATION OF ABSTRACT	18. NUMBER OF PAGES	19a. NAME OF RESPONSIBLE PERSON
a. REPORT	b. ABSTRACT	c. THIS PAGE			Steven Kargl
UNCLASS	UNCLASS	UNCLASS	UNCLASS	65	19b. TELEPHONE NUMBER *(Include area code)* 206-685-4677

Contents

List of Figures

List of Tables

Acronyms

AC ..... Acoustic color
APL-UW ..... Applied Physics Laboratory, University of Washington
ARL-PSU ..... Applied Research Laboratory, Pennsylvania State University
BAYEX14 ..... Bay Experiment 2014
BSA ..... Bistatic scattering amplitude
CLUTTEREX17 ..... Clutter Experiment 2017
CTD ..... Conductivity, Temperature, and Depth
DoD ..... Department of Defense
FE ..... Finite-element
HF ..... High frequency
LF ..... Low frequency
LFM ..... Linear-frequency-modulated
MIP ..... Maximum intensity projection
MSA ..... Monostatic scattering amplitude
MuST ..... Multi-Sensor Towbody
NSWC PCD ..... Naval Surface Warfare Center, Panama City Division
ONR ..... Office of Naval Research
PC ..... Pulse-compressed
PONDEX08 ..... Pond Experiment 2008
PONDEX09 ..... Pond Experiment 2009
PONDEX10 ..... Pond Experiment 2010
SAS ..... Synthetic aperture sonar
SNR ..... Signal-to-noise ratio
SSP ..... Sound speed profile
TIER ..... Target-in-the-environment-response
TREX13 ..... Target and Reverberation Experiment 2013
TS ..... Target strength
UXO ..... Unexploded ordnance

Abstract

SERDP MR19-1234 investigated a number of issues with simulations of the acoustic scattering from objects near the water-sediment interface. The initial effort focused on three primary objectives of bistatic scattering, multiple scattering between an object-of-interest and nearby clutter, and simulations for the Multi-Sensor Towbody (MuST) that is being developed under ESTCP MR18-5004. First, full bistatic acoustic scattering capabilities were developed within the Target-in-the-Environment Response model (TIER) framework. Sonar platforms under development for underwater munitions remediation have relatively large spatial separation between acoustic sources and receiving-array elements in comparison to the expected stand-off distances to an object. Second, when a munition is in close proximity to another object (e.g., another munition, scuba tank, boat anchor, ...), the acoustic scattering from the munition and object can interact. The interaction yields a complicate, composite target signature. Second- through fourth-order multiple scattering was integrated into the TIER model. Multiple scattering is inherently a bistatic scattering geometry, so progress on the first objective is a requirement. Third, the TIER model with these new capabilities is used in the generation of simulated data for ESTCP MR18-5004 to aid in the development of detection, classification, and geolocation algorithms. In addition to the first two primary objectives, a few limitations in the TIER model were addressed. These include integration of frequency-dependent beam patterns for a source or receiver, a variable sound speed profile in the water column, and partial/full burial model refinements. Finally, acoustic scattering from lightweight lines used in deployment and recovery of objects in a test bed was investigated in collaboration with SERDP MR21-7211.

1 Introduction

The Applied Physics Laboratory, University of Washington (APL-UW) has a long history in both experimental and theoretical research in acoustic scattering from an object near a water-sediment interface. As a part of this research, the Target-in-the-Environment Response (TIER) model was developed to simulate low-frequency (LF) broadband sonar. Our initial effort considered a single inert unexploded ordnance (UXO) or short, solid aluminum cylinder (2 ft length and 1 ft diameter) in controlled pond experiments (PONDEX8, PONDEX9, PONDEX10) and in our modeling efforts [1]. Today, the set of objects has expanded to include several inert UXO (i.e., 82-mm, 100-mm, 105-mm, and 155-mm shells), scientific objects (i.e., spheres, cylinders, open-ended pipes), and clutter items (i.e., small boat anchors, scuba tanks, crab and lobster traps). Rail-based measurements were performed not only in a pond at the Naval Surface Warfare Center, Panama City Division (NSWC PCD), but the rail system was also deployed in the Gulf of Mexico (TREX13 and CLUTTEREX17) and the brackish environment of St. Andrew Bay. These at-sea measurements were conducted in collaboration with NSWC PCD and leveraged cost-sharing with ONR-funded research. Lastly, APL-UW has transitioned from rail-based measurements to an applied system (i.e., the MuST) under ESTCP MR18-5004.

Prior to SERDP MR19-1234, the TIER model contained the following simplifying assumptions:

- Source and receiver are co-located (i.e., a monostatic scattering geometry). That is, the separation distance between source and receiver is small in comparison to the stand-off distance to an object.
- Objects are isolated. Sound scattered by an object does not interact with neighboring objects.
- Objects are axisymmetric with their axis of symmetry parallel to the water-sediment interface.
- Water column is a homogeneous fluid layer bounded above by air and below by a homogeneous sediment.

Relaxation or removal of these assumptions from the TIER model was motivated by a need to model sonar platforms currently being developed for munition remediation activities. These platforms often deploy downward-looking sonars, and can realize relatively short stand-off distances to the water-sediment interface and to objects near this interface.

The remainder of this report discusses our progress with removing assumptions and limitations of the TIER model. Section 2 provides an overview of the underlying environments in the TIER model at the onset of SERDP MR19-1234. One of the more challenging objectives was removal of the monostatic scattering assumption, which entailed a generalization of tabulated scattering amplitudes for various objects. Full bistatic scattering is discussed in Sec. 3. CLUTTEREX17 collected at-sea data from objects where the separation distance between adjacent objects was on the order of 1 m, which allowed for an interaction of the acoustic scattering with neighboring objects. Synthetic aperture sonar (SAS) images and acoustic color (AC) templates, produced from this data, exhibited structure that could not be associated with a specific object. Thus, the TIER model was modified to include second-order through fourth-order multiple scattering to investigate a possible origin for the observables. This work is documented in Sec. 4, where it is noted that

multiple scattering is an inherently bistatic scattering phenomenon. Section 5 discusses our effort to relax an assumption of a homogeneous fluid environment (i.e., sound propagates along straight lines). Here, the well-known BELLHOP ray-tracing model for propagation in a stratified environment [2] has been integrated within the TIER model. The TIER model includes neither passive noise (e.g., breaking waves or nearby ships) nor active noise (e.g., scattering of a transmitted sonar signal from a rough sea floor or sea surface). Scattering of sound from a rough sea floor is described in Sec. 6. This then allows injection of some realistic noise into simulations. The penultimate Sec. 7 recaps a task that was added to SERDP MR19-1234, which conducted acoustic scattering experiments from guide lines often used in deployment and recovery of at-sea test beds. The final section concludes with general remarks.

2 TIER Model Framework

The TIER model framework employs a global coordinate system to describe a scene, which is composed from an environment and one or more objects placed within that environment. The location of a source, receiver, and an object are $\boldsymbol{r}_s$, $\boldsymbol{r}_r$, and $\boldsymbol{r}_t$, respectively. (A boldface font denotes a vector quantity.) If more than one source, receiver, or object is present within a scene, then an enumerating subscript is included (e.g., $\boldsymbol{r}_{si}$ is the location of the ith source). To compute scattering from any specific object, an object-centered coordinate system is used. That is, the origin of this system is within the object, and $\boldsymbol{d}_s = \boldsymbol{r}_s - \boldsymbol{r}_t$ and $\boldsymbol{d}_r = \boldsymbol{r}_r - \boldsymbol{r}_t$ are positional vectors for the source and receiver relative to the location of an object in the global coordinate system. Currently, six environments are supported by the TIER model. These include free-field, halfspace, waveguide, partial burial of an object, full burial, and an object within a layer (e.g., a mud layer above a sand basement). Each of these environments are described briefly below with the exception of the layered environment, which was not germane to SERDP MR19-1234.

Two additional assumptions are employed in the construction of the models for the environments. First, the distance of the source from an object is large in comparisons to the wavelength (i.e., and $d_s \gg \lambda$). Physically, an illuminating acoustic field is uniform across the cross-sectional area of an object, and hence, the characteristic dimensions of an object are small in comparison to d_s. Second, the distance from an object to a receiver is also assumed to be large in comparison to a wavelength (i.e., $d_r \gg \lambda$). This assumption is known as the far-field approximation. Appendix A explores the question: What does "large" mean?

2.1 Free-field Environment

When an object is sufficiently removed from any boundary and neither the transmitted sonar signal nor pressure scattered by an object interacts with a boundary, an object is said to be in the free field. The free-field environment is the simplest environmental model contained within the TIER model framework and can be expressed as

$$P_f(\omega) = r_0 P_{src}(\omega) \left[B_s(\hat{d}_s, \omega) \frac{\exp(i\omega t_s)}{d_s} \right] s(\hat{d}_s, \hat{d}_r, \omega) \left[B_r(\hat{d}_r, \omega) \frac{\exp(i\omega t_r)}{d_r} \right] \quad (1)$$

where r_0 is a reference distance (typically, 1 m) and $P_{src}(\omega)$ is the spectrum of the transmitted sonar pulse. The first factor in square brackets describes the propagation from the source to an object. The source's beam pattern is $B_s(\hat{d}_s, \omega)$ and $t_s = d_s/c_1$ is the propagation time delay. The

speed of sound in water is c_1. The TIER model assumes a negative time convention, $\exp(-i\omega t)$, with t and ω being time and angular frequency; and hence, a time delay enters as a positive phase shift. The second factor in square brackets is the propagation from an object to a receiver. The beam pattern for the receiver is $B_r(\hat{d}_r, \omega)$ and the time delay is $t_r = d_r/c_1$. The bistatic scattering amplitude (BSA) is $s(\hat{d}_s, \hat{d}_r, \omega)$. Its dependence on the unit vectors $\hat{d}_s$ and $\hat{d}_r$ signifies that the BSA depends on only the spherical polar and azimuthal angles of the source and receiver and is independent of d_s and d_r. The BSA contains all of the information about an object (e.g., shape, material composition, and directionality of the scattered pressure). Finally, throughout the remainder of Sec. 1, the dependency on angular frequency, ω, will be suppressed except in the propagation time delay factor.

Figure 1 shows an obvious ray diagram for the free-field scattering process. The source, receiver, and target are denoted by S_0, R_0, and T_0, respectively. With an arrow pointing in the direction of sound propagation, the diagram is $S_0 \rightarrow T_0 \rightarrow R_0$. Free-field scattering and this ray diagram are building blocks for other environments contained within the TIER model. Lastly, a form of Eq. (1) is used in Sec. 3 for the inversion of simulated scattered pressures to obtain bistatic scattering amplitudes.

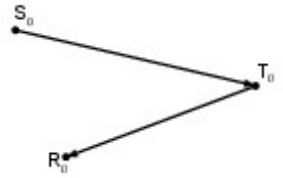

Figure 1. Ray diagram for a free-field environment is depicted.

2.2 Halfspace Environment

Under typical operational conditions for a short-range synthetic aperture sonar (SAS) platform, the air-water interface can be ignored because ray paths that interact with this interface are either removed by time-gating the received signals or suppressed by the beam patterns of the sonar. If the air-water interface is ignored, the environment is reduced to a halfspace (i.e., water above a sediment). When an object resides in the water or rests on the water-sediment interface, only four ray paths are possible as shown in Fig. 2(a). The method of images allows one to replace the water-sediment interface by an image source and image receiver that are located within the sediment. Figure 2(b) shows an equivalent set of free-field scattering geometries that replaces the interface (light-brown, dashed line). Here S_1 and R_1 an image source and image receiver.

(a) Halfspace (b) Halfspace ray diagram

Figure 2. (a) Due to reflection from the interface, four ray paths are possible. (b) Ray paths associated with images are shown.

The direct ray path is the path that would exist in the absences of the sediment, namely, the free-field ray diagram applies, $S_0 \to T_0 \to R_0$. Two ray paths are present with each ray path interacting once with the interface. These are sometimes referred to as the single-bounce ray paths and have the following diagrams: $S_0 \to T_0 \to R_1$ and $S_1 \to T_0 \to R_0$. The last ray path reflects from the interface twice (a so-called double-bounce ray path) and has the diagram $S_1 \to T_0 \to R_1$. These diagrams and Eq. (1) allow one to write an expression for the halfspace environment as

$$\begin{aligned} P_h = {} & r_0 P_{src}\left[B_s(\hat{d}_{s0})\frac{\exp(i\omega t_{s0})}{d_{s0}}\right] s(\hat{d}_{s0},\hat{d}_{r0})\left[B_r(\hat{d}_{r0})\frac{\exp(i\omega t_{r0})}{d_{r0}}\right] \\ & + r_0 P_{src}\left[B_s(\hat{d}_{s0})\frac{\exp(i\omega t_{s0})}{d_{s0}}\right] s(\hat{d}_{s0},\hat{d}_{r1})\left[B_r(\hat{d}_{r1})L(\theta_{r1})\frac{\exp(i\omega t_{r1})}{d_{r1}}\right] \\ & + r_0 P_{src}\left[B_s(\hat{d}_{s1})L(\theta_{s1})\frac{\exp(i\omega t_{s1})}{d_{s1}}\right] s(\hat{d}_{s1},\hat{d}_{r0})\left[B_r(\hat{d}_{r0})\frac{\exp(i\omega t_{r0})}{d_{r0}}\right] \\ & + r_0 P_{src}\left[B_s(\hat{d}_{s1})L(\theta_{s1})\frac{\exp(i\omega t_{s1})}{d_{s1}}\right] s(\hat{d}_{s1},\hat{d}_{r1})\left[B_r(\hat{d}_{r1})\frac{\exp(i\omega t_{r0})}{d_{r0}}\right]. \end{aligned} \tag{2}$$

With two sources and two receivers present, an enumerating subscript is included in Eq. (2) such that $\boldsymbol{d}_{s0} = \boldsymbol{r}_{t0} - \boldsymbol{r}_{s0}$, $\boldsymbol{d}_{s1} = \boldsymbol{r}_{t0} - \boldsymbol{r}_{s1}$, $\boldsymbol{d}_{r0} = \boldsymbol{r}_{r0} - \boldsymbol{r}_{t0}$, and $\boldsymbol{d}_{r1} = \boldsymbol{r}_{r1} - \boldsymbol{r}_{t0}$. The reflection coefficients $L(\theta_{s1})$ and $L(\theta_{r1})$ are defined in terms of the grazing angles associated with the ray paths originating at S_1 or terminating at R_1. These angles can be determined from $\cos\theta_{s1} = D_{s1}/d_{s1}$ and $\cos\theta_{r1} = D_{r1}/d_{r1}$ where D_{s1} and D_{r1} are horizontal distances defined by $D_{s1} = |\boldsymbol{R}_{t0} - \boldsymbol{R}_{s1}|$ and $D_{r1} = |\boldsymbol{R}_{r1} - \boldsymbol{R}_{t0}|$. In terms of Cartesian unit vectors $\hat{x}$ and $\hat{y}$, one has for example $\boldsymbol{R}_{s1} \equiv x_{s1}\hat{x} + y_{s1}\hat{y}$.

The reflection coefficient for a fluid-like sediment appears in Eq. (2) and has the form

$$L(\theta_g) = \frac{\rho\sin\theta_g - \left(\kappa^2 - \cos^2\theta_g\right)^{1/2}}{\rho\sin\theta_g + \left(\kappa^2 - \cos^2\theta_g\right)^{1/2}} \tag{3}$$

where θ_g is a local grazing angle. In Eq. (3), we have $\rho = \rho_2/\rho_1$, $\kappa = k_2/k_1 = (1 + i\delta)/v$ and $v = c_2/c_1$ is a real index of refraction. The fluid's sound speed and density are c_1 and ρ_1; while

c_2, ρ_2, and δ are respectively the speed of sound, density, and dimensionless loss parameter for the sediment. The wavenumbers for the sound in water and sediment are $k_1\ \omega/c_1$ and $k_2 = \omega/c_2$. When the air-water interface cannot be ignored as in Sec. 2.3, the reflecting interface is often treated as a pressure-release surface due to the large acoustic impedance mismatch between water and air. This yields $U(\theta_g) \equiv 1$ at the upper interface. For completeness, the pressure transmission coefficient from water into the sediment is

$$T_{12}(\theta_g) = \frac{2\rho \sin\theta_g}{\rho \sin\theta_g + \left(\kappa^2 - \cos^2\theta_g\right)^{1/2}} \tag{4}$$

and the coefficient for transmission from the sediment into water is

$$T_{21}(\theta_2) = \frac{2\kappa \sin\theta_2}{\kappa \sin\theta_2 + \rho\left(1 - \kappa^2 \cos^2\theta_2\right)^{1/2}} \tag{5}$$

with $\cos\theta_2 = \nu \cos\theta_g$. Equations (4) and (5) are used in Sec. 2.4 below.

2.3 Waveguide Environment

The Bay Experiment 2014 (BAYEX14) was conducted in St. Andrew Bay south of Panama City, FL. The water depth was nominally 8 meters. With objects placed more than 40 m in horizontal range from the APL-UW rail, the air-water interface cannot be ignored. When the wavelength of sound is much smaller than the depth of a water column, acoustic wave propagation may be approximated by an acoustic ray model [3]. The waveguide environment currently assumes that the water column is a homogeneous fluid layer bounded above by air and below by a sediment. The sediment is either a homogeneous attenuating fluid with a frequency-independent loss parameter [4] or a fluid described by an effective density fluid model [5]. In this environment, ray paths are straight, and can change direction only through reflection from the water-sediment or air-water interfaces. An overview of the waveguide environment is provided here, while a more detailed description can be found in [6].

Figure 3(a) depicts the scattering problem where the direct ray path and ray paths that interact at most once with either the upper or lower boundary are shown. The physical source, physical receiver, and object are located again at S_0, R_0, and T_0. Image sources, S_1 and S_2, and image receivers, R_1 and R_2, are reflected through the boundaries such that one can trace ray paths from and to these images. Figure 3(b) shows image sources and image receivers and their associated acoustic ray paths. It is noted that a ray path can interact more than once with an interface, and thus, several images can contribute to a received signal.

The general ray diagram for propagation from the ith source to the kth object and then to the jth receiver is $S_i \rightarrow T_k \rightarrow R_j$. One can use the same procedure as in the halfspace environment of Sec. 2.2 to superimpose the equivalent many free-field scattering ray diagrams to arrive at

$$P_s = r_0 P_{src} \sum_{j=0} \sum_{i=0} \left[A_{si} \frac{\exp(i\omega t_{si})}{d_{si}} \right] s(\hat{d}_{si}, \hat{d}_{rj}) \left[A_{rj} \frac{\exp(i\omega t_{rj})}{d_{rj}} \right] \tag{6}$$

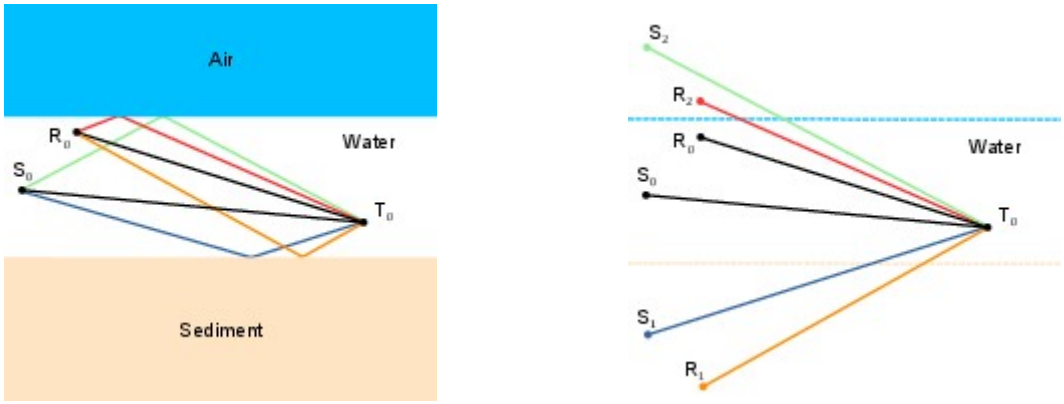

(a) Waveguide (b) Waveguide ray diagram

Figure 3: (a) Due to reflection from the lower and upper interfaces, nine ray paths occur with just two image sources and two image receivers. (b) Ray paths associated with images are shown.

as the spectrum for the total scattered pressure within a waveguide environment. The amplitudes are given by U

$$A_{si} = B_s(\hat{d}_{si})U^{n_i}(\theta_{si})L^{m_i}(\theta_{si}), \quad A_{rj} = B_r(\hat{d}_{rj})U^{n_j}(\theta_{rj})L^{m_j}(\theta_{rj}) \tag{7}$$

with the reflection coefficients at the lower and upper interfaces L and U. In Eq. (7), the local grazing angle for a particular ray path is either $\cos\theta_{si} = D_{si}/d_{si}$ or $\cos\theta_{rj} = D_{rj}/d_{rj}$. The n_i, m_i, n_j, and m_j exponents enumerate the number of interactions a ray path has with the boundaries of the waveguide

2.4 Partially Buried and Fully Buried Environments

Partially and fully buried environments are special cases of the halfspace environment described in Sec. 2.2 with the axis of symmetry of an object parallel to the water-sediment interface. These environments consider a finite cylindrical object, or in the case of an UXO, an enclosing finite cylindrical surface, which will be referred to here as simply a cylinder. Figure 4(a) shows a cylinder of radius a in a broadside orientation to a source and receiver. The physical source and receiver are located in the far field at S_0 and R_0 while the image source and image receiver are S_1 and R_1. Colors are used in Fig. 4 to aid the eye in labeling lines and angles with symbols. In addition, the r and s subscripts used in mathematical expressions have been suppressed for clarity (e.g., $\theta_1 \equiv \theta_{s1}$). The depicted scene in Fig. 4(a) is described by Eq. (2) with the cylinder sitting proud (i.e., 0% burial case).

The partially and fully buried environments currently use simple arguments from geometric acoustics to alter Eq. (2) as the cylinder is buried to different depths. If a ray path can no longer reach an object, it is simply discard. If a ray path can still reach an object and it crosses the water-sediment interface, then refraction occurs. The 0% burial case sets thresholds for the four ray paths. The S_1 ray path reflects from the interface before interacting with an object. From Fig. 4(b), one can easily determine that the S_1 ray path intersects the cylinder's surface at a height of

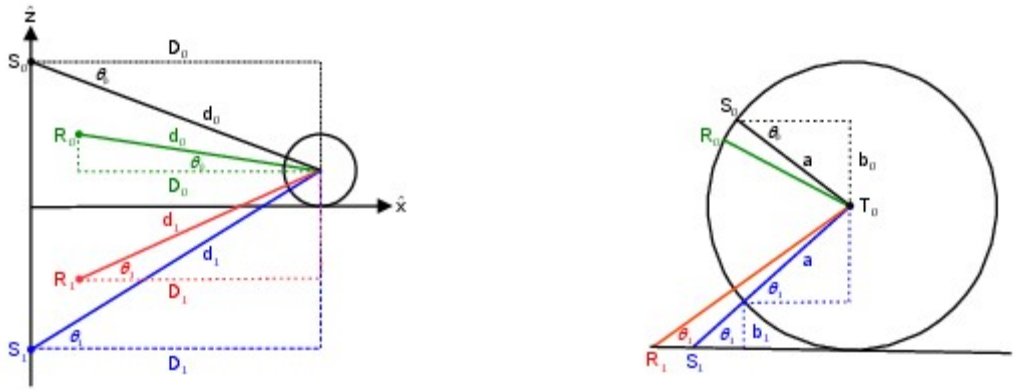

(a) Broadside Cylinder (b) Close-up of Cylinder

Figure 4: (a) Four ray paths interact with a proud cylinder at broadside. (b) A close-up view of the proud cylinder allows one to define angles and lengths.

$b_{s1} = a(1 - \sin\theta_{s1})$ above the interface. Noting that the location of an image source within the sediment is independent of the burial state of an object and if an object experiences some degree of burial, then the grazing angle θ_{s1} is smaller than the proud case and the point of intersection of the S_1 ray path with the water-sediment interface moves towards the cylinder. In addition, the far-field approximation assumes uniform illumination of an object, and hence, adjacent acoustic rays are nearly parallel to the S_1 ray path. With the center of the target at $z_t = b_{s1}$ zt, the S_1 ray path intersects the cylinder's surface at the water-sediment interface. For $z_t < b_{s1}$, the ray path never reaches the cylinder, and it is discarded. This behavior coincides with a Heaviside step function

$$H(z - z_0) = \begin{matrix} 1, & z > z_0, \\ 1/2, & z = z_0, \\ 0, & z < z_0, \end{matrix} \tag{8}$$

A similar argument holds for the R_1 ray path where the threshold is set to $b_{r1} = a(1 - \sin\theta_{r1})$. Now, consider the S_0 and R_0 ray paths. These paths always exist and transition into refracted paths if the cylinder is sufficiently buried. In Fig. 4(b), one has $b_{s0} = a\sin\theta_{s0}$. When $z_t = -b_{s0}$, the intersection of the S_0 ray path and surface of the cylinder occurs in the water-sediment interface. Hence, for $z_t < -b_{s0}$, this ray path must cross the interface to reach the cylinder via refraction. In addition to refraction, the ray path is weighted by the transmission coefficient, $T_{12}(\theta_{s0})$, defined in Eq. (4). The following expression

$$G_s(z) = \begin{matrix} 1, & z \geq -b_{s0}, \\ T_{s0}(\theta_{s0}), & z < -b_{s0}, \end{matrix} \tag{9}$$

is used in Eq. (11) below. A similar construction holds for the R_0 ray path except the transmission occurs from sediment into water. The transmission coefficient is then $T_{21}(\theta_{r0})$ and is given in Eq. (5). Define $G_r(z)$ from Eq. (9) with T_{12} replaced by $T_{21}$and the subscript $s \to r$. With these considerations, the spectrum of the scattered pressure becomes

$$
\begin{aligned}
P_h = {} & r_0 P_{src} A_1 \left[B_s(\hat{d}_{s0}) \frac{\exp(i\omega t_{s0})}{d_{s0}} \right] s(\hat{d}_{s0}, \hat{d}_{r0}) \left[B_r(\hat{d}_{r0}) \frac{\exp(i\omega t_{r0})}{d_{r0}} \right] \\
& + r_0 P_{src} A_2 \left[B_s(\hat{d}_{s0}) \frac{\exp(i\omega t_{s0})}{d_{s0}} \right] s(\hat{d}_{s0}, \hat{d}_{r1}) \left[B_r(\hat{d}_{r1}) L(\theta_{r1}) \frac{\exp(i\omega t_{r1})}{d_{r1}} \right] \\
& + r_0 P_{src} A_3 \left[B_s(\hat{d}_{s1}) L(\theta_{s1}) \frac{\exp(i\omega t_{s1})}{d_{s1}} \right] s(\hat{d}_{s1}, \hat{d}_{r0}) \left[B_r(\hat{d}_{r0}) \frac{\exp(i\omega t_{r0})}{d_{r0}} \right] \\
& + r_0 P_{src} A_4 \left[B_s(\hat{d}_{s1}) L(\theta_{s1}) \frac{\exp(i\omega t_{s1})}{d_{s1}} \right] s(\hat{d}_{s1}, \hat{d}_{r1}) \left[B_r(\hat{d}_{r1}) \frac{\exp(i\omega t_{r0})}{d_{r0}} \right].
\end{aligned}
\tag{10}
$$

with

$$
\begin{aligned}
A_1 &= G_s(z_t) G_r(z_t), & A_2 &= G_s(z_t) H(z_t - b_{r1}), \\
A_3 &= H(z_t - b_{s1}) G_r(z_t), & A_4 &= H(z_t - b_{s1}) H(z_t - b_{r1}),
\end{aligned}
\tag{11}
$$

Inspection of Eq. (10) reveals the same four ray paths of Eq. (2) for the halfspace environment, except the paths here are weighted by the amplitudes A_1, A_2, A_3, and A_4. Finally, due to the presence of Heaviside step functions in A_2, A_3, and A_4, the actual number of ray contributions depends on burial depth.

Equation (10) was developed for an object with a finite cylindrical surface in a broadside orientation. This expression holds for angles other than broadside as long as the side of the cylinder is within the field of view of a source or receiver with one caveat. When the source (receiver) is above the object and looking down. If the source (receiver) is within the footprint of the cross-sectional area of the cylinder projected on the water-sediment interface, then an image source (image receiver) does not occur due to the shadowing caused by the cylinder. In this case, an image source (image receiver) is simply omitted.

When the scattering geometry is rotated to an end-on ensonification, Eq. (10) needs to be modified. A finite cylindrical object or enclosing cylindrical surface has flat ends. For a partially buried object, the four ray paths can reach the exposed portion of the end. Figure 5(a) depicts a family of nearly parallel rays reflecting from the interface prior to interacting with the cylinder. A similar diagram can be drawn for ray paths that reach an image receiver after reflecting from the cylinder's end. The fractional exposed area can be found be considering either Figs. 5(b) or 5(c);

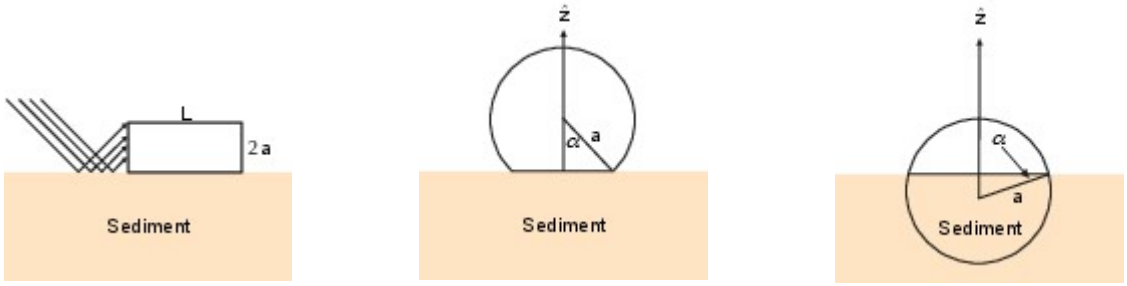

(a) End-on Cylinder (b) $a > Z_t \geq 0$ case (c) $0 > Z_t \geq -a$ case

Figure 5: Ray paths associated with an image source are depicted along with the fractional exposed area, which defines α.

the selection of which depends on if $z_t \geq 0$. If the cylinder is fully buried, only the ray path associated with the physical source and physical receiver survives. Equation (11) is modified to

$$A_e(z_t) = \begin{cases} 1-\alpha/\pi, & z_t = \cos\alpha, \quad a > z_t \geq 0, \\ 1/2-\alpha/\pi, & z_t = \sin\alpha, \quad 0 > z_t \geq -a, \\ 0, & z_t < -a. \end{cases} \tag{13}$$

Heaviside step functions in Eq. (8) are a result of a geometric acoustic approximation that simply turns a ray on or off. In physical acoustics, diffraction by an edge causes some energy to be redirected into the shadow region such that a sharp shadow boundary does not exist. A Fresnel integral $F(z)$ is a result of edge diffraction, and by extension, replacement of $H(z)$ by $F(z)$ may allow removal of this on-off condition.

3 Bistatic Scattering Amplitude

In Sec. 1, the BSA is introduced in the free-field environment. When the incident pressure from a source takes on a planar nature at an object (i.e., $r_s \gg 1$), one has essentially the scattering of a plane wave from that object. In this case, the spectrum of the free-field scattered pressure can be written as

$$P_s(\omega) = p_0 s(\hat{r}_s, \hat{r}_r, \omega) \frac{\exp(i\omega r_r/c_1)}{r_r} \tag{14}$$

[e.g., see Appendix A, Eq. (A6)]. Once again, the angular frequency is ω, p_0 carries units of pressure, and c_1 is the sound speed in the fluid. The scattering amplitude is $s(\hat{r}_s, \hat{r}_r, \omega)$, which contains all the information about an object and carries units of length. The unit vector $\hat{r}_s$ accounts for the direction of the incident sound and $\hat{r}_r$ is the unit vector pointing towards a receiver. In terms of spherical polar and azimuthal angles, θ and ϕ, the general form of the scattering amplitude is $s(\theta_s, \phi_s, \theta_r, \phi_r, \omega)$. For objects other than spheres [7–9] and approximations for finite cylinders [10–12], Eq. (14) is inverted to obtain

$$s(\hat{r}_s, \hat{r}_r, \omega) = \frac{r_r}{p_0} P_s(\omega) \exp(-i\omega r_r/c_1) \tag{15}$$

which is used to generate tables for the TIER model. For axisymmetric objects, we employed a hybrid 2-D/3-D model [13,14] to simulated $P_s(\omega)$ and then use Eq. (15) to obtain the BSA. The hybrid model combines a finite-element (FE) model and Helmholtz integral. The former predicts the scattered pressure and normal derivatives in the near field of an object and the latter then propagates the pressure to a selected far-field distance. The hybrid model takes advantage of the symmetry of an object by decomposing the full 3-D problem into a series of independent 2-D Fourier modal subproblems.

APL-UW's initial foray into the scattering from an object near the water-sediment interface considered the special case of a proud object with its axis of symmetry parallel to the interface. The source and receiver were also assumed to be co-located, because standoff distances from objects in our experiments were significantly larger than the source-receiver separation distance. From Fig. 2 of Sec. 2.2, we see that the source, receiver, object, and images lie in a vertical plane, which is perpendicular to the water-sediment interface. The monostatic assumption means that $\hat{r}_r = -\hat{r}_s$, and the grazing angle θ_g is sufficient to parameterize $s(\theta_{cyl}, \phi_{cyl}, \omega)$ with $\theta_{cyl}(\theta_g)$ and $\phi_{cyl}(\theta_g)$ [1, 6]. Table 1 lists objects that have a monostatic scattering amplitude (MSA) table,

s_{ijk}, where the indices into a table are determined from $i = \theta_{cyl}/\Delta\theta_{cyl}$, $j = \phi_{cyl}/\Delta\phi_{cyl}$, and $k = f/\Delta f$. These tables typically have a resolution of $\Delta\theta_{cyl} = \Delta\phi_{cyl} = 1^{\circ}$ or 2° $\Delta f = 100$ Hz. Two file sizes are reported, which correspond to an uncompressed table and the same data compressed with the zlib library.

Object	Size (MB)	Zlib (MB)	c_1 (m/s)	Comment
Aluminum cylinder	145	56	1464	$L = 2$ ft, $a = 1/2$ ft
Aluminum cylinder	145	57	1530	$L = 2$ ft, $a = 1/2$ ft
Aluminum cylinder	145	59	1694	$L = 2$ ft, $a = 1/2$ ft
Aluminum cylinder	73	28	1530	$L = 3$ ft, $a = 1/2$ ft
Aluminum pipe	145	53	1464	$L = 2$ ft, $a = 1/2$ ft, $h = 3/8$ ft
Aluminum pipe	145	53	1530	$L = 2$ ft, $a = 1/2$ ft, $h = 3/8$ ft
100-mm replica	145	56	1464	Aluminum
100-mm replica	145	52	1464	Rigid
100-mm replica	145	55	1464	Stainless steel
100-mm replica	145	57	1530	Aluminum
100-mm replica	145	57	1530	Rigid
100-mm replica	145	57	1530	Stainless steel
105-mm shell	145	58	1530	Air-filled
105-mm shell	145	60	1530	Water-filled
105-mm shell	145	49	1530	Rigid response
155-mm shell	145	58	1530	End cap, air-filled
155-mm shell	145	58	1530	End cap, water-filled
155-mm shell	145	49	1530	End cap, rigid response
155-mm shell	145	58	1530	No end cap
155-mm shell	145	52	1530	No end cap, rigid response
Scuba tank	145	57	1530	No stem
Scuba tank	145	51	1530	No stem, rigid response
55-gallon oil drum	290	119	1530	One end opened

Table 1: Monostatic scattering amplitudes are available for the objects listed here. These tables are restricted to co-located source and receiver, and require an object's symmetry axis to be parallel to water-sediment interface. Uncompressed and compressed files sizes are listed.

SERDP MR19-1234 sought to remove the co-location assumption, because systems under development at APL-UW and ARL-PSU have significant source-receiver separation in comparison to anticipated stand-off distances. When the angular separation of the source and receiver relative to an object standoff distance was small, an attempt was made to re-use a monostatic scattering amplitude, but this quickly fails as the standoff distance approaches 5 m. For the APL-UW rail experiments, the closest approach to an object was 5 m and the distance between the source and receiver was 0.3 m. This yields an approximate 3.4° angular separation. The downward-looking sonar on APL-UW's MuST is composed from two sources with one at each end of a 64-element receiving array. For an array with a 1.6-m length, the angular separation between a source and most distal element is $\approx 18.2^{\circ}$. In addition, munitions at live sites may have

undergone deformation, structural compromise (e.g., nose-cone broken off), or corrosion, which breaks the axisymmetric assumption. Clearly, full bistatic scattering amplitudes are required.

3.1 Initial Effort

Our initial effort in the generation of BSA tables still exploited the axisymmetry of the UXO expected to be found at munition remediation sites and APL-UW's reference object of a finite solid aluminum cylinder. With the symmetry axis aligned with the z-axis, the source can be restricted to the xz-plane, which means $\phi_s \equiv 0°$. Figure 6 shows the scattering geometry for a cylinder of length L and radius a where $\theta_s \neq \theta_r$ such that the BSA is $s(\theta_s, \theta_r, \phi_r, \omega)$.

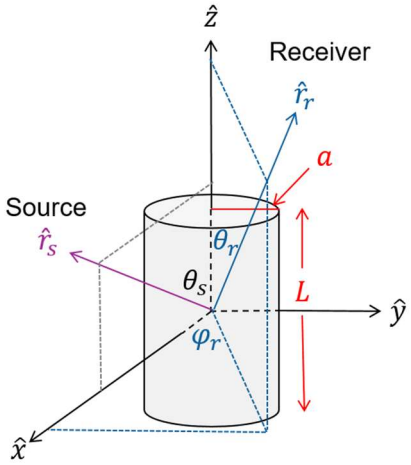

Figure 6: The target-centered coordinate system used in bistatic scattering from axisymmetric objects.

To generate a BSA table, we first note that $0^\circ \leq \theta_s \leq 180^\circ$, $0^\circ \leq \theta_r \leq 180^\circ$, $0^\circ \leq \phi_r \leq 180^\circ$, and $0 \leq$ f ≤ 30 kHz. Using the resolution of a MSA table, $\Delta\theta_s = \Delta\theta_r = \Delta\phi_r = 1^\circ$ and $\Delta f = 100$ Hz gives a four-dimensional table with a size of 181 × 181 × 181 × 291, which is prohibitively large. Thus, a three-dimensional table was generated for each source location where each table contains 181×181×291 entries. The first step executes the hybrid model [6] with a fixed source location in the xz-plane. The scattered pressure on a hemispherical surface at $r_r = 10$ or 20 m is then predicted for the discrete θ_r, ϕ_r and f. Equation (15) is then used to invert the scattered pressure to give

$$s_{ijk} = \frac{r_r}{p_0} P_s(j\Delta\theta_r, k\Delta\phi_r, l\Delta f) exp(-i2\pi l\Delta f r_r/c_1) \tag{16}$$

with $j = 0, 1, \ldots, J$; $k = 0, 1, \ldots, K$; and $l = 0, 1, \ldots, L$. Note, a table is constructed in terms of the actual frequency f instead of the angular frequency ω. Under this initial effort, BSA for 2:1 aluminum cylinder and pipe, scuba tank, aluminum replica of a 100-mm UXO, and water-filled 155-mm howitzer shell have been constructed.

Returning to the size of a single table, the number of complex entries is 181×181×291. In single precision floating point arithmetic, an entry occupies 8 bytes. This means a single table consumes 72.73 MB of memory and with 181 source locations, the BSA for an object occupies

12.86 GB of disk space. Scaling s_{jkl} and conversion to two 2-byte integers provides an immediate reduction in table size to 36.37 MB. This reduces the relative dynamic range of simulated data from 144 dB to approximately 90 dB. A further reduction can be achieved through compression, which typically provides an addition 10–25% file size reduction.

The TIER model determines θ_s, which rarely matches a $i\Delta\theta_s$ value. This means two tables are loaded into memory. For example, if $\theta_s = 23.2^\circ$ and $\Delta\theta = 1^\circ$, then the tables for 23° and 24° are loaded. The loading process decompresses a table and converts it back to a complex-valued scattering amplitude. Interpolation methods are then used to evaluate the required $s(\theta_s = 23.2^\circ, \theta_r, \phi_r, \omega)$. In the original implementation, pairs of tables were loaded on an as-needed basis. Profiles from simulations involving second-order multiple scattering from two 2:1 aluminum cylinders revealed significant reloading of tables as the sonar platform moved along a linear path. A caching scheme has been implemented to save up to ten tables. After θ_s has been determined if the tables are already in memory, those tables are used. If a table is not currently in the cache and a cache slot is available, then a cache slot is allocated and the table is loaded from disk. If a table is not currently in the cache and no cache slots are available, then all tables in the cache are flushed. The file loading is summarized in Table 2. The reduction in file loads represents a significant decrease in computation time.

Order	Uncached	Cached
First	214	106
Second	3208	156
Third	8006	207
Fourth	14442	207

Table 2: Number of tables loaded during first- through fourth-order multiple scattering simulations are shown. Under the original uncached scheme, only previously loaded tables were re-used if the next θ_s could utilized these table. The new caching scheme significantly reduced file reloads.

3.2 Reduction in number of table entries

The initial effort described in Sec. 3.1 has two drawbacks. First, angular increments must be chosen to adequately sample a spherical surface that encloses an object. If a uniform increment is used, then this leads to either an oversampling or undersampling of regions of angular space. Figure 7(a) depicts 630 points on a hemispherical surface, where $\Delta\theta = \Delta\phi = 3^\circ$. It clearly shows an oversampling near the poles and an undersampling near the equator. Choosing a sufficiently small angular increment to adequate sample near the equator causes a significant oversampling at the poles, which leads to the second drawback, namely, large tables (i.e., large file sizes). Two questions are then motivated by Fig. 7(a):

- *How does one distribute a fixed number of points on a spherical surface?*
- *How many points are needed?*

The first question is an optimization problem where one tries to minimize the maximum distance between all neighboring points. Fortunately, this question has been an active area of research in many fields of science [15, 16]. Appendix B describes a procedure from [17] that can be used to obtain a nearly uniform distribution of n points on a spherical surface. This procedure

is called a Fibonacci lattice or golden spiral. Figure 7(b) shows the results of using Eq. (B3) of Appendix B to generate a golden spiral distribution with $n = 626$.

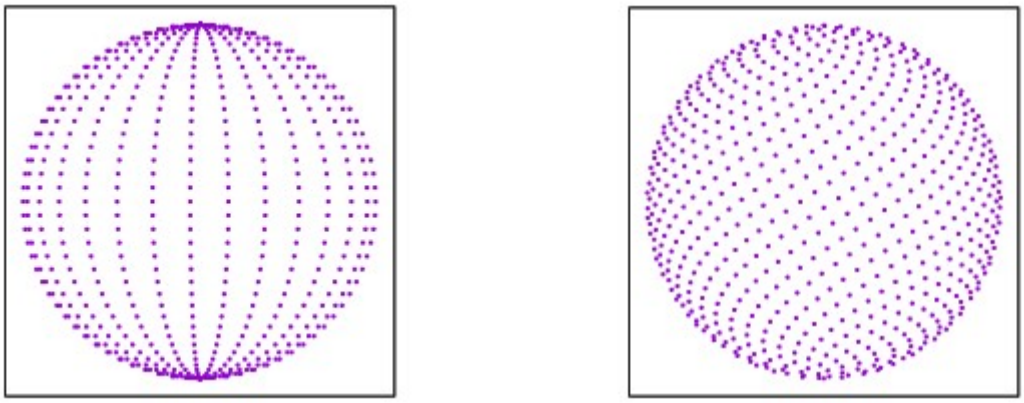

(a) Fixed $\Delta\theta$ and $\Delta\phi$ (b) Golden spiral

Figure 7: (a) With $\Delta\theta = \Delta\phi = 3^{\circ}$, 630 points are placed on the hemispherical surface. (b) 626 points are distributed on the hemisphere via the gold spiral.

The second question requires a detour into the transition matrix (T-matrix) formulation of scattering theory [18–21]. The T-matrix formalism represents the scattered pressure in terms of a complete basis set of irregular wave functions ψ_{lm}. The incident pressure on an object is expanded in a complete basis set of regular wave functions $\hat{\psi}_{lm} = \Re[\psi_{lm}]$ with $\Re[\cdots]$ indicating the real part of the enclosed quantity. A regular wave function is finite at the origin while an irregular wave function has a singularity at the origin and it satisfies the Sommerfeld radiation condition $\psi_{lm} \to 0$ as $r_r \to \infty$. For a finite volume scatterer, the expansions rfor the incident and scattered pressures are $p_{inc}(\boldsymbol{r}_s) = \sum a_{l'm'}\,\hat{\psi}_{l'm'}$ and $p_{sca}(\boldsymbol{r}_r) = \sum b_{lm}\,\psi_{lm}$.cThe T-matrix relates the unknown expansion coefficients b_{lm}blm to the presumably known coefficients $a_{l'm'}$ through surface integrals and boundary conditions on the surface of an obstacle. In matrix notation, one has $\boldsymbol{b} = \boldsymbol{T}\boldsymbol{a}$. For a fixed source location and in the far field of an obstacle, $p_{sca}(\boldsymbol{r}_r)$ takes on the form of Eq. (14)

$$p_{sca}(r_r) = \left[\sum_{l=0}^{\infty}\sum_{m=-l}^{l} c_{lm}Y_{lm}(\theta_r,\phi_r)\right]\frac{\exp(i\omega r_r/c_1)}{r_r} \tag{17}$$

where Y_{lm} is a spherical harmonic and c_{lm} represents a new set of coefficients. The question is then for what value of l can theω infinite summation be truncated? For a spherical target, the maximum l is slightly larger than $\omega a/c_1$ with a the radius of the sphere (and spherical symmetry implies $m \equiv 0$). From an inverse scattering viewpoint, the question is how many points are needed on a spherical surface in the far field of an object to resolve the spherical harmonic with the largest l value? Table 3 is a count of the number of expansion coefficients that appear in Eq. (17) for a given truncation value of l. For an inverse problem one needs at least one point on the surface for each coefficient c_{lm}. Thus, if a BSA table can be constructed with say 3000 point on a spherical surface, then this would represent a factor of 10 reduction in a BSA table size (i.e., 181 × 181 = 32761 versus 3000).

l_{max}	0	31	44	54	63	70
$m = 2l + 1$	1	63	89	109	127	141
$n = \sum_l (2l + 1)$	1	1024	2025	3025	4096	5041

Table 3: Top row is a tentative truncation value. Middle row is the number of Y_{lm} for a given l value (i.e., $-l \leq m \leq l$). Last row is the total number of unknown b_{lm} in Eq. (17).

Prior to the generation of BSA tables, based on a golden spiral distribution of points, it is profitable to consider the scattering from a finite cylinder. Stanton developed an analytic expression for broadside and near-broadside scattering from a finite cylirnder [11, 12]. Later, Ye revisited Stanton's model and provided a scattering amplitude that includes scattering from a flat end [10]. For a finite cylinder with its symmetry axis aligned with the z-axis and an incident wave vector confined to the xz-plane, their results can be rewritten as a form function [see Appendix A, Eq. (A6)]

$$F_{cyl}(\theta_r, \phi_r) = F_{st}(\theta_r, \phi_r) + F_{ye}(\theta_r) \tag{18}$$

$$F_{st}(\theta_r, \phi_r) = \frac{L}{a}\left[-\frac{ik_\perp a}{\pi}\right]\frac{\sin(k_\parallel L)}{k_\parallel L}F_\infty^{cyl}(k_\perp a, \phi_r) \tag{19}$$

$$F_{ye}(\theta_r) = -i\Gamma(\pi/2 - \theta_r)J_1(2k_\parallel a)\cot\theta_r exp(-ik_\perp L) \tag{20}$$

where the subscripts st and ye denote Stanton's and Ye's results, respectively. Explicit dependence on the receiver's polar and azimuthal angles are shown in Eqs. (18)–(20). The portions of the incident wavenumber parallel and perpendicular to the z-axis are $k_\parallel = k\sin\theta_s$ and $k_\perp = k\cos\theta_s$. In Eq. (19), $F_\infty^{cyl}(k_\perp a, \phi_r)$ is the form function for scattering from an infinitely long cylinder, and J_1 in Eq. (20) is a first-order cylindrical Bessel function.

The TIER model contains an implementation of Eqs. (18)–(20) for rigid and fluid finite cylinders. Consider a 2:1 rigid cylinder with its axis aligned with the z-axis and centered on the origin of the coordinate system (see Fig. 6). An omni-directional source is placed at $r_s = 10$ m in the xz-plane. The TIER model simulated the scattering of a 1–30 kHz LFM pulse from the cylinder with θ_s set to one of 0° (end-on), 15°, …, 90° (broadside). Receivers were distributed on a $r_r = 10$ m spherical surface via the golden spiral where n was set to 500, 1500, …, 3000. Time-domain beam forming of the simulated scattered signals was performed to render a 1.25 × 1.25 × 1.25 m^3 volume of the intensity. Figure 8 contains the maximum intensity projection (MIP) images of the intensity projected onto the xy-, yz-, and xz-planes. Each column is labeled with the relevant θ_s. Casual inspect immediately reveals that the distribution with 500 points is inadequate to resolve the cylinder. As the number of points increases one observes an improvement in the resolution, and it is seen that $n = 3000$ provided fairly sharp features.

The results of Fig. 8 are for a broadband pulse, and does not provide insight into any frequency dependence with the choice of n. Simulations were performed where a short sinewave tone burst was incident on the rigid cylinder. Scattered time signals were again recorded and MIP images were constructed in the xy-plane. Figures 9(a) and 9(b) correspond to source locations for broadside ($\theta_s = 90^\circ$) and an end-on ($\theta_s = 0^\circ$) orientations, respectively. The top row is for a 1 kHz tone burst and the bottom row had a 15 kHz carrier frequency. Each column is labeled with the number of points in the golden spiral distribution. It is evident from Fig. 9 that $n = 500$ is

sufficient to resolve the cylinder at 1 kHz, but $n > 2500$ is need at 15 kHz. Although it is tempting to construct tables that exploit this dependency to reduce table sizes, the indexing scheme utilizes a search for a point within the set of golden spiral points that is closest to an arbitrary r_r and it is convenient to have a single set.

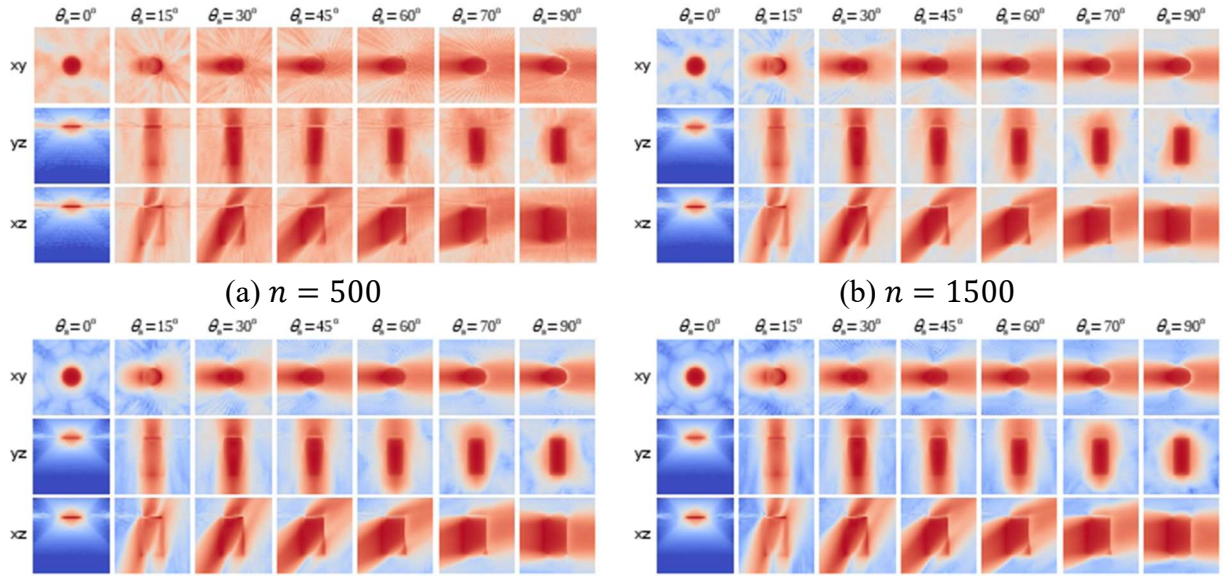

(a) $n = 500$ (b) $n = 1500$

(c) $n = 2500$ (d) $n = 3000$

Figure 8: Maximum intensity projections in the xy, xz, and yz-planes are depicted for the indicated number of surface points. All images are normalized to the same 0 (red) to -40 dB (blue).

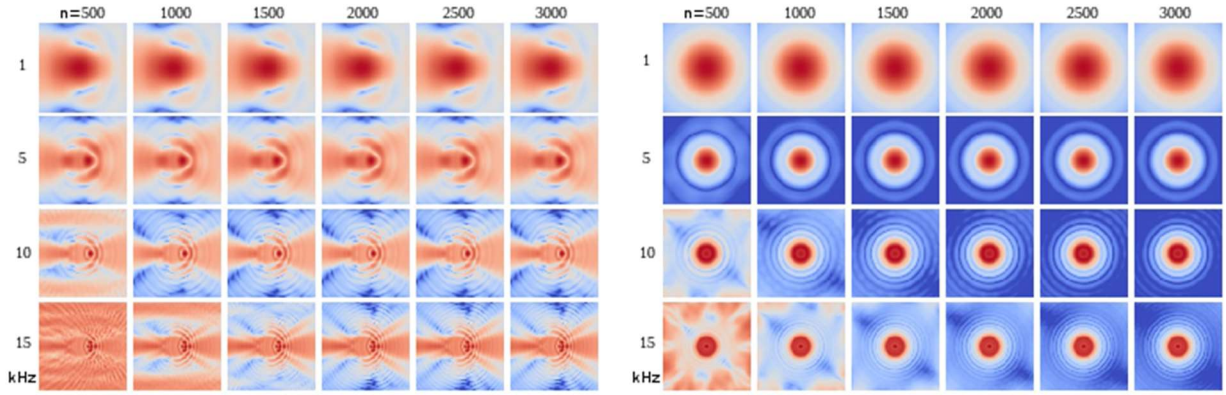

(a) Broadside orientation (b) End-on orientation

Figure 9: Maximum intensity projections in the xy-plane for broadside and end-on orientations. All images are normalized to the same 0 (red) to -40 dB (blue).

With completion of the simulations for a 2:1 finite rigid cylinder, BSA tables were constructed for a 2:1 aluminum cylinder and pipe (3/8 inch wall thickness), stemless scuba tank, aluminum replica of an 100-mm UXO, and a water-filled 155-mm shell. These objects retain axisymmetry, so APL-UW's hybrid model can provide high-fidelity simulations of the scattered pressure at receivers located on a spherical surface. Axisymmetry is exploited by restricting the source to reside in the xz-plane. This then allows construction of 181 BSA tables such that $\theta_s = i\Delta\theta_s$ with

$\Delta\theta_s = 1^\circ$ and $i = 0, 2, \ldots, 180$. A golden spiral distribution with $n = 5001$ receiver locations was generated from Eq. (B3). At each receiver location, the pressure was recorded in the $1 \le f \le 30$ kHz frequency range with a $\Delta f = 100$ Hz increment. For the hybrid model, the simulations used $r_s = r_r = 10$ m. It is noted that Appendix A not only looked at far-field scattering but also includes the scattering from a rigid sphere where a table was generated. Those results suggest that future tables may benefit from an increase of $r_s$rs and/or r_r to larger values. Each individual table contains 5001 × 301 entries (for $0 \le f < 1$ kHz the table is padded with zeros). With file compression, it occupies approximately 3.5–5.1 MB of disk space. Thus, when compared to compressed file sizes reported in Table 1, this is a substantial reduction.

The choice of 5001 over the maximum value of 3000 in Table 3 was motivated by two considerations. First, the eccentricity and sharp features of an UXO (e.g., nose cone or an edge due to structural compromise) , require a densely populated table to resolve a feature. In addition, the elastic nature of an object may require a finer table resolution to adequately capture an elastic response. Second, the upper frequency of 30 kHz is adequate for APL-UW's sonars, but may need to be pushed to a higher limit to accommodate other broadband LF sonars. In fact, the BSA tables for the 2:1 solid aluminum cylinder have been extended to a maximum frequency of 50 kHz. With compression the file size is nominally 6.1 MB per table. Finally, by using the same 5001 points for all objects, the complexity of the indexing scheme is reduced in that only a single list of receiver positions needs to be maintained.

A comment on indexing is merited. For an arbitrary θ_s, two tables can be quickly identify from $i\Delta\theta_s < \theta_s < (i+1)\Delta\theta_s$ with $i = \lfloor \theta_s/\Delta\theta_s \rfloor$. The symbol $\lfloor \cdots \rfloor$ indicates the fractional portion of the quotient is discarded. Both tables are loaded and available for interpolation. The indexing associated with the receiver locations results in an increase in complexity, because one cannot simply use $\Delta\theta_r$ and $\Delta\phi_r$ to determine indices. The list of receiver positions in the golden spiral are converted to unit vectors via $\hat{\boldsymbol{r}}_{rq} = \boldsymbol{r}_{rq}/r_{rq}$ with $q = 1, 2, \cdots, 5001$. For an arbitrary receiver location $\boldsymbol{r}_r$ the unit vector is $\hat{\boldsymbol{r}}_r = \boldsymbol{r}_r/r_r$. To find a table entry, the list of $\hat{\boldsymbol{r}}_{rq}$ is searched for the minimum $\left|\hat{\boldsymbol{r}}_r - \hat{\boldsymbol{r}}_{rq}\right|^2$. This search yields the table entry which is the nearest receiver location to the actual location. An interpolation scheme can be used by locating the closest two or three table entries, but at this time only the search portion of the scheme has been implemented. Finally, it is noted that the caching scheme described above in Sec. 3.1 can still, be used to reduce unnecessary reloading of tables as a sonar platform moves through a scene.

An initial test of the new BSA tables considered monostatic scattering from the five objects listed above. For co-located sources and receivers at $r_s = r_r = 20$ m, the golden spiral was again utilized to generate a distribution with $n = 2000$ points. That is, no point in this distribution matches a point used in the production of a BSA table. A 1–30 kHz LFM pulse was transmitted from an omni-directional source and the receiver was also assumed to be omni-directional. Time-domain beam forming was used to render an intensity in a 1.25 × 1.25 × 1.25 m^3 volume, and MIP images were projected into the xy-, xz-, and yz-planes. The initial orientation of an object aligned the symmetry axis with the z-axis, which coincides with an Euler angle rotation of $(\alpha, \beta, \gamma) = (0^\circ, 0^\circ, 0^\circ)$. The Euler angle convention used here is an α rotation about the z-axis, followed by a β rotation about the y'-axis in the new coordinate system, and then a final γ rotation about the z''-axis. All rotations are counter-clockwise about the axes. Four additional rotations about the y'-axis were also simulated: $\beta = 30^\circ, 45^\circ, 60^\circ$, and 90°. The last rotation has the symmetry axis parallel to the xy-plane. Because $\alpha = \gamma = 0^\circ$, the β rotation amounts to a counter-clockwise

rotation about the original y-axis. Figures 10–14 show the MIP images for the five objects. The top, middle, and bottom rows are labeled with the plane of the image, and each column is labeled by the Euler angles. The middle row clearly shows the progression of β from 0° to 90°. The xy-plane and yz-plane show a symmetry in the displayed images, but one must visualize a cut through a rotated object that is projected onto the plane. Finally, the BSA tables for the cylinder and 155-mm shell, which gave the results in Figs. 10 and 11, are used in multiple scattering simulations in Sec. 4 (see the discussion for Fig. 18).

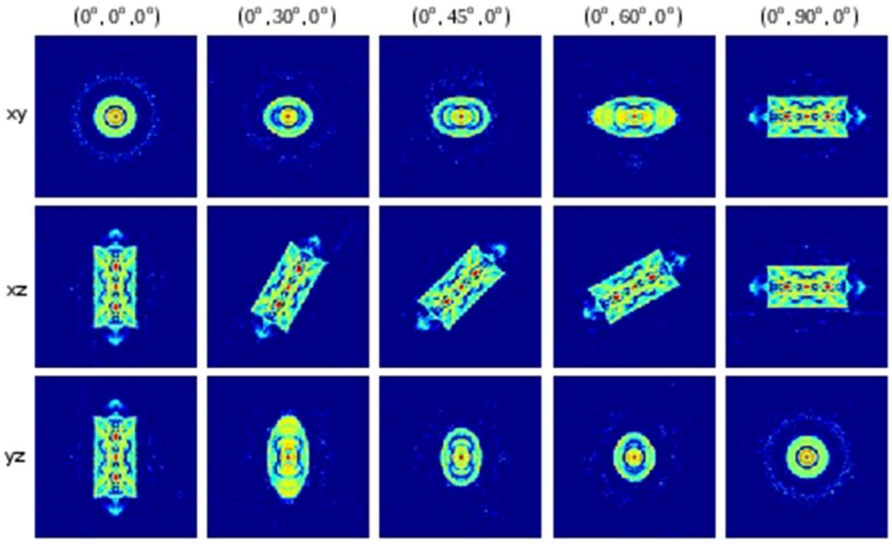

Figure 10: MIP images for a solid 2:1 aluminum cylinder in three perpendicular planes are displayed for several Euler angle rotations. Each image is normalized by the maximum voxel, and the color scale is 0 to -20 dB.

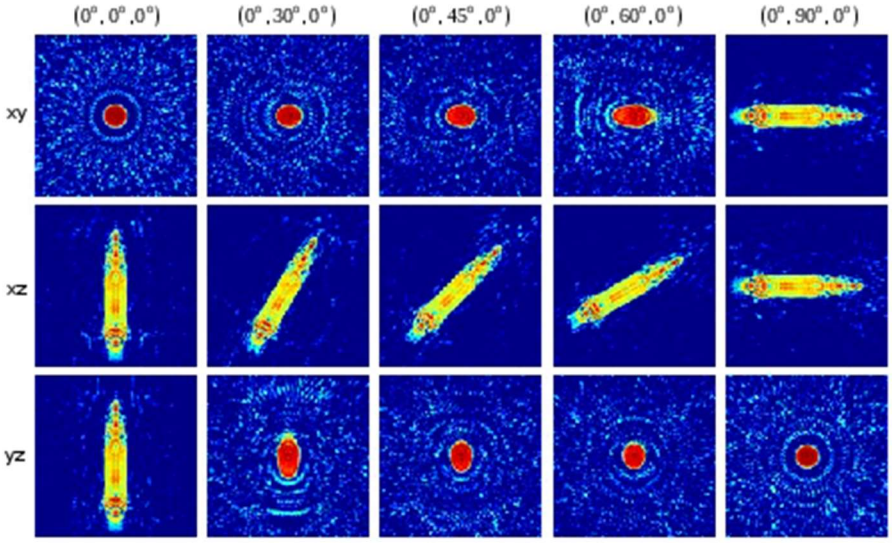

Figure 11: MIP images for a 155-mm howitzer shell are displayed. The shell has a bottom end cap and is water filled. Each image is normalized by the maximum voxel. The color scale is 0 to -20 dB.

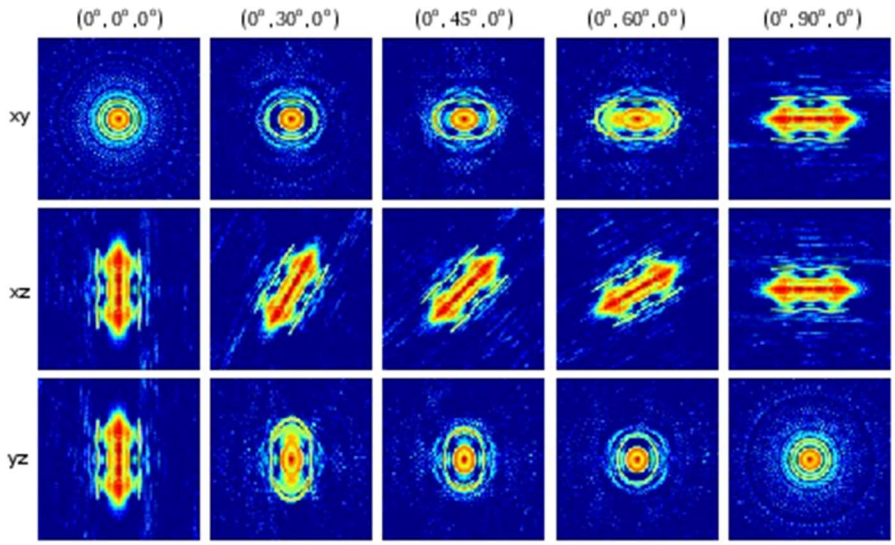

Figure 12: MIP images for an aluminum pipe are displayed for several Euler angle rotations. Each image is normalized by the maximum voxel. The color scale is 0 to -20 dB.

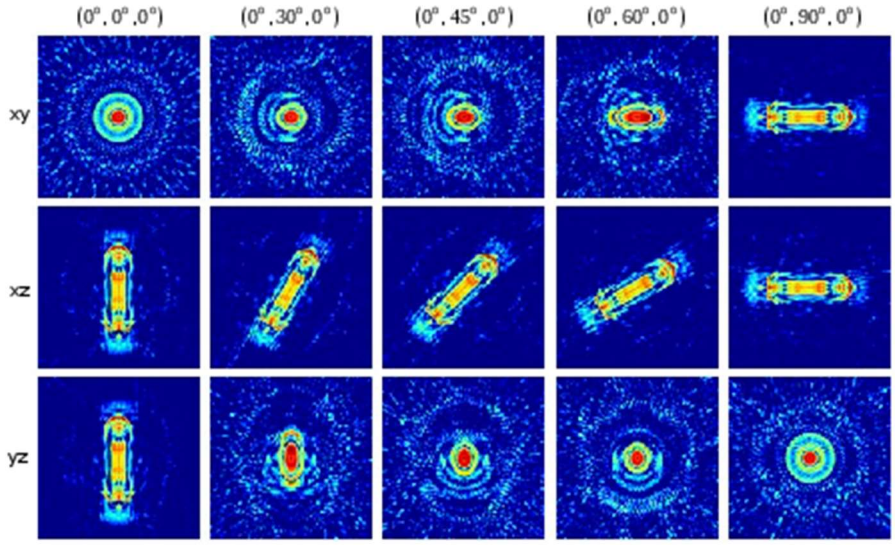

Figure 13: MIP images for an stemless scuba tank are displayed for several Euler angle rotations. Each image is normalized by the maximum voxel. The color scale is 0 to -20 dB.

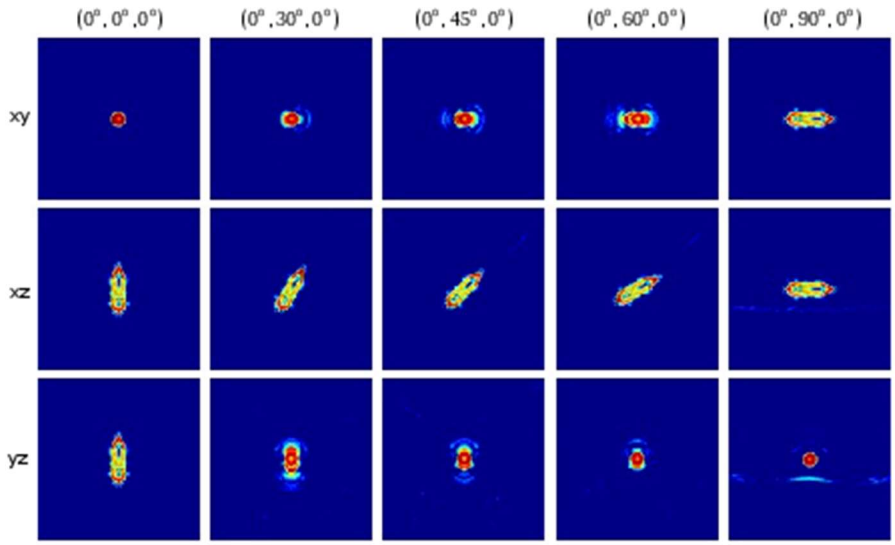

Figure 14: MIP images for an aluminum replica of a 100-mm UXO are shown. The color scale is 0 to -20 dB for normalized images.

4 Multiple Scattering

During CLUTTEREX17, data were collected from several objects, which were distributed in an approximate 40×40 m^2 area of the sea floor. Minimum separation distances between an object and nearby clutter were on the order of 1 m. Figure 15 shows a diver measuring the distance between a 2:1 aluminum cylinder and cement block. SAS images and acoustic color (AC) templates are displayed in Fig. 16 for this pair of objects. Although not clearly evident in the SAS images, comparisons of other SAS images with diver-recorded video surveys found features in SAS images where no objects could be identified. An application of either synthetic aperture decomposition [22] or quasi-holographic processing [23] allows isolation of the portion of the sonar signals that contributed to the SAS images. The isolated signals are converted into the AC templates in Fig. 16. Inspection of the regions within the red boxes reveal a periodic structure when the cement block was present. This structure is indicative of sound scattered by an object interacting with a neighboring object. Thus, an assumption of isolated objects no longer holds, and the TIER model needed to be updated.

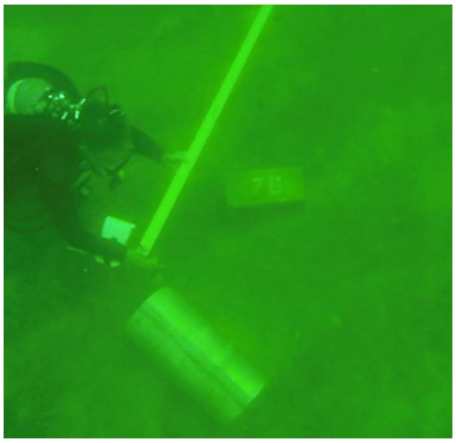

Figure 15: Divers performed routine surveys of deployed objects during CLUTTEREX17.

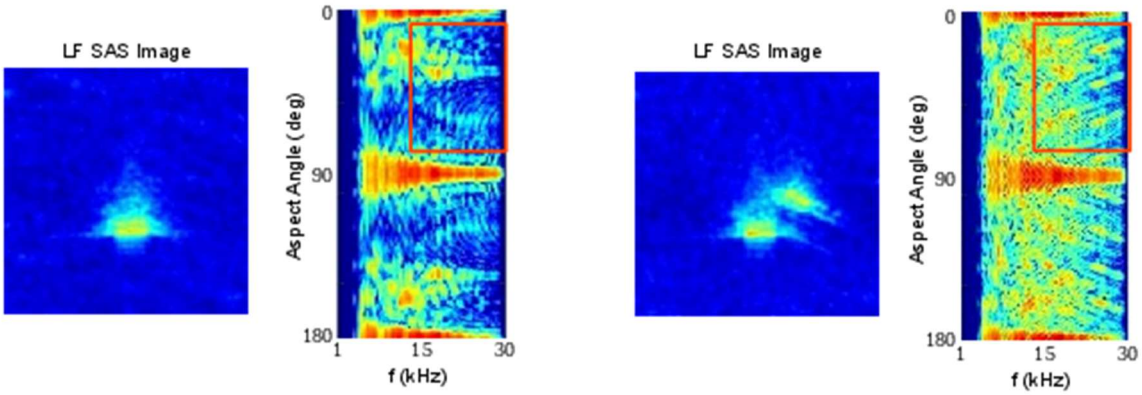

(a) Aluminum cylinder (b) Aluminum cylinder and block

Figure 16: (a) LF SAS image and AC template for an isolated 2:1 aluminum cylinder are displayed. (b) LF SAS image and AC template for a 2:1 aluminum cylinder with a nearby cement block are displayed.

An initial investigation into multiple scattering from deployed objects requires modification to the TIER model. The free-field model described in Sec. 2.1 is utilized in the development of a method to handle multiple scattering. When sound from the ith source interacts with the kth object, a portion of that sound can be directed towards the jth receiver. From Eq. (1), we write

$$P_k = r_0 P_{src}\left[B_s(\hat{d}_{ik})\frac{\exp(i\omega t_{ik})}{d_{ik}}\right] s(\hat{d}_{ik},\hat{d}_{kj})\left[B_r(\hat{d}_{kj})\frac{\exp(i\omega t_{kj})}{d_{kj}}\right] \tag{21}$$

with the ray diagram $S_i \to T_k \to R_j$. The notation slightly differs here from that in Sec. 2.1, because we need to track interactions with neighboring objects. The distance from the ith source to kth object is $d_{ik} = |\boldsymbol{r}_{tk} - \boldsymbol{r}_{si}|$, and likewise $d_{kj} = |\boldsymbol{r}_{rj} - \boldsymbol{r}_{tk}|$ is the distances from kth object to the jth receiver. In the absence of interactions between objects, the lowest order (or first-order) multiple scattering is simply a summation of all individual contributions: $P = \sum_k P_k$.

To account for possible multiple scattering effects, the scattering amplitude is replaced by an *effective* scattering amplitude such that Eq. (21) becomes

$$P^{(n)} = r_0 P_{src}\left[B_s(\hat{d}_{ik})\frac{\exp(i\omega t_{ik})}{d_{ik}}\right] s^{(n)}s(\hat{d}_{ik},\cdots,\hat{d}_{lj})\left[B_r(\hat{d}_{lj})\frac{\exp(i\omega t_{lj})}{d_{lj}}\right] \tag{22}$$

where the superscript (n) with $n > 0$ denotes the order of multiple scattering. The first argument in $s(n)$ indicates the sound from ith source interacts with the kth object while $\hat{d}_{lj}$ indicates sound scattered by the lth object is directed to the jth receiver. In Eq. (22), $\cdots$ represents possible interaction with other nearby objects. Finally, if objects are sufficiently isolated from each other, then $n = 1$ and Eq. (22) reduces to Eq. (21) with a spectrum for the total scattered pressure of $P = \sum_k P_k$.

Second-order multiple scattering has $n = 2$ and involves two objects. The ray diagram is then modified to include the propagation from the kth object to lth object such that one has $S_i \to T_k \to T_l \to R_j$. It is assumed that pressure scattered by a portion of the kth object does not interact with

any other portion of the kth object. Or, if there is a self-interaction, it is incorporated within the scattering amplitude for that object in isolation. This then implies the condition $k \neq l$ when summing all contributions to the total scattered pressure. For second-order multiple scattering, Eq. (22) becomes

$$P_{kl}^{(2)} = r_0 P_{src} \left[B_s(\hat{d}_{ik}) \frac{\exp(i\omega t_{ik})}{d_{ik}} \right] s^{(2)} s(\hat{d}_{ik}, \hat{d}_{kl}, \hat{d}_{lj}) \left[B_r(\hat{d}_{lj}) \frac{\exp(i\omega t_{lj})}{d_{lj}} \right] \quad (23)$$

$$= r_0 P_{src} \left[B_s(\hat{d}_{ik}) \frac{\exp(i\omega t_{ik})}{d_{ik}} \right] s(\hat{d}_{ik}, \hat{d}_{kl}) \frac{\exp(i\omega t_{kl})}{d_{kl}} s(\hat{d}_{kl}, \hat{d}_{lj}) \left[B_r(\hat{d}_{lj}) \frac{\exp(i\omega t_{lj})}{d_{lj}} \right] \quad (24)$$

Unit vectors point long the direction of propagation. For example, the ith source and kth object have $\hat{d}_{ki} = (\boldsymbol{r}_{tk} - \boldsymbol{r}_{si})/d_{ki}$. When the pressure from the ith source is incident on the kth object, a portion of the scattered pressure is directed towards the lth object. The relevant scattering amplitude is $s(\hat{d}_{ik}, \hat{d}_{kl})$, and $s(\hat{d}_{kl}, \hat{d}_{lj})$ is the scattering amplitude that directs pressure from the lth object to the jth receiver. The propagation time delay between the kth and lth objects is $t_{kl} = d_{kl}/c_1$, and the geometric spreading $1/d_{kl}$ is only included in Eq. (24) if it exceeds 1 m. Finally, from Eq. (24), the total pressure is then a double summation over all objects $P = \sum_k \sum_{l \neq k} P_{kl}^{(2)}$.

The TIER model traces the time-of-flight of a wave packet along ray paths from a source to a receiver. It is convenient to consider ray diagrams instead of cumbersome mathematical expressions like Eq. (24). The four lowest orders of multiple scattering are then

$S_i \rightarrow T_k \rightarrow R_j$		1st order	(25)
$S_i \rightarrow T_k \rightarrow T_l \rightarrow R_j$	$k \neq l$	2nd order	(26)
$S_i \rightarrow T_k \rightarrow T_l \rightarrow T_m \rightarrow R_j$	$k \neq l,\ l \neq m$	3rd order	(27)
$S_i \rightarrow T_k \rightarrow T_l \rightarrow T_m \rightarrow T_n \rightarrow R_j$	$k \neq l,\ l \neq m,\ m \neq n$	4th order	(28)

where each subscript is associated with a summation over the collection of objects with the restrictions noted in Eqs. (25)–(28). The restrictions exclude the possibility of self-scattering. Second and higher orders of multiple scattering inherently involve bistatic scattering (see Sec. 3). These orders have been included in the TIER model. Additional orders could be added, but the accumulation of propagation time delay places the higher-order multiple scattering contributions later in time, which means the contribution may be time-gated out.

The first interim report for SERDP MR19-1234 considered a collection of three point scatterers in the free field. These scatterers do not include an elastic response, so the SAS images and pulse-compressed signals allow one to associate observables with a particular order of multiple scattering. Those results are not repeated here. Although the formulation for multiple scattering was developed from the free-field model of Sec. 2.1, it can be easily extended to halfspace and waveguide models (Sec. 2.2). For multiple scattering from a collection of objects in a halfspace or waveguide, the subscripts i and j enumerate the physical sources and physical receivers as well as their images reflected through the water-sediment or air-water interface.

SAS simulation was constructed for two 2:1 solid aluminum cylinders sitting proud on the water-sediment interface. The TIER model utilized BSA tables constructed under the procedures described in Sec. 3.1. The source and receiver were scanned along the y-axis, and each aperture

had a 20×20 cm^2 surface area. The simulation also employed frequency dependent beam patterns (see Appendix C). The cylinders were placed at $T_1 = (10, 4.25, 0)$ m and $T_2 = (10, 5.75, 0)$ m in the global coordinate system. The orientation of T_1 had the axis of symmetry parallel to the y-axis, which gives a broadside orientation of 0°. Cylinder T_2 had a -45° pose with respect to broadside. Figure 17(a) displays pulse-compressed pings, when no interaction occurs between T_1 and T_2. The SAS image, constructed from those pings, is shown in Fig. 17(b). This result corresponds to the TIER model prior to the addition of multiple scattering. The pings in Fig. 17(a) contain sufficient structure that it is difficult to assign portions of the pings to one or the other cylinder. Spatial filtering can be applied to the complex SAS image to try to isolate the contributions from the pings to a specific object [22].

The second row in Fig. 17 introduced second-order multiple scattering, and it is evident in the SAS image that new observable structure appears near (10.5, 5) m. This structure is about 15 dB down from the peak response. The TIER model does not include reverberation (e.g., scattering from a rough sea floor), and so, this structure may not be observable in actual data. In additional, applying spatial filtering to the complex SAS image of Fig. 17(d) can potentially eliminate any contamination from the second-order component when preparing data products for a classification scheme. The third row in Fig. 17 now includes both second- and third-order multiple scattering. Third-order multiple scattering contributes easily identifiable structure in both the pings near (14.5 ms, 5.5 m) and SAS image near (11, 5.7) m. In particular the new observable in Fig. 17(f) is as strong as most of the TS of the isolated cylinder T_2 in Fig. 17(b). This observable also appears to overlap the response from T_2 and may not be easily removed. The last row in Fig. 17 includes fourth-order multiple-scattering, which appears to contribute little to the overall response.

In Sec. 3.2, the BSA were recast in terms of a golden spiral distribution of receiver locations on a spherical surface. Look-up tables for five objects were constructed, and the tables for the 2:1 solid aluminum cylinder (see Fig. 10) and 155-mm howitzer shell (see Fig. 11) were utilized in a sequence of multiple scattering simulations. The objects were placed proud on a water-sediment interface at a 15-m horizontal range from a linear SAS path. The TIER model simulated 1200 pings over a 30-m SAS aperture. Throughout the simulations, the cylinder maintained a broadside pose with its symmetry axis parallel to the SAS path in all simulations. The 155-mm shell is rotated through a series of poses. The separation distance between objects was 2 m (center-to-center). Figure 18(a) shows SAS images for simulations without multiple scattering (left panel, labeled with "No MS"), with multiple scattering through fourth order (center panel, labeled with "MS"), and the right panel is the "difference" to isolate multiple scattering observables. The sub-captions in Figs. 18(a)–18(g) are the Euler angle rotations applied to the 155-mm shell. All images are normalized to same 0 to -40 dB color scale.

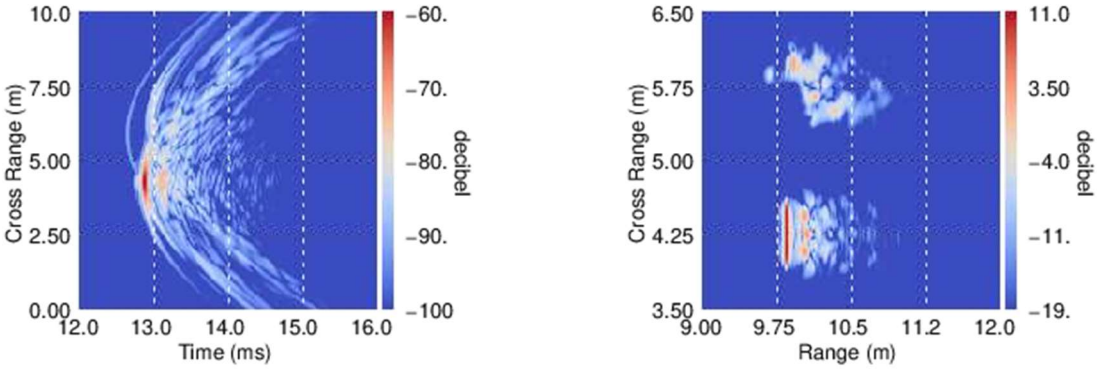

(a) Pings for 1st order

(b) SAS image for 1st order

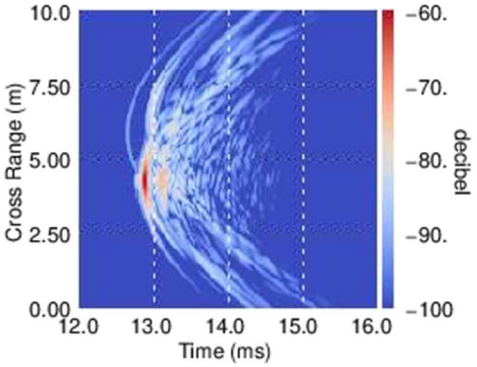

(c) Pings for 2nd order

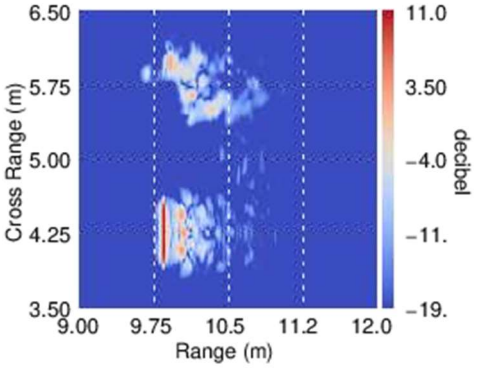

(d) SAS image for 2nd order

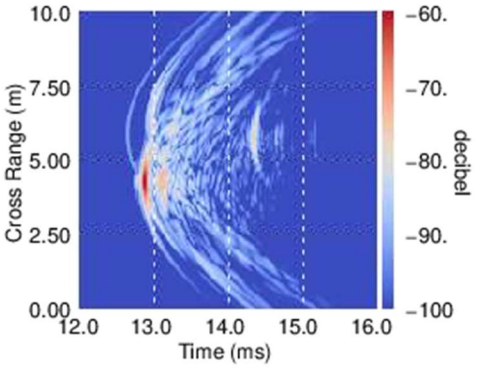

(e) Pings for 3rd order

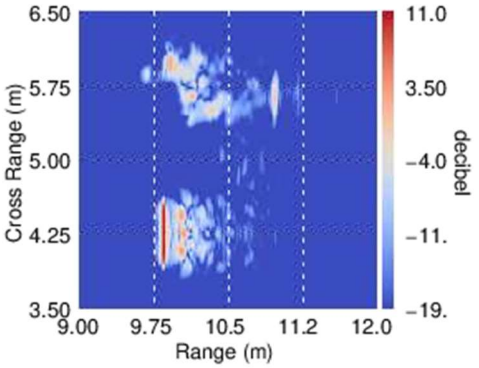

(f) SAS image for 3rd order

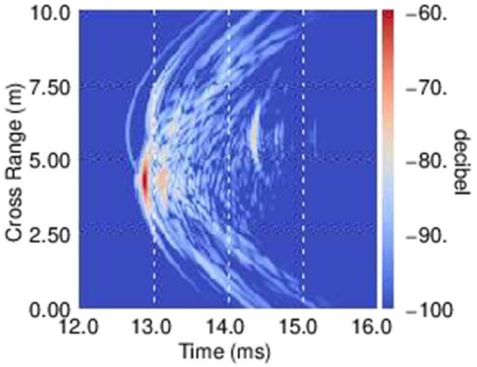

(g) Pings for 4th order

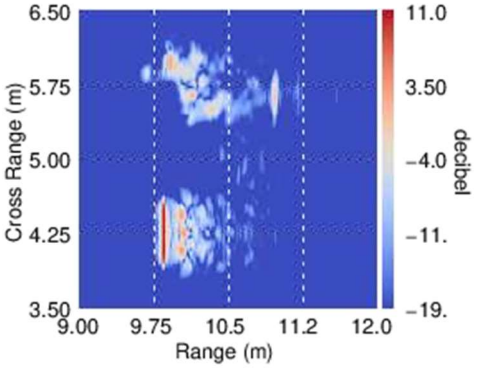

(h) SAS image for 4th order

Figure 17: Magnitude of the pulse-compressed pings and SAS images created from the pings are depicted for two aluminum cylinders.

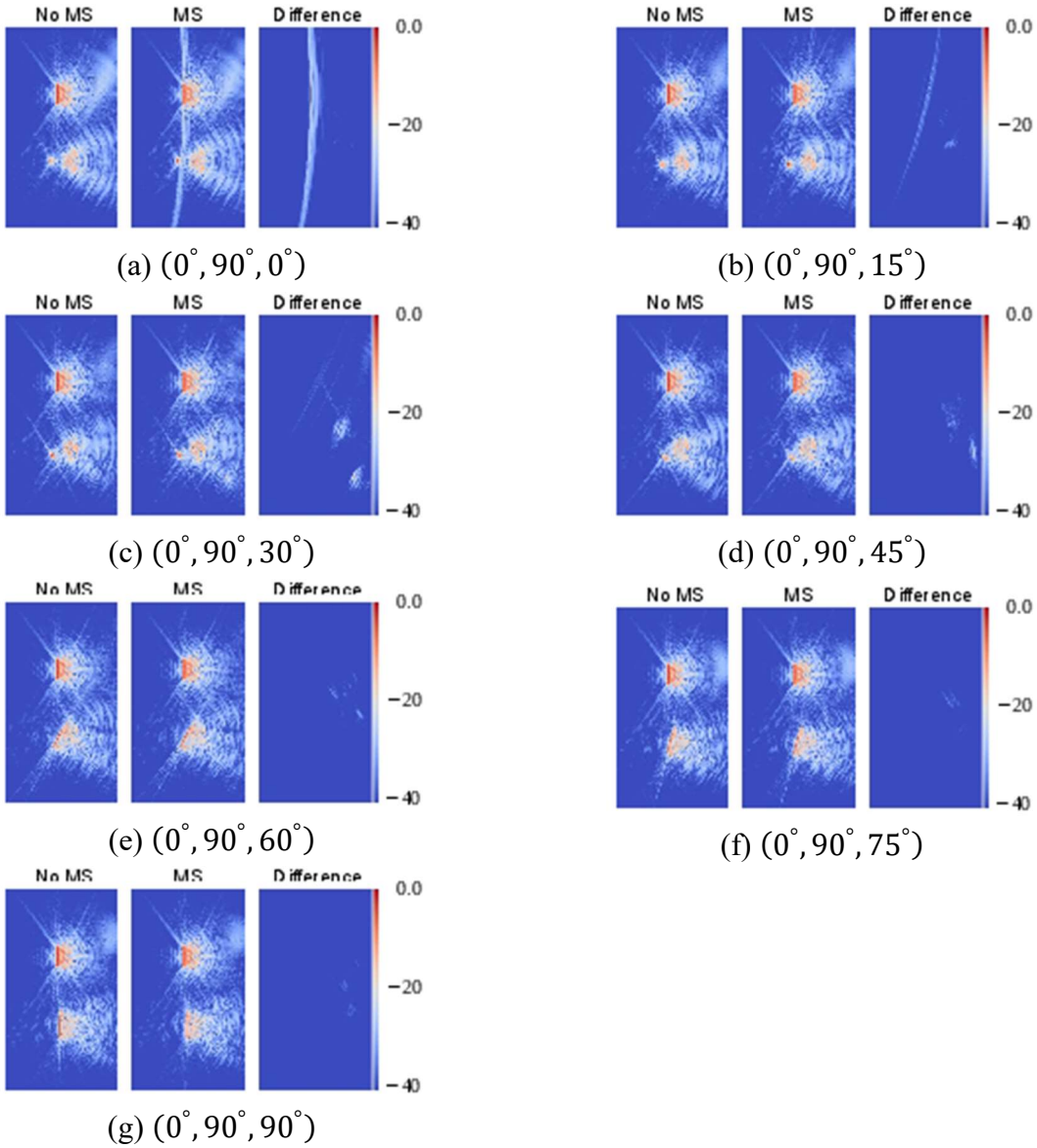

Figure 18: SAS images of a 2:1 aluminum cylinder and 155-mm howitzer shell with and without multiple scattering effects are shown along with the difference to accentuate the interaction between objects. BSA used in simulations were based on the golden spiral.

5 Replacement of Straight Rays via BELLHOP

Since 2013, APL-UW has collected acoustic scattering data from objects during several at-sea experiments. For any given experiment, APL-UW was on-site for multiple days. Each day, prior to any other scheduled activities, the water's conductivity and temperature were measured as a function of depth (a CTD measurement). The CTD data can then be converted to a local sound speed and density. Measured sound speed profiles (SSP) are displayed in Fig. 19. Major weather events would necessitate a temporary absence from a site. The colors in Fig. 19 separates the SSP into groups prior to a major weather event (red) and post event (blue). The green lines in Figs.

19(a) and 19(c) are the measurements conducted on the first day after returning to a site. A consequence of a weather event is a mixing of the water column, which yields a fairly uniform SSP. However, in general the SSP contains complicated structure, which will cause an acoustic ray path to deviate from a straight line. For our rail experiments, the source and receiver are ≈ 3.8 m above the sea floor. The designed and desired stand-off distance from the sea floor of the MuST is 5 m. Inspection of the SSP for BAYEX14 in Fig. 19(b) reveals a strong knee near a 3-m depth, close to the mid-column. If a sonar platform is above this knee, refraction of sound across the sound speed gradient may compromise the efficiency of a sonar platform.

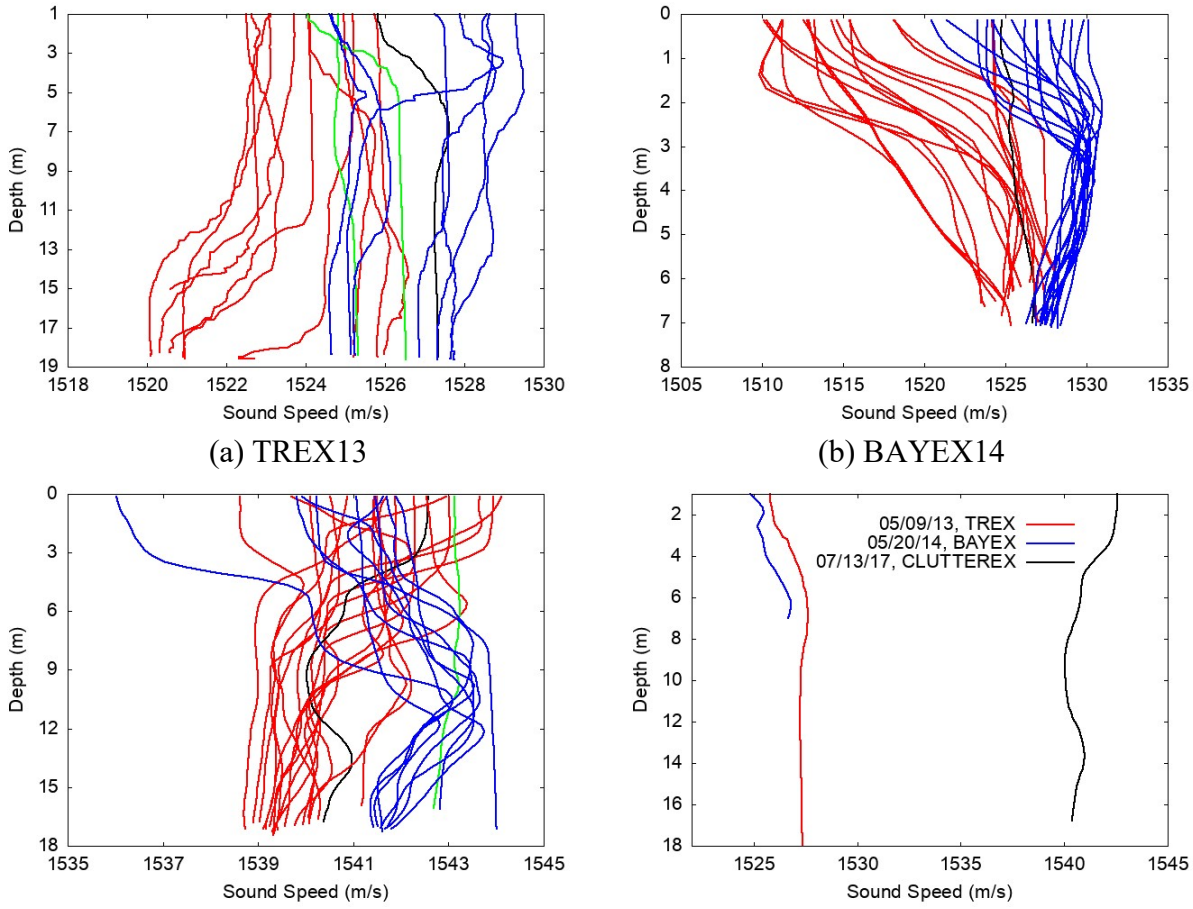

(a) TREX13 (b) BAYEX14

(c) CLUTTEREX17 (d) Black lines from (a)-(c)

Figure 19: The SSP was measured at least once per day during TREX13, BAYEX14, and CLUTTEREX17. The lowest depth in (a)–(c) coincides with the sea floor.

From Sec. 2, the direct path consists of a ray path connecting the ith source with the kth object $(S_i \rightarrow T_k)$. A second ray path connects the kth object with the jth receiver $(T_k \rightarrow R_j)$. A ray path that connects two points, A and B, within a waveguide is an eigenray [24, Ch. 3.7.5]. BELLHOP is a model that propagates rays through a horizontal stratified environment such that the SSP can vary with depth. One feature of BELLHOP is its ability to effectively find eigenrays (if one or more exists for the two points). Due to its robust implementation, instead of explicitly solving for eigenrays, it transmits a fan of rays from launch point A and then iterates over the rays searching for pairs that bracket the arrival point B. The search criteria include both the propagation time

delay of each ray should be nearly equal and the pair of rays have minimum perpendicular distances above and below point B [see Fig. 20(c) below]. The angular width of the fan determines the number of pairs of rays isolated. The number of rays within the fan determines the resolution.

For a homogeneous waveguide, the spectrum of total pressure is gmiven in Sec. 2.3 by Eq. (6). To use results from BELLHOP, Eq. (6) is rewritten as

$$P_B = r_0 P_{src} \sum_{m=0} \sum_{n=0} A_m e^{i\phi_m + i\omega\tau_m} s(\alpha_m, \beta_n)\, A_n e^{i\phi_n + i\omega\tau_n} \tag{29}$$

where the m subscript enumerates the eigenrays for source-to-object transmission. Note, ω is suppressed in Eq. (29) except in the time-delay phase factor. The magnitude and phase of the complex amplitude for the mth ray are A_m and ϕ_m, respectively. These quantities accumulate geometric and ray-tube spreading, reflection coefficients from boundaries, and possibly phase shifts due to a ray passing through one or more caustics. The accumulated propagation time delay is τ_m and α_m is an impact angle at an object location. By convention, BELLHOP measures an angle from the horizontal with a positive (negative) angle pointing downward (upward). Likewise, the subscript n enumerates the same quantities for object-to-receiver rays except β_m is related to a launch angle at an object. As implemented, the eigenray feature of BELLHOP does not directly provide A_m, ϕ_m, τ_m, and α_m although these quantities are computed. Fortunately, the software implementation [2] is available and modifications have been made.

To test BELLHOP a linearly increasing SSP was created. The near-surface sound speed was 1530 m/s and the near-bottom sound speed was 1535 m/s. The sediment properties were set to those of TREX13 ($c_2 = 1694$ m/s and $\rho_2 = 1800$ kg/m^3) while an 8-m water depth was selected to match BAYEX14. It is noted that the TIER model places the origin of its coordinate system in the water-sediment interface with the $+z$-axis pointing upward; while the origin for BELLHOP is in the air-water interface with the $+z$-axis pointing downward. With this consideration, the source and object locations are specified in terms of water depth: $A = (0, 0, 4.2)$ m and $B = (15, 0, 7.8)$. The shallow water depth and horizontal range from A to B suggest that rays reflecting from the air-water interface may become important. To capture three pairs of rays that correspond to the direct ray, single bottom bounce, and single surface bounce, a ray fan was set to have launch angles such that $-39^\circ \leq \alpha \leq 20^\circ$. The number of transmitted rays within the fan was changed from a few hundred to > 10000 during testing. Figure 20 shows eigenrays with an angular increment in the fan of $\Delta\alpha = 0.0059^\circ$. To achieve sufficient resolution along a ray, the spatial step in horizontal range was $\Delta R = 0.025$ m. Finally, the frequency of the transmitted rays is set to 16 kHz, which matches the carrier frequency of the LFM pulse transmitted by the APL-UW sonar.

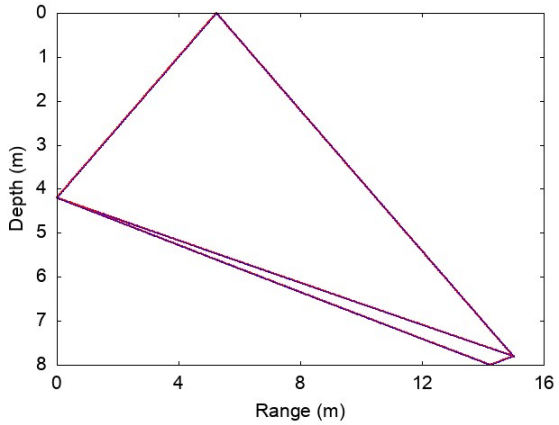

(a) Full range to receiver location

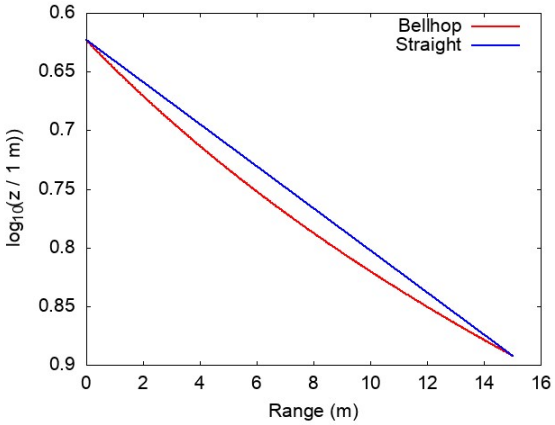

(b) Logarithm of the direct path

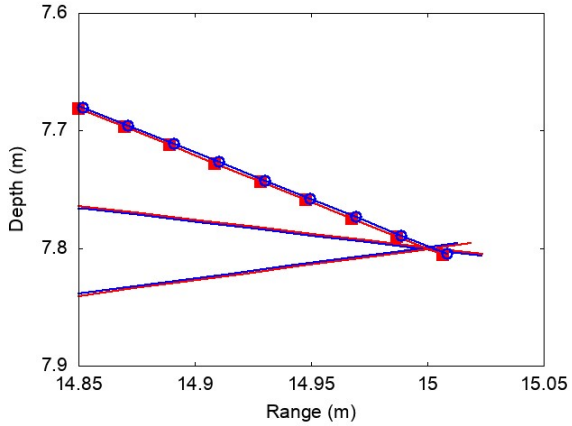

(c) Close up of the direct arrivals

Figure 20: (a) Pairs of rays that can reach an object with at-most one interaction with a waveguide boundary. (b) Logarithm of the direct ray path compared to a straight-line. (c) Close up of rays that pass closest to the receiver location.

Inspection of Fig. 20(a) reveals three pairs of rays within the waveguide for the specified ray fan. The first two entries in Table 4 are the pair of rays reflected from the air-water interface. The next two entries are the direct rays that interact with neither interface. The last two entries correspond to the rays that reflect once from the water-sediment interface. The deviation between a straight ray path and one of the rays from the pair for the direct path is depicted in Fig. 20(b). The ordinate is log10(z/1 m). It is observed that the distance along the BELLHOP ray exceeds the distance along the straight ray. However, due to sound speed increasing with depth, the ray predicted by BELLHOP arrives at the object in $\tau = 10.058$ ms, which is earlier than $t = 10.082$ ms for a straight-line ray in a homogeneous fluid with $c_1 = 1530$ m/s. The difference in arrival times is $\Delta t \approx 0.024$ ms. With a wavelength at the carrier frequency of $\lambda \approx 0.096$ m, the accumulated phase advance yields $c_1 \Delta t \approx 0.38\lambda$. Thus far, only propagation from the source to object has been considered. For co-located source and receiver, the object-to-receiver ray paths are reciprocal and are those shown in Fig. 20(a). Under this condition, the overall path-length difference for the direct ray approaches 0.76λ. If the source and receiver are not co-located, then BELLHOP would need to be run again to determine eigenrays for object-to-receiver propagation.

With a sonar platform sweeping past an object, deviations in the path-length difference may lead to defocusing or aberrations in images from coherent SAS processing.

θ (deg)	τ (ms)	A	ϕ (deg)	α (deg)
-38.634	12.539	0.1539	180.0	38.529
-38.628	12.539	0.0482	180.0	38.523
13.669	10.058	0.1585	0.000	13.318
13.675	10.058	0.0926	0.000	13.324
15.103	10.121	0.1179	72.67	-14.788
15.108	10.121	0.1313	72.64	-14.794

Table 4: The launch angle at the source location is θ. The other displayed quantities are defined following Eq. (29) above.

Returning to Table 4, the quantities that appear in Eq. (29) need to be selected. The arrival time, τ, of the rays within a pair are the same to microsecond accuracy. For ϕ and α, simply averaging the recorded values seems to be a good choice as the true eigenray lies between these values. For A, averaging may adversely affect the amplitude. For example, the first pair of rays, which interact with the air-water boundary, have $A = 0.1539$ and 0.0482. The straight ray model of TIER assumes a ray has essentially zero width; whereas BELLHOP includes a finite width for a ray and tracks its evolution as the ray propagates. For the rays in Fig. 20(a), the finite width is specified to have a Gaussian shape centered on the ray. Thus, selection of the largest A is preferred.

The preceding discussion concerns the identification of eigenrays, and does not address an actual simulation of a received sonar signal. The TIER model was modified to interact with BELLHOP. Given a scattering geometry, description of an inhomogeneous environment, and the number of desired eigenrays, the TIER model generates an input file for BELLHOP (e.g., for $S \rightarrow T$) and then executes BELLHOP, which generates an output file containing a table of A, ϕ, τ, and α values. (A table is likewise generated for $T \rightarrow R$.) After execution, the TIER model reads these tables to finally compute Eq. (29). The original waveguide implementation in Sec. 2.3 is designed to include a specified number of sources, receivers, and number of contributions to include in Eq. (6), which are denoted by N_s, N_r, and $N \leq N_s N_r$, respectively. If $N < N_s N_r$, the ordering is determined from an enumeration that prioritizes the receiver over the source irrespective of time-of-flight. For example, if $N_s = 2$ and $N_r = 3$, the ordering $(S_i, R_j) = (S_0, R_0)$, (S_0, R_1), (S_0, R_2), (S_1, R_0), (S_1, R_1), and (S_1, R_2), and $N = 4$ yields a superposition of $(S_0, R_0) + (S_0, R_1) + (S_0, R_2) + (S_1, R_0)$.

For a meaningful comparison, the linearly increasing SSP of the previous example was modified to have near-surface and near-bottom sound speeds of 1530 m/s and 1530.1 m/s (i.e., a nearly isotropic environment). A point object was placed at $B = (15, 0, 7.85)$ m and collocated point source/receiver are at $A = (0, 0, 3)$ m. The source transmitted a 1-ms duration sine-wave tone burst with a 16-kHz carrier frequency. The BELLHOP model was requested to include 16 eigenrays while the waveguide model within the TIER model used $N_s = N_r = 4$ and $N = 1$, 4, 8, and 16. Figure 21 shows the scattered signals in a 9-ms window. The leading arrival includes the

direct ray path $S_0 \rightarrow T_0 \rightarrow R_0$, which is shown in isolation in Fig. 21(a). With $N = 4$ (i.e., four paths), one might anticipate that the scattering coincides with the halfspace environment of Sec. 2.2, but only the $S_0 \rightarrow T_0 \rightarrow R_0$ and $S_0 \rightarrow T_0 \rightarrow R_1$ paths from Sec. 2.2 are included by the truncation in N. The other two paths are associated with image receivers above the air-water interface. This then means a portion of the second pulse in Fig. 21(b) is included by Eq. (6). With $N = 8$, all ray paths for the halfspace model in Sec. 2.2 are now included, and the first pulse is resolved. When $N = 16$, all possible combinations of $S_i \rightarrow T_0 \rightarrow R_j$ are included, and one sees substantial agreement between BELLHOP and original waveguide simulations in Fig. 21(d).

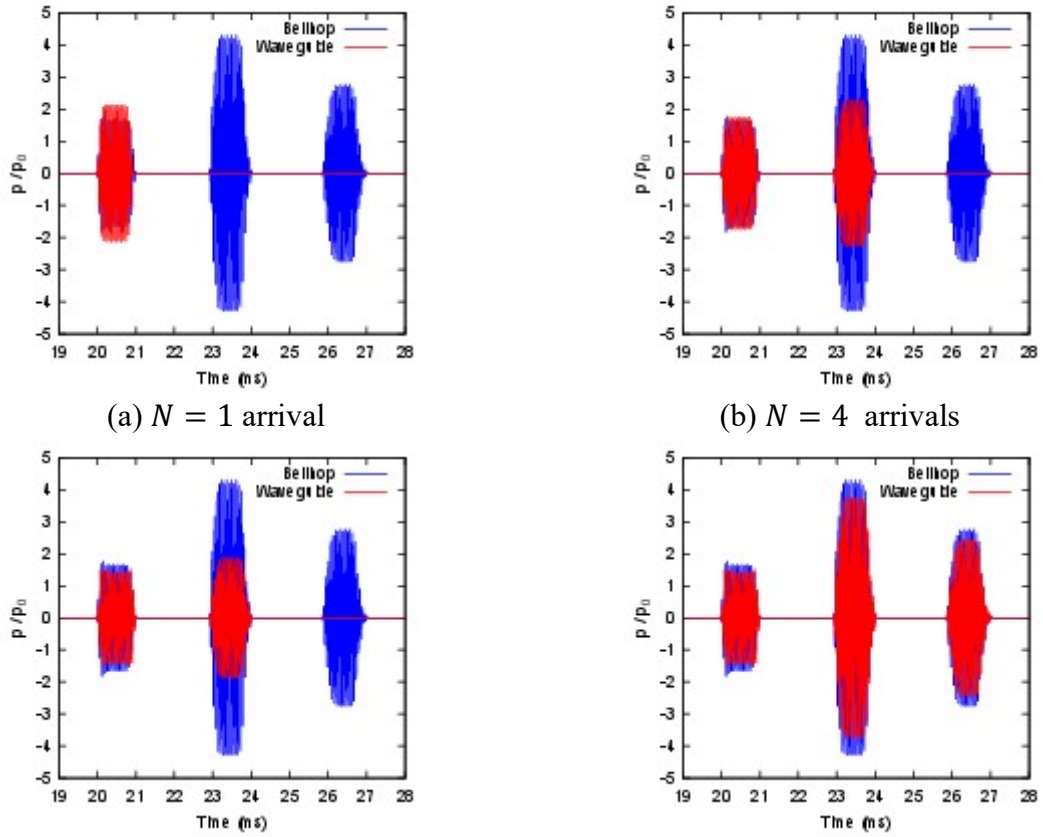

(a) $N = 1$ arrival (b) $N = 4$ arrivals

(c) $N = 8$ arrivals (d) $N = 16$ arrivals

Figure 21: Comparison on the results from Eqs. (29) and (6) are depicted where the number of contributions in Eq. (6) has been limited as indicated in the sub-captions.

Figure 22 repeats the $N = 16$ result, and also includes close-up depictions of short 2-ms windows about the three returns. Two important observations follow. First, the arrival times and phases for the pulses agree in Figs. 22(b)–22(d). This suggests that the desired integration of BELLHOP within the TIER model framework has been accomplished. Second, the BELLHOP pulses seem to be slightly larger in amplitude than the original waveguide model in Sec. 2.3. BELLHOP tracks acoustic energy transport along a ray tube, and the evolution of a ray tube in horizontal range may provide a better estimate of an amplitude of a ray than Sec. 2.3. It is, however, noted that the difference is on the order of only 1 dB.

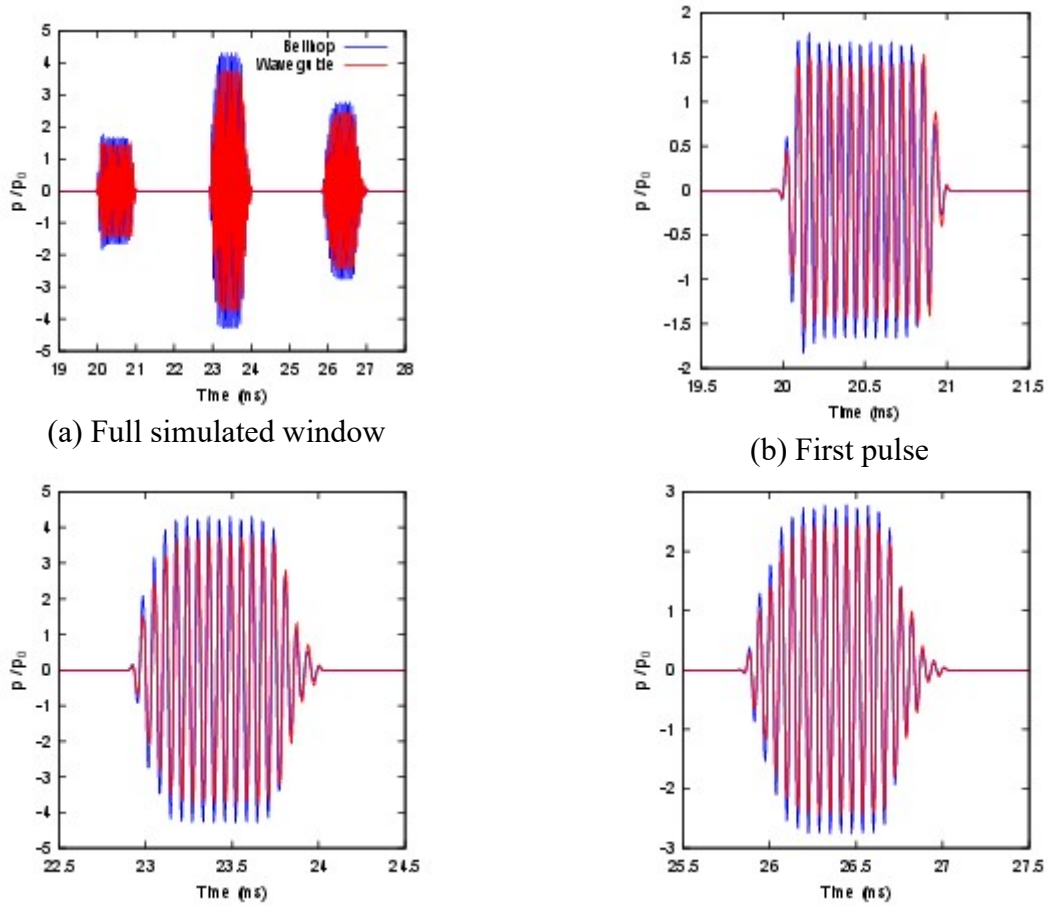

(a) Full simulated window

(b) First pulse

c) Second pulse

(d) Third pulse

Figure 22: Comparison on the results from Eqs. (29) and (6) are depicted where the number of contributions in Eq. (6) has been limited as indicated in the sub-captions.

6 Reverberation from small-scale surface roughness

The sound scattered from small-scale surface roughness on a water-sediment interface is a primary contribution to reverberation (i.e., background noise). Other contributions to reverberation include noise associated with ships, wind-driven surface waves, volume scattering from inhomogeneities within the sediment, and scattering from fish school or biomass in the water column. Only the reverberation due to small-scale surface roughness is considered here, and is denoted by p_{rev}.

First-order perturbation theory was used to model time-domain reverberation from a rough sea floor. A derivation of this model is given in [4, Appendix A]. Several approximations are employed in addition to first-order perturbation theory: stationary phase approximation is used to evaluate the zero-order field needed for the first-order theory, properties of the water and sediment are the same as those used in Sec. 2, and the source and receive beam patterns are frequency independent. The latter approximation is reasonably satisfied for APL-UW experiments, because the horizontal aperture of the four-element source is steadily reduced as the frequency is increased by reducing the number of active elements from four down to one in steps (see Sec. C and Fig.

C1). In addition, the two sources on the MuST platform are omni-directional. The contribution to reverberation from a rough sea floor reduces to an integral over the mean sea floor (i.e., $z = 0$).

$$p_{rev}(\boldsymbol{R}_r, t) = \frac{r_0}{4\pi c_1^2} \int d^2R \frac{A_{rev}(\boldsymbol{R}) h(\boldsymbol{R}) \ddot{p}_s(t - t_r)}{|\boldsymbol{R}_r - \boldsymbol{R}||\boldsymbol{R} - \boldsymbol{R}_s|} \tag{30}$$

As in Sec. 2, $r_0 = 1$ m preserves dimensional consistency. In Eq. (30), subscripts rev, s, and r denotes quantities related to reverberation, a source, and a receiver, respectively. Environmental and system parameters enter through

$$\begin{aligned} A_{rev}(\boldsymbol{R}) = B_s B_r \{ & [1 + L(\theta_i)][1 + L(\theta_s)](1 - \kappa^2/\rho) \\ & + (\rho - 1)[1 - L(\theta_i)][1 - L(\theta_s)] \sin\theta_i \sin\theta_s \\ & + (1 - 1/\rho)[1 + L(\theta_i)][1 + L(\theta_s)] \cos\theta_i \cos\theta_s \cos\phi \} \end{aligned} \tag{31}$$

Source and receiver beam patterns, B_s and B_r, are evaluated on the $z = 0$ mean interface. In [4], these are evaluated at the carrier frequency of the transmitted sonar signal. Appendix C investigates the relaxation of a constant-frequency requirement in a beam pattern. The flat-interface reflection coefficient, $L(\theta)$, is given by Eq. (3) with the grazing angles determined from $\sin\theta_i = z_s/|\boldsymbol{R} - \boldsymbol{R}_s|$ and $\sin\theta_s = z_r/|\boldsymbol{R}_r - \boldsymbol{R}|$. The horizontal positional vector $\boldsymbol{R}$ is defined in Sec. 2.2 following Eq. (2) with $\boldsymbol{R}$ being the horizontal vector to some point of the mean interface. The angle between the incident and scattered wave vectors is ϕ with $\phi = 0^\circ$ in the forward direction and $\phi = 180^\circ$ for backscatter. The local height of the sea floor relative to the mean plane is $h(\boldsymbol{R})$, and $p_s(t)$ is the time-domain pressure at 1 m from the source along its acoustic axis. The second partial time derivative is denoted by a double-dot notation above an entity. Finally, the round-trip time delay to propagate from the source to a point on the mean interface and then back to the receiver is $t_{rev} = (|\boldsymbol{r}_r - \boldsymbol{r}||\boldsymbol{r} - \boldsymbol{r}_s|)/c_1$.

The numerical implementation of Eq. (30) has been updated to use the global coordinate system of the TIER model. An example computation for reverberation considered a surface height associated with isotropic small-scale roughness, which is described by the following power law [4]:

$$W(k_x, k_y) = \frac{w_2}{(k_s^2 + k_c^2)^{\gamma_2/2}} \tag{32}$$

The spatial wavenumber for the surface is $k_s^2 = k_x^2 + k_y^2$ with Cartesian components k_x and k_y. Equation (32) cuts off the wavenumber spectrum at k_c. Figure 23(a) shows the magnitude of the surface relief generated with $w_2 = 0.0016$ m$^{4-\gamma_2}$, $\gamma_2 = 3.82$, and $k_c = 20.9$ m^{-1} (i.e., at a 0.3-m length scale), which fall into the range of values for a medium-fine sand sediment.

To compute Eq. (30), the double integral is transformed into discrete sums over the mean surface coordinates $\boldsymbol{R}_{m,n} = (m\Delta x, n\Delta y)$. The resolution of Δx and Δy need to satisfy the Bragg scattering conditions $\Delta x < \lambda/4$ and $\Delta y < \lambda/4$ to suppress artifacts. Here, λ is the smallest wavelength of interest in the spectrum of the transmitted sonar signal. In APL-UW experiments,

the upper frequency was 30 kHz, which gives $\lambda \approx 5$ cm. For Fig. 23(a), Δx and Δy were set to 1 cm, which means the discrete sums represents 1.5 million surface points, and by extension 1.5 million evaluations of Eq. (31). For co-located source and receiver placed at (25,0,5) m with a 20° depression angle, the footprint of $B_s B_r$ on the surface relief is shown in Fig. 23(b). The large semi-circular edge is an event horizon associated with the maximum time of the computational window. Thus, $B_s B_r$ and time window allow a significant reduction in the number of evaluations of Eq. (31) (i.e., on the order of 50%).

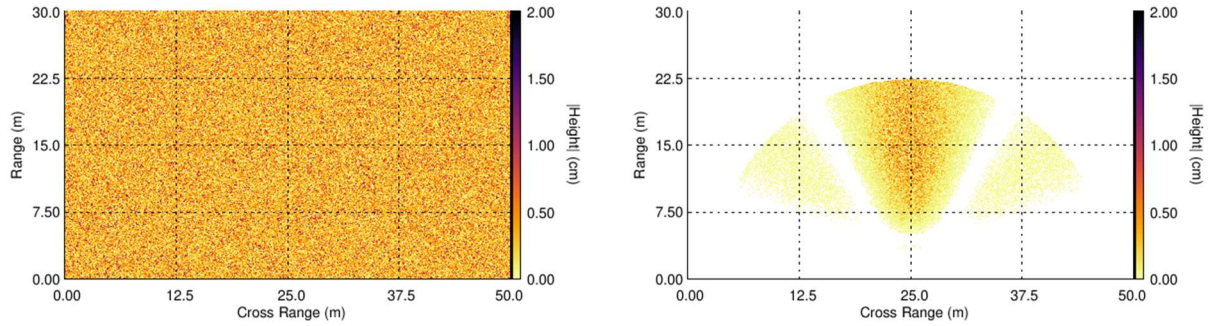

(a) Surface relief (b) Surface relief weighed by beam patterns

Figure 23: (a) Fourier transform methods allow generation of a random rough surface from Eq. (32). (b) $B_s B_r$ masks the surface relief and reduces the computational complexity.

Figure 24 depicts the transmitted signal and the real part of the reverberation compute from Eqs. (30) and (31). The transmitted signal is a tapered 6-ms 1–30 kHz LFM pulse sampled at 100 kHz (i.e., $\Delta t = 10^{-5}$ s), which is often used in the TIER model simulations of APL-UW experiments. With $t = 0$ corresponding to the start of the transmission, the simulation recorded reverberation in a 8-30 ms time window. As noted above, the semicircular edge in Fig. 23(b) is the 30 ms event horizon. That is, scattering from points on the surface beyond this edge do not enter into this time window. Combining the results for the TIER model, which computes only the scattering response of an object, and the reverberation model presented here allows one to simulation sonar platforms used in UXO remediation.

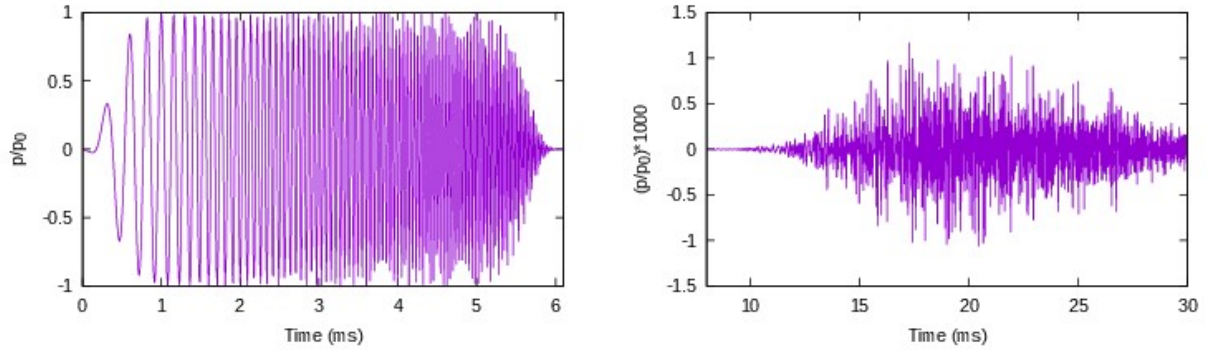

a) LFM Transmitted Signal (b) Real Part of Reverberation

Figure 24: (a) The source transmitted a 1–30 kHz LFM pulse. (b) The real part of the reverberation computed from Eq. (30) with the surface shown in Fig. 23.

Inspection of Eq. (30) shows that this formulation of small-scale rough surface scattering has a limitation. The integrand is singular for points on the surface below a source or receiver. Hence, a small patch enclosing the singular point is excluded. This is tantamount to selecting the initial time of recording a scattered signal large enough to exclude contributions from the patch.

7 Scattering from Thin Lines

At the 2020 ESTCP & SERDP symposium, a session was devoted to development and use of underwater UXO test sites. In controlled at-sea measurements, it was recognized that deployed objects must be registered to ground-truth GPS coordinates and tethered to prevent transport of an object due to local currents and for recovery. To aid in this task, divers often insert lines (i.e., lightweight cords), which can interact with the transmitted sonar signal. Many, if not all, sonar systems currently under development for UXO remediation use labeled sonar data to train classification schemes. It has been suggested that unintended sonar detections of these lines may influence or compromise classification. In particular, a sonar system under evaluation at an ESTCP test-bed site may leverage artifacts to attain a passing score during blind testing.

During CLUTTEREX17, divers installed a grid of cords with a 5-m spacing parallel to the APL-UW rail system to aid in the deployment of targets and clutter objects. Data were collected simultaneously within the 1–30 kHz LF band and 110–190 kHz HF band. Figures 25(a) and 25(b) display the SAS images generated from data sequence 54, where the objects are randomly distributed in an approximately 20×20 m^2 area. The colored images have a dynamic range of 40 dB. Four horizontal lines are clearly observed in the HF SAS image; while no such lines are visible in the LF SAS image. It is noted that the simultaneous transmission of the LF and HF bands facilitates spatial registration of the SAS images. As an aside, the HF image shows a sand ripple over the entire image while it appears as a speckle background in the LF image. The reverberation model in Sec. 6 was developed for this type of surface roughness and the LF band.

To investigate the question of whether a sonar system could exploit the interaction of its transmitted signal with lines used by divers in the deployment and recovery of target fields, a task was added to SERDP MR19-1234, and performed in collaboration with Dr. Raymond Lim (MR21-7211) [25], to measure the relative target strength of various line types. Acoustic scattering data were collected at the Acoustic Test Facility (ATF) at Naval Surface Warfare Center, Panama City Division over the period 14–25 June 2021. The ATF is a filtered and chlorinated freshwater facility. For the duration of the measurements, the temperature and sound speed of the water were nearly constant at 24.9 C and 1494 m/s, respectively.

7.1 Types of lines deployed

Five types of line were deployed in the ATF with the lines extending vertically from the water surface to the bottom of the facility, which has a nominal depth of 8 m. Figure 26 shows short segments of each deployed line. It is noted that Amsteel and 550 parachute cord are commonly used due to their light weight, high visibility, and strength. The dry weight of each sample in Fig. 26 was measured at APL-UW with a Mettler Toledo AL204 analytic balance. An Archimedes'

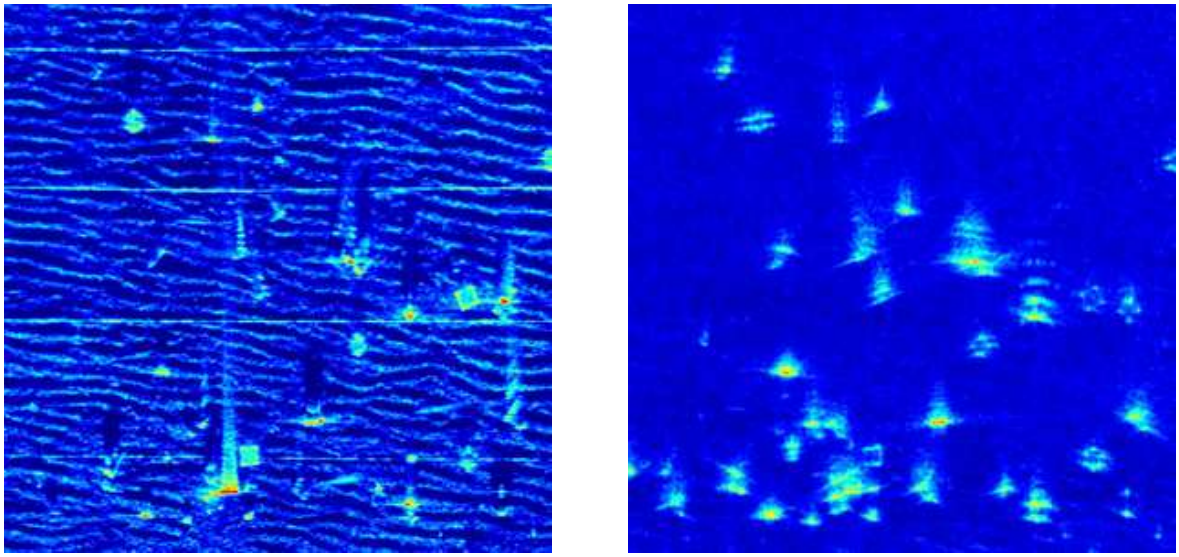

(a) HF SAS Image (b) LF SAS Image

Figure 25: (a) HF SAS image and (b) LF SAS image generated from CLUTTEREX17 data sequence 54. The sonar on the APL-UW rail system ran along bottom of the images.

principle measurement also was conducted, where the volume measurement was complicated due to the buoyancy of the lines. An additional weight was placed over each line to keep it submerged. Table 5 summarizes the measurements. No attempt was made to determine porosity of the lines nor were water-saturated weights determined. Inspection of Fig. 26 shows that the lines are formed from braiding strands of a much thinner material. The structure allows air to be trapped when placed in water. Acoustic scattering data were obtained from the lines with no special handling. In addition, data were collected after the lines were placed into a small chamber where a vacuum could be drawn. The lines remained in the chamber for at least an hour. Prior to a scattering measurements, degassed and saturated lines were transported from the vacuum in a bucket of water. That is, once degassed the lines had minimal exposure to air to prevent diffusion of air back into the inner structure.

Figure 26: (a) Amsteel from Samson Rope, (b) 550 parachute cord, (c) Polypropylene line, (d) Fibrous cotton rope, (e) braided fishing line (200-lb test). A ruler runs along the bottom of the image

Line	Dry weight (g)	Volume (ml)	Density (kg/m^3)
Amsteel	1.248	2.45	503.2
550 parachute cord	1.156	2.00	578.0
Polypropylene	2.699	3.95	683.2
Fibrous cotton	0.981	1.80	545.0
Fishing line	0.431	1.60	269.0

Table 5: Densities for the line segments shown in Fig. 26 were determined via a standard volumetric measurement. The nominal length of each is 0.1525 m except for the fishing line, which was 1.17 m.

7.2 Low frequency measurements

Standard US Navy transducers were used in measurements in the 10–50 kHz and 50–150 kHz frequency bands. The source was an F33 transducer, which contains two sections. In the lower frequency band, the sections were operated in parallel to increase effective aperture. Only the inner section was used for the upper frequency band. The receiver was a H52 reference hydrophone. The source and receiver were placed four meters below the surface (i.e., approximately mid-water column). The perpendicular distance from the F33 transducer to a line was 2.46 m. A monostatic measurement would require co-location of the source and receiver, which cannot be realized with two physical transducers. A backscattering experiment would place a receiver between the source and line with the receiver on the acoustic axis of the source. The result is either the received signal is saturated from a direct incident signal over-driving the electronics or the receiver shadows the line. To mitigate these issues, the H52 hydrophone was shifted off the acoustic axis by ≈ 0.3 m and placed forward of the F33 transducer. With no lines in the water, a quiet window was found in the received signal at approximately 2.6 ms after transmission. With $c_1 = 14941$ m/s, the stand-off distance of the source has an equivalent time delay of 1.65 ms. The time window and delay time of the source yield a stand-off distance of ≈ 1.42 m for the H52 hydrophone from the line.

Sine-wave tone bursts were transmitted during the experiments, where the tone bursts were not tapered. The carrier frequency was incremented from 10 kHz in 1 kHz steps up to 150 kHz. Below 50 kHz, a tone burst contained 5 cycles; while, above 50 kHz 10 cycles were used. The duration of a tone burst is of course determined by the number of cycles and frequency. One consequence of the untapered nature of the tone burst is that the sudden application of a signal to the F33 transducer could cause it to ring with a wider frequency response than in the tone burst. Data were also collected with LFM pulses. The LFM pulses had an 1-ms duration and shaped with 10% leading and trailing tapers to try to suppress a ringing response of the F33 transducer. The LFM measurements utilized two pulses where the pulses spanned the 10–50 and 50–150 kHz bands. Comparison of the relative target strengths of the tone-burst results and broadband LFM results allows one to assess whether a single LFM measurement can reduce the time required to measure the target strength across the full band with tone bursts.

At each frequency, scattered signals were collected. Initial testing with the braided fish line (see Fig. 26) suggested that any scattered LF signal would fall below the noise floor of the experimental set-up. Thus, the braided fish line was only deployed during HF measurements.

7.3 High frequency measurements

Standard US Navy transducers again were used in measurements within the 100–2000 kHz range. A pair of E37 transducers were employed as a source and receiver. The transmitter voltage response and receive sensitivity of the E37 transducers at 100 kHz were barely sufficient in recording data, but this frequency is common to the both the LF and HF measurements. The source and receiver were placed again 4 m below the air-water interfaces at mid-water column. For these measurements, the pair of E37 transducers were mounted in a fixture that allowed the acoustic axes of the beam pattern of the transducers to overlap at 1 m. The angular separation of the acoustic centers of transducers was estimated to be approximately 2.4°. The pair, in this configuration, nearly meet a monostatic requirement given the small angular separation, stand-off distance, and in particular the wavelength of sound. It is noted that the shorter stand-off distance for the high-frequency measurements was imposed by the relatively narrow beamwidth in the beam patterns at the upper frequencies and the effort required to align the experimental setup.

Both sine-wave tone bursts and LFM pulses were transmitted during the experiments. The tone burst contained 10 or more cycles and were not tapered. While the number of cycles varied in the HF tone-burst measurements, the frequency increment was fixed at 100 kHz. This was insufficient to adequately cover the full band of 100–2000 kHz due to the time available at the ATF; however, this gives 20 measurements that can be used to spot check the LFM pulse measurements. LFM pulses were transmitted with center frequencies of 150, 250, …, 1950 kHz with a bandwidth of 100 kHz in an attempt to span the 100–2000 kHz range. Finally, the LFM pulses were shaped with the same 10% taper of the LF measurements.

7.4 Data processing chain

The ATF is a barge centered in a small pond and held in-place by a four-point moor. On calm days, the mooring is sufficient to keep the barge from swaying from any fluctuations in the outside air. A measurement under these conditions could record a time-averaged scattered signal to reduce experimental noise in the system. However, over the 11-day planned experiment, calm conditions cannot be expected, so individual measured signals were saved to a computer for later processing.

After the LF and HF scattering data were collected from the lines, the receiver was placed on the acoustic axis of the source at the location of the lines in a pitch-and-catch configuration. Ten or more transmissions of each tone burst and LFM pulse were recorded as reference signals for data normalization. The reference signals allow for the removal of transmitter voltage response and receiver sensitivity from the scattered data. This, however, was a spot measurement on the acoustic axis of the source, and as such, it cannot compensate for any effects due to a transducer's beam pattern [26].

The basic processing chain can be summarized as follow. For a given measurement, N scattered signals or pitch-and-catch signals were collected. Henceforth, measured data are referred to as pings. Figures 27(a) and 27(d) show scattered pings for 25 and 100 kHz tone bursts. Each ping is transformed into the frequency domain and a window centered at the carrier frequency is applied to remove frequencies outside the band of interest. The fullwidth-at-half-maximum for a window is always selected to include the entire main response and possibly some or all of the first sidelobe. Testing showed that the choice of window (Hann, Hamming, or Tukey) had little effect on results. Figures 27(b) and 27(e) use a Tukey window with a default parameter of $\alpha = 0.25$.

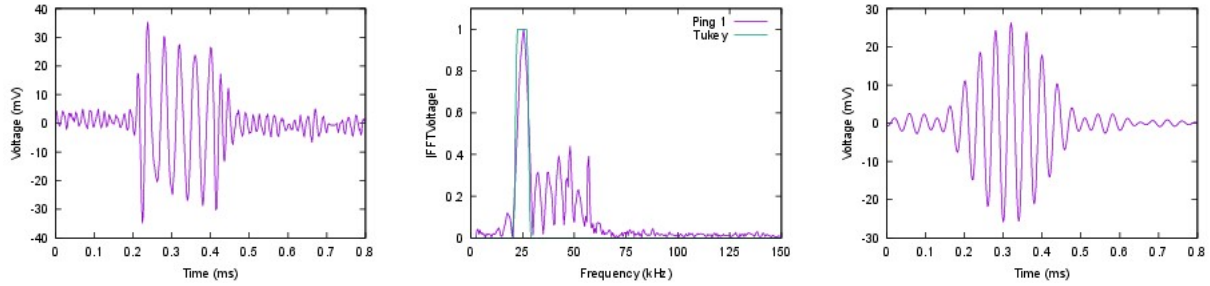

(a) Raw data, 25 kHz (b) |FFT|, 25 kHz (c) Hilbert transform, 25 kHz

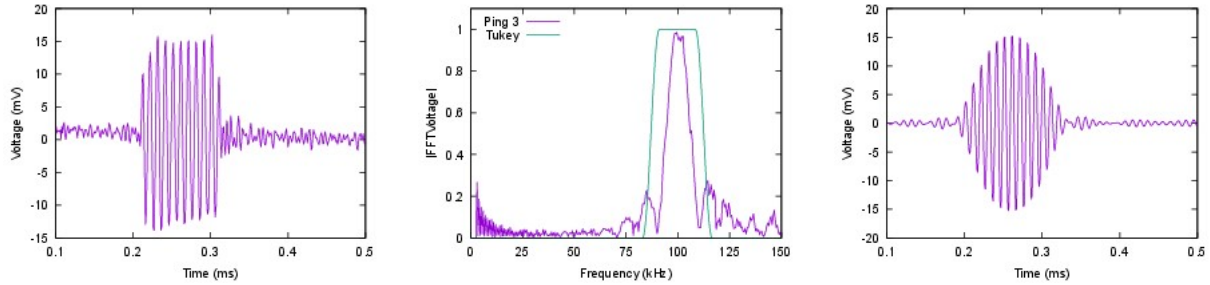

(d) Raw data, 100 kHz (e) |FFT|, 100 kHz (f) Hilbert transform, 100 kHz

Figure 27: Initial steps in the processing chain are shown for LF data scattered from an Amsteel line. The top row is for 25-kHz data, where both sections of the F33 transducer are used. The bottom row is for 100-kHz data with only the inner section active.

Further processing of the data followed one of two paths. First, the data were transformed back to the time domain via a Hilbert transform. Figures 27(c) and 27(f) depict the results of this transformation on the windowed data shown in Figs. 27(b) and 27(e). The first path simply averaged the filtered, but possibly unaligned, pings. The second path would select one of the pings, and compute the cross-correlation for all other pings. This provides an estimate of a lead or lag time for the filtered pings due to possible motion of the ATF. When averaging these pings, each was shifted by its time offset to align all pings. Figures 28(a) and 28(b) contain the results of these processing paths. At 25 kHz, there is little difference between the simple average and the average of the aligned pings. However, the 100-kHz results show a small increase in peak amplitude when the pings are aligned, which suggest the ATF may have been effected by wind.

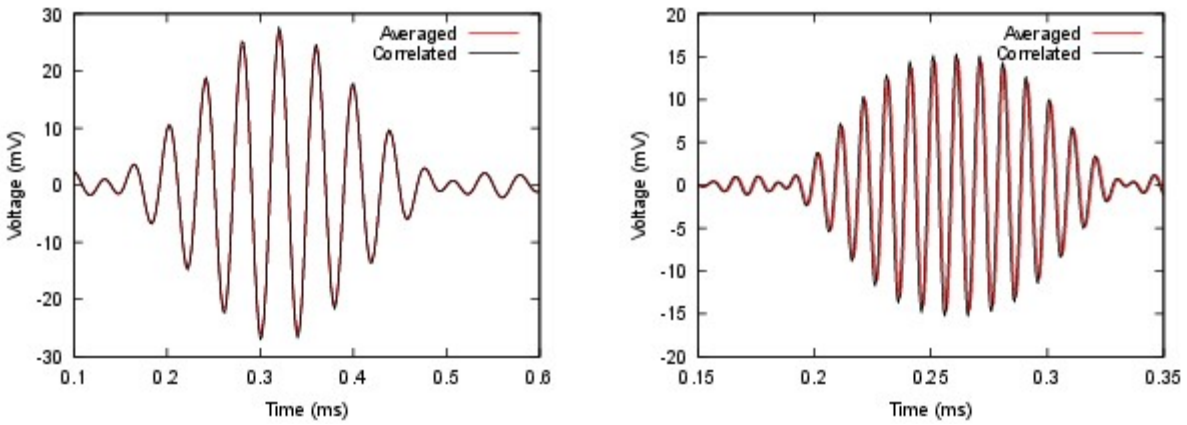

(a) Processed 25 kHz tone burst b) Processed 100 kHz tone burst

Figure 28: The final steps of the processing chain either averaged the unaligned pings (black) or averaged aligned pings after cross-correlation (red).

The processing chain was applied to both the scattered data and the pitch-and-catch data. A relative target strength (TS) was computed from

$$TS = 20\log_{10}\left(\frac{|p_s(f)|}{|p_i(f)|}\right) \tag{33}$$

where $p_s(f)$ is the spectrum of the scattered data and $p_i(f)$ is the spectrum of the pitch-and-catch data. Figure 29 depicts the results from Eq. (33) where the maximum value is retained for each tone burst. It is noted that within the 10–150 kHz range, the time sampling of the data was $\Delta t = 2$ μs, which translates to a Nyquist frequency of 500 kHz. A prime-factor FFT [27, 28] was used in the data processing such that the selected number of time points yields $\Delta f = 0.5$ kHz.

A number of observations are evident from Fig. 29. First, when the lines were placed in the vacuum chamber and degassed, the relative TS is significantly lowered. It is well-known that a gas bubble in water has a fairly large scattering cross-section [29]. In particular, near the resonance frequency of a bubble, the scattering cross-section can be on the order of 3000 times larger than the physical cross-section of the bubble. Without special handling, the lines retain air and it is the presences of this air that causes a strong scattered signal. Second, a discontinuity appears at 50 kHz. This is the upper and lower frequency in the bands transmitted by the F33 when it is configured to use two active sections versus one section, respectively. Sheng and Hay [26] show that one must account for the source's beam pattern when the total length of a long thin wire exceeds the ensonified length. Equation (33) does not currently compensate for a beam pattern, and it is likely that the discontinuity is an artifact from the different aperture sizes. A third observation is that ping alignment through cross-correlation appears to improve the non-degassed case (upper purple and green points). For the degassed data, only the upper frequencies appear to be improved, in particular for Amsteel (see Fig. 29(b)). The degassing of the line causes the amplitude of the scattered signals to approach the noise floor of the experiment in the lower frequencies. Thus, the cross-correlation method may not provide sufficient accuracy in predicting

a lead or lag time. Finally, the legends for Figs. 29(e) and 29(f) were omitted for clarity, but are that same as those in Figs. 29(a) and 29(b).

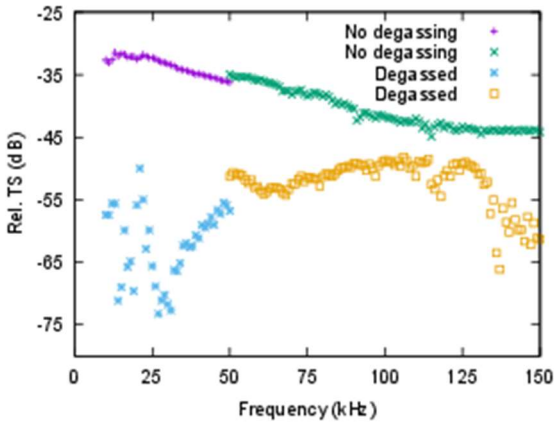

(a) Amsteel (unaligned pings)

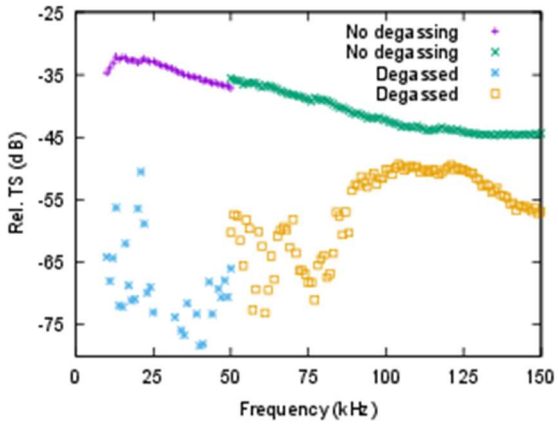

(b) Amsteel (aligned pings)

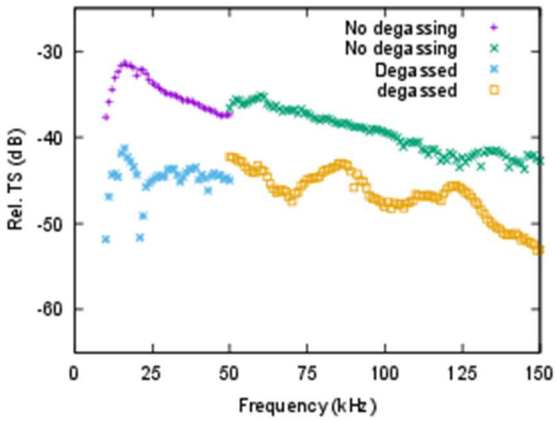

(c) 550 parachute cord (unaligned pings)

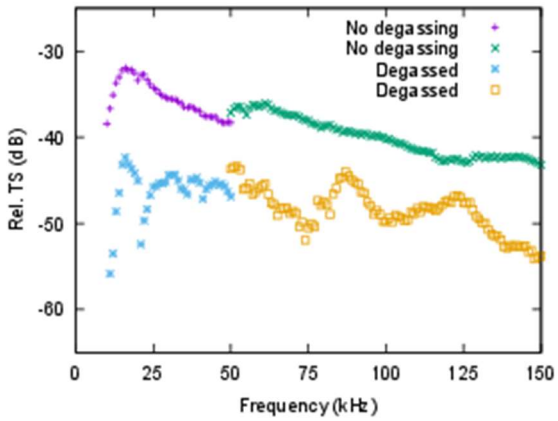

(d) 550 parachute cord (aligned pings)

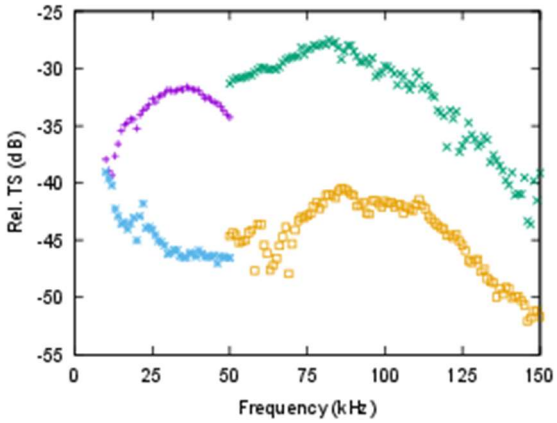

(e) Polypropylene (unaligned pings)

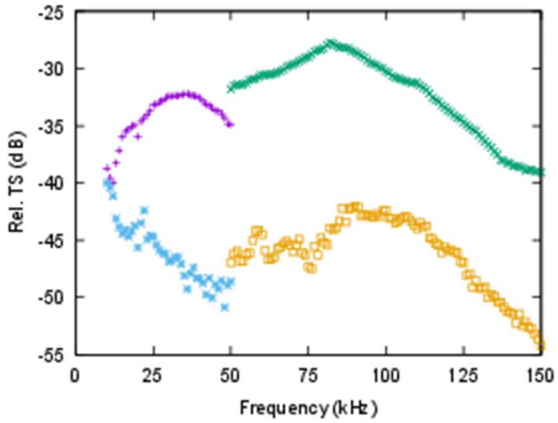

(f) Polypropylene (aligned pings)

Figure 29: Relative TS are shown for lines often used in layout of target fields. The left and right columns are the results when the pings are unaligned and aligned, respectively.

Sine-wave tone burst data were not collected from the fibrous cotton rope under non-degassed conditions. When the rope was placed into the water, a thin veil of bubbles were seen rising up along its exterior. After waiting several minutes, the rope was removed, placed into the vacuum chamber, and later returned to the ATF for data collection under degassed condition. The results for tone burst are not shown here, because of the lack of data for comparison under non-degassed conditions and it is unlikely that this type of line will be used within a target field due to its low visibility and poor contrast with typical sediments.

The magnitude of the spectra for the 10–50 and 50–150 kHz LFM pulses, recorded in a pitch-and-catch configuration, are depicted in Figs. 30(a) and 30(b). For display purposes, these are scaled to have a maximum value of one. The Tukey windows, used in processing the LFM pulse data, are also shown. The width of the window is tailored to reject frequency components outside of the band of interest. These spectra are used in the normalization of the scattered data, and contain both the transmitter voltage response of the F33 transducer and the receiver sensitivity of the H52 hydrophone but do not include beam patterns. Figure 30(c) displays the relative target strength for a background measurement with the 10–50 LFM pulse. For the background measurement, the source and receiver were placed in the scattering geometry described above for the LF range. With no lines in view, pings were recorded of the time window of interest. The purple line in Fig. 30(c) represents the noise floor of the experiment in this frequency range. Figure 30(c) also depicts the relative TS for the fibrous cotton rope and braided fishing line. The green line is for the rope, where it was not placed in the vacuum chamber; rather it was placed into the water and left to naturally de-gas (i.e., no visible bubbles rising along the rope). The gold and blue lines are the relative TS for fishing line and rope after degassing. Clearly, measurements from these lines are close to the noise floor, which makes any attempts to estimate a relative TS difficult.

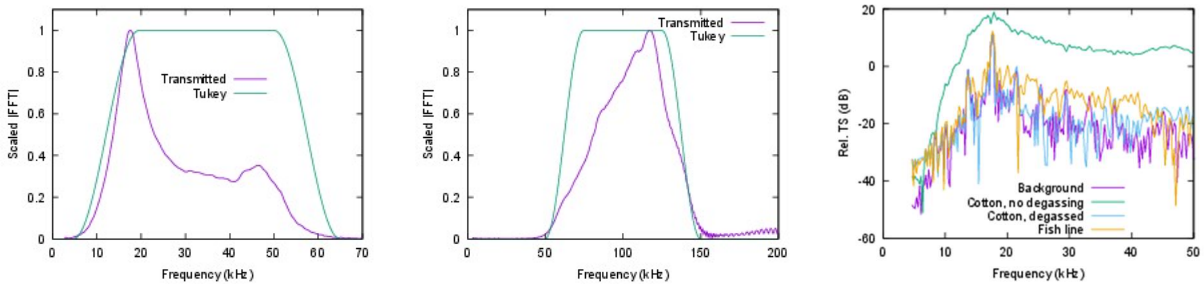

(a) 10–50 kHz LFM pulse (b) 50–150 kHz LFM pulse c) 10–50 kHz noise floor

Figure 30: The spectra for the (a) 10–50 and (b) 50–150 kHz pulses are displayed along with the Tukey window. (c) The noise floor measured over the 10–50 kHz band.

Figure 31 shows the relative TS measured with the two LFM pulses. The general trend found in Fig. 29, where the relative TS was significantly lower for the degassed lines than the non-degassed case, is observed here. Only the TS after aligning the pings for averaging is depicted The unaligned-ping average is similar. The cause of the fine structure, particularly in the 50-150 kHz range, is currently unknown, but is indicative of a weak signal arriving with a time delay within the time window of interest (e.g., a reflection of the scattered signal from the source transducer). A second observable is the drop in levels at the edges of each frequency band. A portion of this drop may be related to the width of the Tukey windows shown in Figs. 30(a) and

30(b). The beamwidth of the source beam pattern may also contribute to the drop. The data processing chain currently does not compensate for beam patterns. Recalling that $p_i(f)$ in Eq. (33) is a spot measurement on the acoustic axis of the source, Eq. (33) would need to include a frequency-dependent beam pattern correction in the denominator. Sheng and Hay [26] denote the correction factor as $\Gamma(r_0)$ with r_0 being the horizontal distance of the source from line. The form of $\Gamma(r_0)$ involves an integral over the ensonified length of line and the source's beam pattern. In addition, estimates for $\Gamma(r_0)$ depend on whether the source transmits a continuous monochromatic signal or a finite duration pulse.

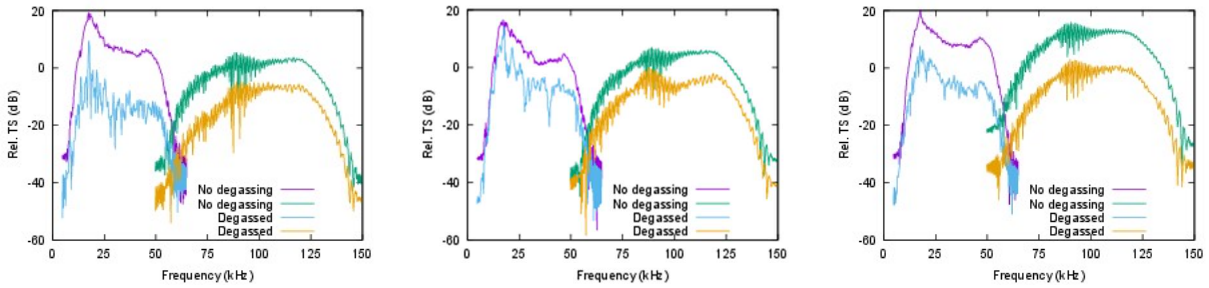

(a) Amsteel (b) 550 parachute cord c) Polypropylene

Figure 31: Relative TS for Amsteel, 550 parachute cord, and polypropylene line are depicted when the transmitted pulse is an LFM pulse. These results are for ping-aligned data.

8 Concluding Remarks

8.1 Bistatic scattering amplitude

One of the primary goals of SERDP MR19-1234 was the development of a simulation capability to simulate the MuST system under development at APL-UW. Due to large spatial separation between the sources and receiving array elements (on the order of 1 m) in comparison to the short stand-off distances to objects (on the order of 5 m), bistatic scattering becomes important. High-speed and high-fidelity models for most objects leverage look-up tables that are indexed by frequency and information related to the scattering geometry. Section 3.1 discusses initial implementation details for look-up tables where the receiver's polar and azimuthal angles were sampled with an uniform increment. To achieve an acceptable level of fidelity, angular increments were often set to $\Delta\theta_r = \Delta\theta_s = 1^\circ$, which led to an oversampling near poles and thus extremely large tables. It was found in Sec. 3.2 that the Fibonacci lattice, also known as the golden spiral, could be utilized to populate a spherical surface with a nearly uniform distribution of receiver locations. The golden spiral led to a significant reduction in table size at the expense of a slightly more complicated indexing scheme. New tables were generated for five objects, and two of these tables were used for the multiple scattering simulations displayed in Fig. 18.

An initial simulation of the MuST system has been performed. During October 2022, the MuST was deployed in Sequim Bay, WA as part of an ESTCP blind test bed. Figure 32 shows the tracks of the two sources from data sequence 63, which was collected on 6 October 2022. These tracks are relative to onboard GPS navigation, and the initial port source location is used as

a fiducial to set an origin for Fig. 32. The entire track represents 3674 source transmissions. The red portion of Fig. 32 represents 301 consecutive pings, and the straight-line distance for the first location to the last is ≈ 10 m. Operationally, the starboard source would transmit and 64 signals were recorded on the individual elements of the receiving array; and then, the port source transmits and 64 new signals are recorded. Thus, the 301 pings correspond to 19264 individually recorded signals. TIER model simulations have been performed for the red portion of Fig. 32.

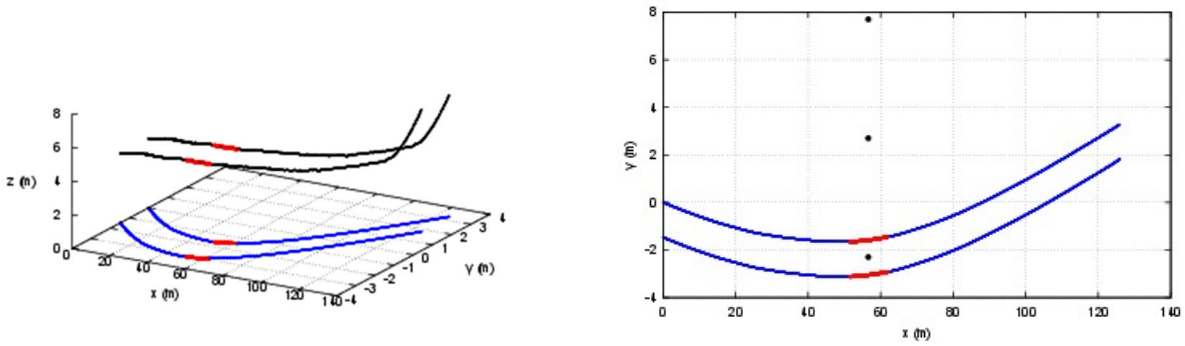

(a) Track of MuST (b) Track restricted to xy-plane

Figure 32: Tracks of sources on MuST are shown for data sequence 63 collected in Sequim Bay. Red portion is used in simulations, and black dots are locations of a 155-mm shell.

Water-filled, 155-mm howitzer shells were placed at $T_0 = (56.6, -2.3, -0.0875)$ m, $T_1 = (56.6, 2.7, -0.0875)$ m, and $T_2 = (56.6, 7.7, -0.0875)$ m. The locations of the shells are the black dots in Fig. 32(b). The average speed of sound in the water along the path of the MuST system was $c_1 = 1489.7$m/s and simulations use $\rho_1 = 1000$ kg/m^3. The sonar has a nominal 5–25 kHz frequency band. To cover this band, a 6-ms duration LFM pulse was created with a 2–26 kHz band. An envelope was applied to the pulse to taper the leading and trailing edges. Received signals were recorded over a 30-ms time window, $t = 0$ ms for each pulse corresponds to the initial time of transmission, and the sample rate was 97.7 kHz. Both free-field and buried environments were simulated. The sea floor of Sequim Bay at the measurement site was identified as sand, but physical properties were unavailable at the time the simulations were performed. Sediment properties from TREX13 were used: $\rho_2 = 1800$ kg/m^3, $c_2 = 1694$ m/s, and $\delta_2 = 0.008$. With $z_t = -0.0875$ m and a shell radius of $a = 0.0775$ m, the buried case represents a shell with 1 cm of sediment above it.

SAS images were constructed with a time-domain beam former at the location of each shell. That is, the plane of an image is parallel to the xy-plane and set to a dep $z_t = -0.0875$ m. Each image covers a 2×2 m^2 area, and the absolute target strength is shown on a 30 dB color scale with red being 42 db. Figures 33(a) and 33(b) are for the free-field and buried environments, respectively. The bottom, middle, and top rows correspond to T_0, T_1, and T_2. Euler angle rotations are listed at the top of each column. A rotation of $\beta = 90^\circ$ places the shell with its symmetry axis parallel to the water-sediment interface. Rotations in α then change the pose angle of the shell with respect to the x-axis of Fig. 32(b). In the $(90^\circ, 90^\circ, 0^\circ)$ orientation, the nose of the shell points away from the path of the MuST. Inspection of Fig. 33 shows a significant reduction in the TS for T_1, and T_2 in the full burial cases. This is due partly to the attenuation within the sediment along

the refracted portion of each path, the values of the relevant transmission coefficients in crossing the water-sediment interface, and the use of c_1 as a reference sound speed during SAS processing (i.e., a defocusing due to phase error). It is noted that MuST passes over the top of T_0 and the free-field and buried simulations do not show too many differences as both are essentially looking down onto the shell where propagation within the sediment is minimal.

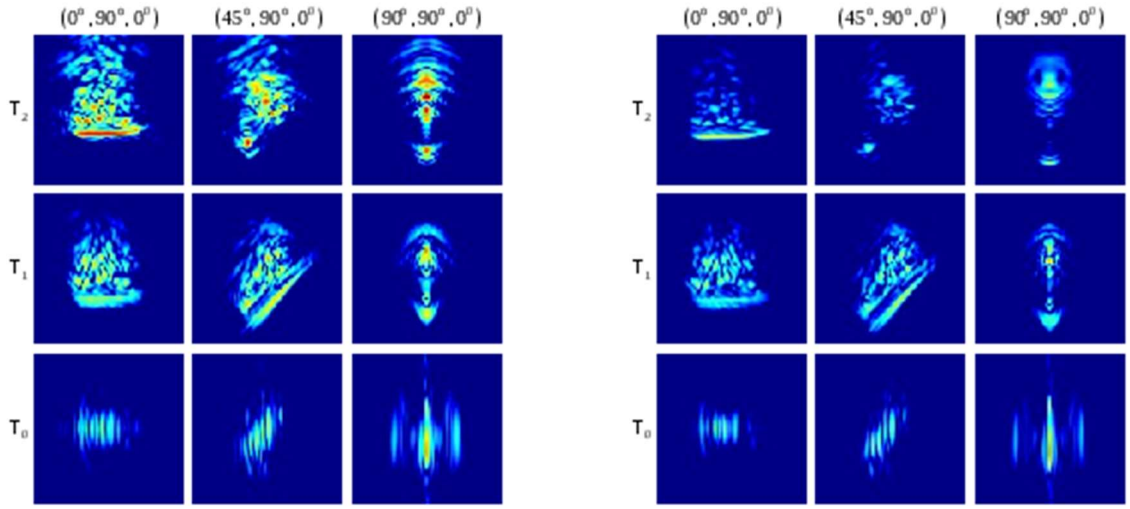

(a) Free field simulation (b) Buried object simulation

Figure 33: The track of the sources on MuST are displayed for the data sequence 63 collected in Sequim Bay on 6 October 2022.

The SAS images in Fig. 33 represent an infinite signal-to-noise ratio (SNR). These types of simulations can provide suitable data to augment the Sequim Bay data for training and classification purposes. Work has been initiates with Williams and Marston under ESTCP MR18-5004 to repackage the TIER model simulations into a format that can be consumed by the MuST processing chain. Note, the SNR of the simulated data can be lowered or "dirtied" by the reverberation model discussed in Sec. 6 or by superposition with measured MuST background data (e.g., a region of MuST data with no known objects).

8.2 Multiple scattering

After completing the work in Sec. 4, a new class of multiple scattering was identified for a pair of in-water objects near the sea floor. The ray diagram for second-order multiple scattering is shown in Eq. (26) of Sec. 4. The new class of ray diagram for second-order is

$$S_i \to T_k \to B \to T_l \to R_j \tag{34}$$

where B represents an interaction with the sea floor. Figure 34(a) depicts the scattering path and Fig. 34(b) shows the corresponding ray diagram. The ray that interacts with the sea floor appears to originate from the location of an image object T_i. This construction is convenient in that the point B on the interface can easily be found, which is needed in the determination of the bistatic scattering angles from T_k to B and the grazing angle of incidence for the reflection coefficient. An

interaction with the sea floor can occur for any pair of objects in the ray diagrams shown in Eqs. (26)–(28) of Sec. 4. Thus, there can be a significant increase in the number of ray paths that contribute to the total pressure.

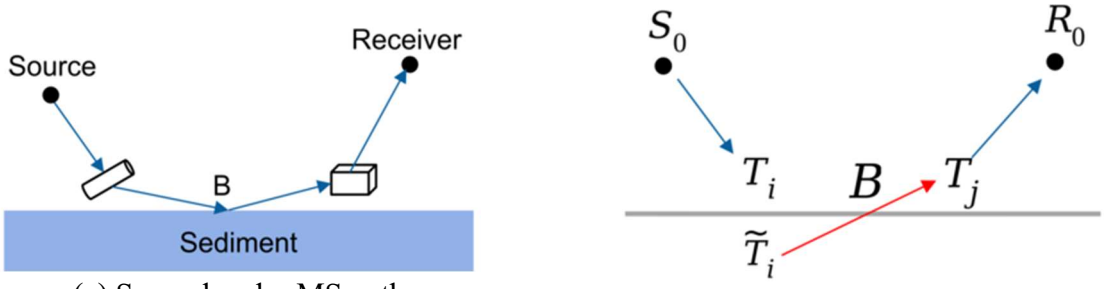

(a) Second-order MS path (b) Ray diagram

Figure 34: (a) A new ray path interacts with the sea floor before it arrives at a second object. (b) The ray path is associated with an image of an object.

In Sec. 2, the TIER model replaces the scattering from an object in a halfspace or waveguide by an equivalent collection of free-field scattering problems. This is accomplished by reflecting image sources and image receivers through the sea floor and, if present, an air-water interface of a waveguide. In the enumeration of this new class of ray paths, it is important to note that a ray path originating from a source never interacts with an image object. Likewise, a ray path from an image object never reaches a receiver. That is, the sea floor interaction occurs for a ray path connecting two objects. While the approach to include this new class of ray diagrams into the TIER model has been established. Implementation had been delayed until bistatic scattering amplitudes, based on a golden-spiral distribution, were available.

8.3 Ray model in inhomogeneous medium

When the water column no longer has a constant sound speed, an acoustic ray path will deviate from a straight line. In Sec. 5, the integration of the TIER model with BELLHOP to remove the straight line assumption was discussed. An important feature of BELLHOP is its ability to efficiently isolate an eigenray, which connects point A to point B within the water column. Mathematically, this involves a numerical integration of a coupled set of differential equations (i.e., the eigenray equations) in a generalized coordinate system such that an eigenray from A is constrained to pass through B [24]. Closer inspection of the BELLHOP source code found that it does not solve the eigenray equations. Rather, it propagates several rays from A and searches for pairs that pass closest and brackets point B. Two advantages of this approach are interactions with boundaries and possible phase shifts from a ray passing through caustics are automatically tracked. A pair of rays bounds the actual eigenray, and by broadcasting a dense set of rays, the pair approaches the eigenray. Figure 20 shows the eigenray paths with at-most one boundary interaction.

As discussed in Sec. 5, BELLHOP was modified to output the eigenray parameters needed for Eq. (29). These include a complex amplitude, propagation phase and time delay, and an angle of impact at B. The TIER model was modified to directly execute BELLHOP for a ray path from a

source to the object, $S \rightarrow T$, and for the scattered ray from the object to the receiver $T \rightarrow R$. The eigenray parameters are stored in external files and the TIER model consumes these to evaluate Eq. (29). Figures 21 and 22 show a comparison of the original waveguide environment of Sec. 2.3 and the newly integrated BELLHOP model for a nearly isotropic water column.

8.4 Scattering from test bed lines

Measurement of acoustic scattering from lines was a task added to SERDP MR19-1234. The target strength of 5 line types were measured to address the influence of a line might have on sonar detection. Five line types are investigated in Sec. 7. Amsteel and 550 parachute cord are often chosen because of their light weight, high visibility, and strength. LF and HF frequency bands of 10–150 kHz and 100–2000 kHz band were considered. Measurements overlapped at 100 kHz to allow direct comparison of the two bands. At the time of data collection, equipment issues appear to cause a nonlinear contamination of the HF data. Additional, HF data were collected and analyzed by Lim under SERDP MR21-7211.

In Sec. 7, the processing chain was described. Figures 29 and 30 reveal that the relative target strength for a line deployed without special handling is significantly higher than for a line placed under a vacuum for a short time. Trapped air in the lines has been identified as the cause of this higher TS. The availability of the ATF for the TS measurements was too short to allow us to determine if long-term deployment of lines at depth would naturally degas [30]. However, during the October 2021 Sequim test bed measurement, the Amsteel, 550 parachute cord, and polypropylene lines were deployed along the calibration line of the test bed. It has been reported that SAS images showed one or more of the lines (K. Williams and T. Marston, private communications). Finally, Figs. 29 and 30 display only a relative target strength, because compensation for beam-pattern effects has not been included.

A choice of line type must be made to aid in the deployment and recovery of objects placed in an at-sea test bed. Although line strength, durability, and diver visibility are important characteristics, Fig. 29 suggests that test bed practitioners should take some action to mitigate the presence of trapped air within a line. As discussed in Sec. 7, placement of a line under a vacuum led to a reduction in target strength across the entire LF band. An alternate approach, not investigated here, might be the application of an environmentally friendly surfactant to a line. A reduction in surface tension should aid in the evacuation of trapped air.

Finally, the original intent with adding this task to SERDP MR19-1234 was to expand the TIER model's capability to model the scattering from lines. As noted in Sec. 2.1, a fundamental assumption within the TIER model is that an object is uniformly illuminated across its cross-sectional area during a given scattering configuration. For the lines used in CLUTTEREX17 and observed in Fig. 25(a), this condition is not met. However, the TIER model can simulation the scattering from a finite cylinder via the models of Stanton [11,12] and Ye [10]. The long lines in a test bed can be partitioned into a sequence of line segments. The acoustic scattering from each segment can be superposed to simulated the scattering form the total line.

References

[1] K. L. Williams, S. G. Kargl, E. I. Thorsos, D. S. Burnett, J. L. Lopes, M. Zampolli, and P. L. Marston, "Acoustic scattering from a solid aluminum cylinder in contact with a sand sediment: Measurements, modeling, and interpretation," *J. Acoust. Soc. Am*., vol. 127, pp. 3356–3371, 2010.

[2] M. B. Porter, "BELLHOP," Heat, Light, and Sound Research, Inc., Tech. Rep., 2018, http://oalib.hlsresearch.com/Rays/.

[3] L. M. Brekhovskikh and Y. P. Lysanov, Fundamentals of Ocean Acoustics, 2nd ed. New York, NY: Springer-Verlag, 1991.

[4] S. G. Kargl, K. L. Williams, and E. I. Thorsos, "Synthetic aperture sonar imaging of simple finite targets," *IEEE J. Ocean. Eng*., vol. 37, pp. 516–532, 2012.

[5] K. L. Williams, "An effective density fluid model for acoustic propagation in sediments derived from biot theory," *J. Acoust. Soc. Am*., vol. 110, no. 5, pp. 2276–2281, 2001.

[6] S. G. Kargl, A. L. España, K. L. W. J. L. Kennedy, and J. L. Lopes, "Scattering from objects at a water-sediment interface: experiment, high-speed and high-fidelity models, and physical insight," *IEEE J. Ocean. Eng*., vol. 40, pp. 632–642, 2015.

[7] G. C. Gaunaurd and H. ¨Uberall, "Rst analysis of monostatic and bistatic acoustic echoes from an elastic sphere," *J. Acoust. Soc. Am*., vol. 73, pp. 1–12, 1983.

[8] S. G. Kargl and P. L. Marston, "Observations and modeling of the backscattering of short tone bursts from a spherical shell: Lamb wave echoes, glory, and axial reverberations," *J. Acoust. Soc. Am*., vol. 85, pp. 1014–1028, 1989.

[9] S. G. Kargl and P. L. Marston, "Ray synthesis of the form function for backscattering from an elastic spherical shell: leaky lamb waves and longitudinal resonances," *J. Acoust. Soc. Am*., vol. 89, pp. 2545–2558, 1991.

[10] Z. Ye, "A novel approach to sound scattering by cylinders of finite length," *J. Acoust. Soc. Am*., vol. 102, pp. 877–884, 1997.

[11] T. K. Stanton, "Sound scattering by cylinders of finite length. I. Fluid cylinders," *J. Acoust. Soc. Am*., vol. 83, pp. 55–63, 1988.

[12] T. K. Stanton, "Sound scattering by cylinders of finite length. II. Elastic cylinders," *J. Acoust. Soc. Am*., vol. 83, pp. 64–67, 1988.

[13] M. Zampolli, A. Tesei, G. Canepa, and O. A. Godin, "Computing the far field scattered or radiated by objects inside layered fluid media using approximate green's functions," *J. Acoust. Soc*. Am., vol. 123, pp. 4051–4058, 2008.

[14] M. Zampolli, A. L. E. na, K. L. Williams, S. G. Kargl, J. L. Lopes, J. L. Kennedy, and P. L. Marston, "Low- to mid-frequency scattering from elastic objects on a sand sea floor:

simulation of frequency and aspect dependent structural echoes," *J. Comp. Acoust*., vol. 20, p. 1240007 (14 pp.), 2012, dOI: 10.1142/S0218396X12400073.

[15] E. B. Saff and A. B. J. Kuijlaars, "Distributing many points on a sphere," *The Mathematical Intelligencer*, vol. 19, pp. 5–11, 1997, DOI: 10.1007/BF03024331.

[16] B. Keinert, M. Innmann, M. S¨anger, and M. Stamminger, "Spherical fibonacci mapping," *ACM Trans. Graph*., vol. 34, p. 7 pages, 2015, DOI: 10.1145/2816795.2818131.

[17] M. Roberts, "How to evenly distribute points on a sphere more effectively than the canonical fibonacci lattice," 2020, http://extremelearning.com.au/.

[18] P. C.Waterman, "Matrix theory of elastic wave scattering," *J. Acoust. Soc. Am*., vol. 60, pp. 567–580, 1976.

[19] A. Boström, "Scattering of stationary acoustic waves by an elastic obstacle immersed in a fluid," *J. Acoust. Soc. Am*., vol. 67, pp. 390–398, 1980.

[20] A. Boström, "Scattering by a smooth elastic obstacle," *J. Acoust. Soc. Am*., vol. 67, pp. 1904–1913, 1980.

[21] S. G. Kargl and R. Lim, "A transition-matrix formulation of the scattering in homogeneous, saturated, porous media," *J. Acoust. Soc. Am.,* vol. 94, pp. 1527–1550, 1993.

[22] T. M. Marston, P. L. Marston, and K. L. Williams, "Scattering resonances, filtering with reversible sas processing, and applications of quantitative ray theory," in *Proc. 2010 Oceans MTS/IEEE* Seattle, 2010, p. 9pp, DOI: 10.1109/OCEANS.2010.5664606.

[23] D. J. Zartman, D. S. Plotnick, T. M. Marston, and P. L. Marston, "Quasi-holographic processing as an alternative to synthetic aperture sonar imaging," in *Proc. Meet Acoust. Soc. Am*., 2013, p. 5pp, DOI: 10.1121/1.4800881.

[24] F. B. Jensen, W. A. Kuperman, M. B. Porter, and H. Schmidt, Computational Ocean Acoustics. New York, NY: Springer, 2011.

[25] R. Lim, "Scattering strength of target lines used to facilitate relocation and recovery," SERDP MR21-7211, 2021, https://serdp-estcp.org/projects/details/75f295f6-31b0-4b0e-943d-6c39c8ea544b.

[26] J. Sheng and A. E. Hay, "Spherical wave backscatter from straight cylinders: Thin-wire standard targets," *J. Acoust. Soc. Am*., vol. 94, pp. 2756–2765, 1993.

[27] C. Temperton, "Self-sorting in-place fast fourier transforms," *SIAM J. Sci. Stat. Comp*.,vol. 12, pp. 808–823, 1991.

[28] C. Temperton, "A generalized prime factor fft algorithm for any $n = 2^p3^q5^r$," *SIAM J. Sci. Stat. Comp.*, vol. 13, pp. 676–686, 1992.

[29] S. G. Kargl, "Effective medium approach to linear acoustics in bubbly liquids," *J. Acoust. Soc. Am*., vol. 111, pp. 168–173, 2002.

[30] A. A. Atchley and A. Prosperetti, “The crevice model of bubble necleation,” *J. Acoust. Soc. Am*., vol. 86, pp. 1065–1084, 1989.

[31] R. R. Goodman and R. Stern, “Reflection and transmission of sound by elastic spherical shells,” *J. Acoust. Soc. Am*., vol. 34, pp. 338–344, 1962.

[32] “Bessel Functions: Spherical Bessel Functions - Explicit Formulas,” in NIST Digital Library of Mathematical Functions. NIST, 2010-2023, https://dlmf.nist.gov/10.49.

[33] R. J. Urick, Principles of Underwater Sound. New York: McGraw-Hill, 1975.

[34] S. Kargl and P. L. Marston, “Ray synthesis of lamb wave contributions to the total scattering cross section for an elastic spherical shell,” *J. Acoust. Soc. Am*., vol. 88, pp. 1103–1113, 1990.

[35] L. E. Kinsler, A. R. Frey, A. B. Coppens, and J. V. Sanders, Fundamentals of Acoustics, 3rd ed. New York: Wiley, 1982.

A On the far-field approximation

In many sonar applications, an object-of-interest is typically at a large distance from a source and receiver. This then allows sonar practitioners to simplify mathematical models for the scattered pressure. Appendix A investigates what "large distance" means in the context of a canonical object.

The scattering of a harmonic plane wave from a rigid sphere has a long history, and more importantly an exact solution [31]. For a source with a finite aperture, this implies that the source and sphere are sufficiently separated to ensure uniform ensonification across the object. Furthermore, it is assumed the sphere is sufficiently removed from any boundary such that the fluid can be viewed as infinite in extent. Consider a rigid sphere of radius a placed in an inviscid, homogeneous fluid with sound speed c. The origin of the scattering geometry is centered in the sphere. For completeness, the plane wave propagates in the $+z$ direction and has the form $p_i(z) = p_0 \exp(ikz - i\omega t)$; and henceforth, the time dependence will be suppressed. Here, p_0 is a constant amplitude. The frequency, angular frequency, and wavenumber within the fluid are f, $\omega = 2\pi f$, and $k = \omega/c$ = ω/c. The scattered pressure at an observation point r has the following exact mathematical representation

$$p_e(r) = p_0 \sum_{n=0}^{\infty} i^n (2n+1) \frac{j_n'(ka)}{h_n'(ka)} h_n(kr) P_n(\cos\theta) \tag{A1}$$

The nth-order spherical Bessel function, spherical Hankel function of the first kind, and Legendre polynomial are j_n, h_n, and P_n, respectively. A prime denotes differentiation with respect to the argument of the function and $i = \sqrt{-1}$.

The far-field approximation considers the asymptotic behavior of $h_n(kr)$, which has an explicit representation [32, 10.49.6]. After a minor re-arrangement of 10.49.6, one has

$$h_n(kr) = i^{-n} \frac{exp(ikr)}{ikr} \sum_{m=0}^{n} b_m(n) \frac{i^m}{(kr)^m} \tag{A2}$$

$$b_0(n) = 1 \tag{A3}$$

$$b_{m+1}(n) = \frac{(n+m+1)(n-m)}{2(m+1)} b_m(n), \quad 0 \le m \le n-1. \tag{A4}$$

In the limit $kr \gg 1$, the far-field assumption retains only the leading term,

$$h_n(kr) \to i^{-n} \frac{exp(ikr)}{ikr} \tag{A5}$$

where the first neglected term is of order $(kr)^{-2}$. If Eq. (A5) is inserted into Eq. (A1), the resulting expression can be arranged to give

$$p_f(r) \approx p_0 \frac{a}{2} \left[\frac{2}{ika} \sum_{n=0}^{\infty} (2n+1) \frac{j_n'(ka)}{h_n'(ka)} P_n(\cos\theta) \right] \frac{\exp(ikr)}{r} = p_0 \frac{a}{2} F(\theta) \frac{\exp(ikr)}{r} \tag{A1}$$

The notation p_f is used in Eq. (A6) to distinguish it from p_e of Eq. (A1). The dimensionless factor within the square bracket is often referred to as the form function, $F(\theta)$. In the context of the TIER model, the bistatic scattering amplitude is then $S(\theta) = a\,F(\theta)/2$, which due to symmetry depends only the polar angle of the observation point as well as the ensonifying frequency. Note, for $ka \rightarrow \infty$, one has $F(\theta) \rightarrow 1$, and the target strength reduces to $TS = 20\log_{10}(a/2)$ where the geometric spreading $1/r$ is removed and a is referenced to 1 m. The expression for TS agrees with Urick [33].

The infinite summations of Eqs. (A1) and (A6) need to be truncated after each has converged. In previous work, Kargl and Marston [34] established that truncation for $F(\theta)$ can occur at $n_{max} = 3 + \lfloor ka + 4\sqrt[3]{ka} \rfloor$ where $\lfloor \cdots \rfloor$ retains only the integer part. In addition to p_e and p_f, a look-up table was constructed for a bistatic scattering amplitude from $p_e(r)$ such that

$$p_t(r) = S_{ij}\frac{\exp(\imath kr)}{r} \tag{A7}$$

$$S_{ij} = r_0 p_e(r_0, i\Delta f, j\Delta\theta)exp(-\imath kr_0) \tag{A8}$$

with $r_0 = 10$ m, $\Delta f = 100$ Hz, and $\Delta\theta = 1^\circ$. This look-up table permits one to gain confidence in the construction and use of tables for the bistatic scattering amplitudes described in Sec. 3 for UXO and other scientific objects. For a set of parameters (r, f, θ), an estimate of the pressure can be obtained from Eq. (A7) by applying bilinear interpolation techniques to S_{ij}.

Figure A1 displays comparisons of p_e (black), p_f (red), and p_t (blue) for various ranges in the backscattered direction (i.e., $\theta = 180^\circ$). In these computations, the radius of the rigid sphere is a = 0.1 m and the sound speed in the fluid is c = 1500 m/s. Clearly, Fig. A1(a) shows a visible differences between p_e and p_f and between p_e and p_t; while at larger distances p_f and p_t converge to p_e. In APL-UW's TREX13, BAYEX14, and CLUTTEREX17 experiments, the sonar platform operated in the 1–30 kHz range with a minimum distance of closest approach of the sonar to a target of ≈ 5 m. Error estimates for p_f and p_t are depicted in Fig. A2. First, we observe that even at a fairly close range of r = 1 m, the error is typically less than 9%. Figure A2(a) shows the error falls to less than 2% for p_f, and more importantly p_t provides a better estimate for p_e (i.e., < 1%) than p_f. Recalling the table was generated with $r_0 = 10$ m, the error depicted in Fig. A2(b) for p_t is expected; while p_f still has errors approaching 1%. At longer ranges from the sphere, Fig. A2(c)–A2(f) show that p_f is approaching p_e while the error in p_t is consistently less than 1%. The cause for the error in p_t is due to phase information in p_e retained in S_{ij} from the inversion with Eq. (A8) at $r_0 = 10$ m. Finally, construction of a table with $r_0 = 30$ m yields a p_t that is a better estimate of p_e than p_f at 20, 30, and 40 m ranges.

The scattered pressured is a function of the polar angular associated with the observation point. Forward and backward scattering occur at $\theta = 0^\circ$ and 180° respectively. Figures A3 and A4 show the angular dependence in the scattered pressure for $f = 5$ and 25 kHz. These figures show both p_f and p_t converge to the exact pressure p_e for a sufficiently large r. Even at a modestly small value of r = 5 m [green line in Fig. A4(d) and Fig. A4(f)] p_f and p_t capture the scattering lobes in p_e at 40 m.

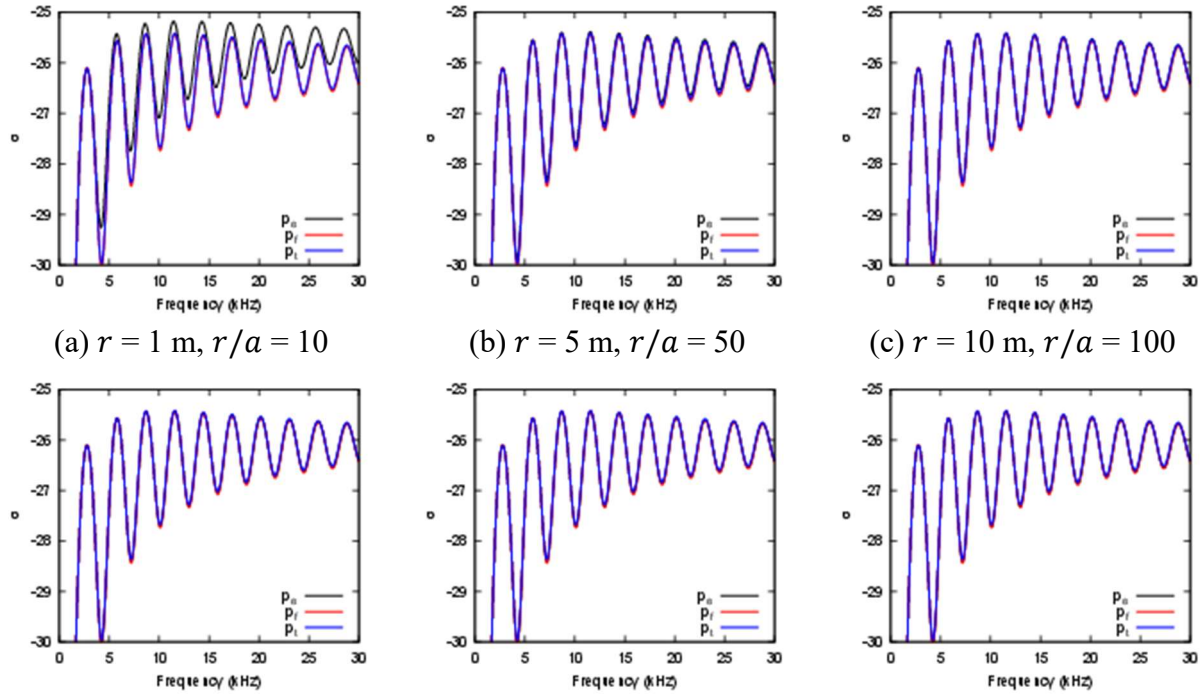

(a) r = 1 m, r/a = 10 (b) r = 5 m, r/a = 50 (c) r = 10 m, r/a = 100

(d) r = 20 m, r/a = 200 (e) r = 30 m, r/a = 300 (f) r = 40 m, r/a = 400

Figure A1: Backscattered target strengths are depicted for a 0.1 m rigid sphere. The r/a ratios for (b)–(f) are those realized in APL-UW experiments.

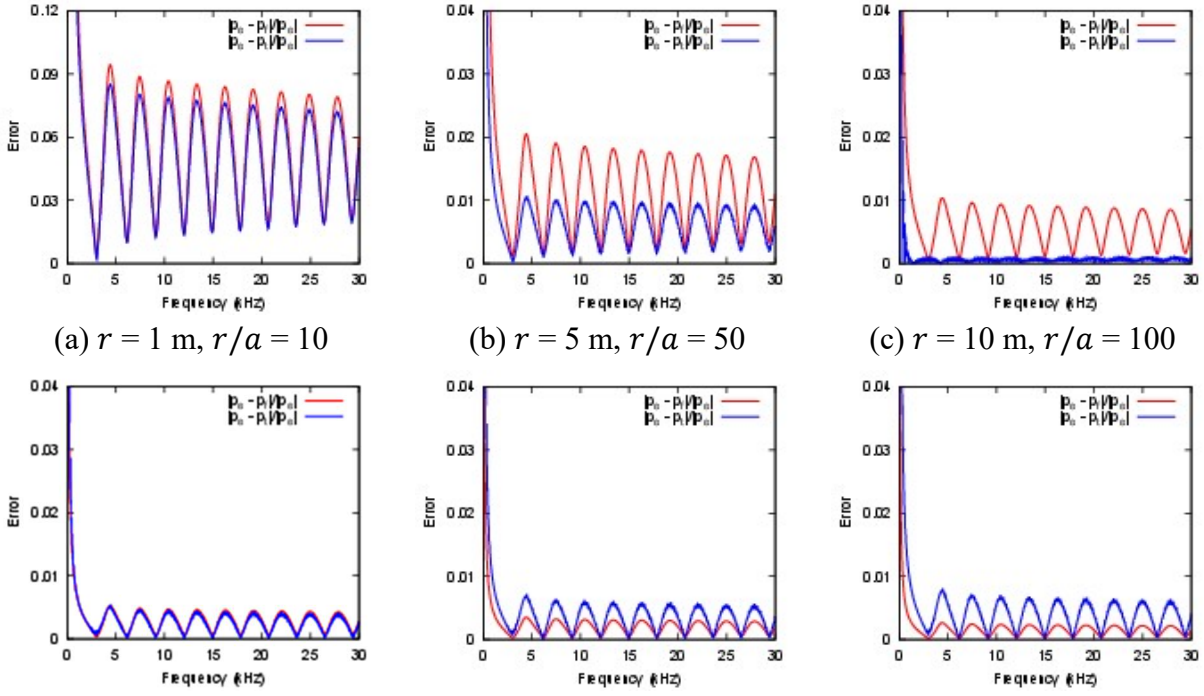

(a) r = 1 m, r/a = 10 (b) r = 5 m, r/a = 50 (c) r = 10 m, r/a = 100

(d) r = 20 m, r/a = 200 (e) r = 30 m, r/a = 300 (f) r = 40 m, r/a = 400

Figure A2: Error estimates in the comparison of Eq. (A1) to either Eq. (A6) or Eq. (A7) are displayed.

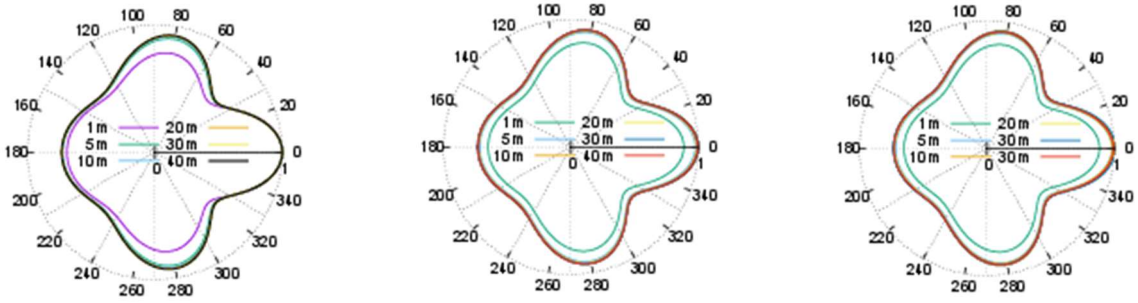

(a) Exact pressure (b) Far-field approximation (c) Interpolated pressure

Figure A3: Magnitude of the scattered pressure from a rigid sphere at 5 kHz is displayed.

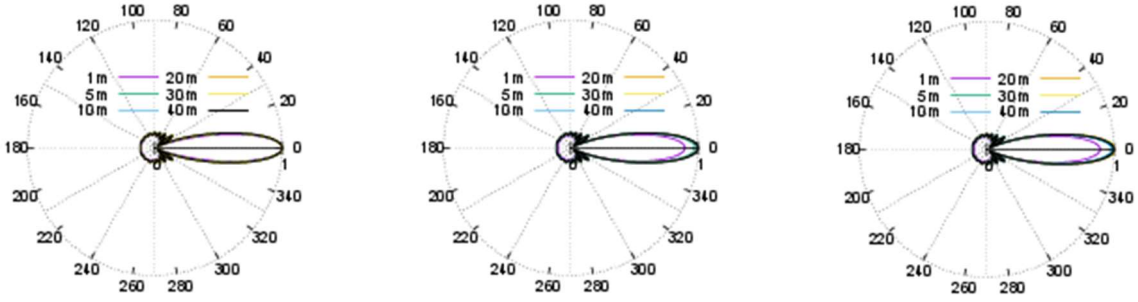

(a) Exact pressure (b) Far-field approximation (c) Interpolated pressure

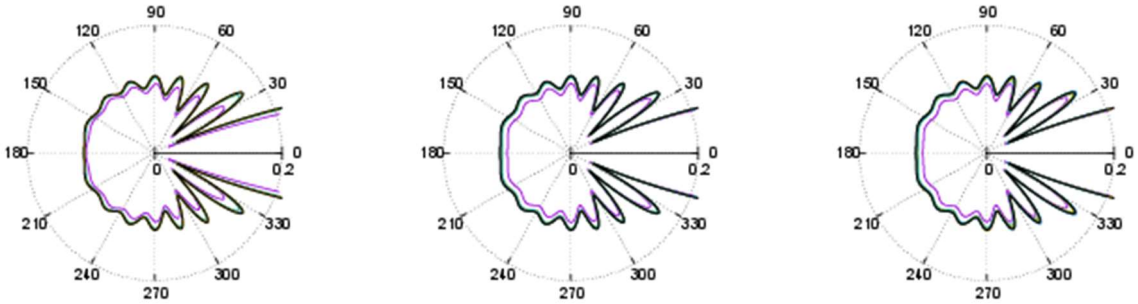

(d) close-up of above (e) close-up of above (f) close-up of above

Figure A4: Magnitude of the scattered pressure from rigid sphere at 25 kHz is displayed. The black lines in (c)–(f) is p_e at $r = 40$ m.

B Fibonacci lattice

A nearly uniform distribution of n points on a spherical surface relies on a method known as a Fibonacci lattice [15,16]. The formulation used in the TIER model is derived from [17], where the canonical Fibonacci lattice for n points in the unit square is defined by

$$(x_i, y_i) = \left(\frac{i+\varepsilon}{n-1+2\varepsilon}, \left\lfloor\frac{i}{\varphi}\right\rfloor\right), \qquad 0 \le i < n \tag{B1}$$

with $\varepsilon = 1/2$, $\varphi = \left(1+\sqrt{5}\right)/2 \approx 1.61803\cdots$, and here $\lfloor\cdots\rfloor$ means only the fractional part is retained. The golden ratio is φ and ε allows one to maximize the minimum separation distance between nearest neighbors. Figure B1(a) shows the distribution for n = 300; while the top row in Table B1 shows the minimum and maximum nearest neighbor distances, average distance, and standard deviation (denoted by d_{min}, d_{max}, $\bar{d}$, and σ, respectively).

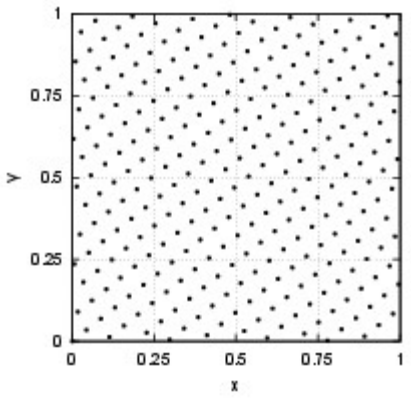

(a) 300 points in unit square

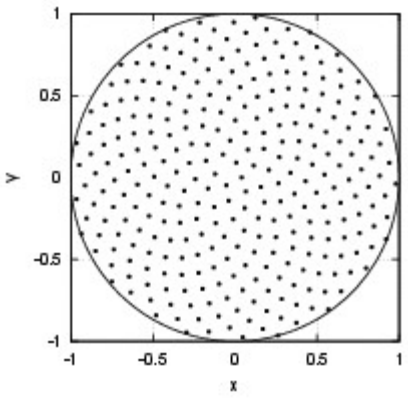

(b) Polar transformation of 300 points

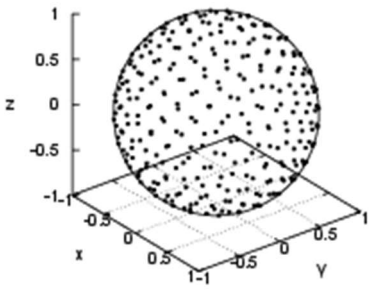

(c) 300 points distributed on sphere

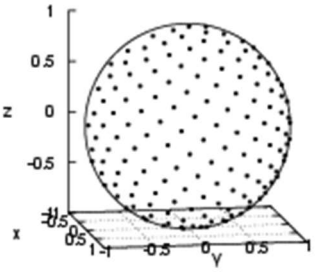

(d) Same as (c) except points with $x < 0$ removed

Figure B1: Nearly uniform distributions of points from Eqs. (B1)–(B3) are depicted for (a) unit square, (b) unit-radius circle, and (c,d) unit-radius sphere.

	ε	d_{min}	d_{max}	$\bar{\bar{d}}$	σ
Eq. (B1)	0.5	0.05535	0.05536	0.05535	0.00000
Eq. (B2)	0.5	0.08926	0.10002	0.09731	0.00112
Eq. (B3)	0.5	0.17849	0.19987	0.19408	0.00261
Eq. (B3)	0.36	0.17829	0.20002	0.19413	0.00273

Table B1: With n = 300, the minimum and maximum nearest neighbor distances were determined along with the average distance and its standard deviation.

The Fibonacci lattice of n points from Eq. (B1) can be transformed into a set of points that are confined to a unit-radius circle. The transformation into polar coordinates is

$$(x_i, y_i) \rightarrow (r_i, \phi_i) = \left(\sqrt{x_i}, 2\pi y_i\right)$$
$$\bar{x}_i = r_i \cos\phi_i, \quad \bar{y}_i = r_i \sin\phi_i \tag{B2}$$

where r_i and ϕ_i are the radial and polar coordinates. Figure B1(b) shows $(\bar{x}_i, \bar{y}_i)$ for a distribution with n = 300 within the unit-radius circle. Visually, one's eye is drawn to subsets of points, which appear to reside on arms that spiral outwards from the center of the circle; and hence, golden spiral is an alternative name for the method. The second row in Table B1 contains d_{min}, d_{max}, $\bar{d}$, and σ for the depicted distribution.

$$(x_i, y_i) \rightarrow (\theta_i, \phi_i) = (\cos^{-1}(1 - 2x_i), 2\pi y_i)$$
$$\bar{x}_i = \sin\theta_i \cos\phi_i, \quad \bar{y}_i = \sin\theta_i \sin\phi_i, \quad \bar{z}_i = \cos\theta_i \tag{B3}$$

where θ_i and ϕ_i are the spherical polar and azimuthal angular coordinates. Figure B1(c) shows the points $(\bar{x}_i, \bar{y}_i, \bar{z}_i)$ on the spherical surface. To aid in the visualization of the golden spiral, points with $\bar{\bar{x}}_i < 0$ have been removed in Fig. B1(d). The last two rows in Table B1 are for ε = 0.5 and 0.36. The former allows for a consistent comparison between the unit square, circle, and sphere; while, the latter is a value recommended in [17] to slightly bias the distribution towards the north and south poles. Given the elongated natural of UXO, this bias may be beneficial in the angular sampling of bistatic scattering amplitude tables used by the TIER model.

C Frequency-dependent Beam Pattern

The original formulation of the TIER model was developed to gain physical insight into data collected during several field measurements performed by APL-UW under ONR and SERDP funded projects. These field measurements included PONDEX10, TREX13, BAYEX14, and CLUTTEREX17, where a sonar platform was scanned along a fixed, straight rail to collect SAS data. The deployed source was an array with effectively four elements. These elements were driven by the linear-frequency-modulated (LFM) signals depicted in Fig. C1(a). The superposition of the transmitted signals achieves a nearly uniform horizontal beam pattern over the entire 1–30 kHz frequency band of the source (see Fig. C1(b)). The intended beam pattern was that of a rectangular source with a 20-cm horizontal width operated at 15-kHz (i.e., the carrier frequency of the LFM signal), which is the green curve in Fig. C1(c). The magenta and cyan curves in Fig. C1(c) are the beam patterns for a 20-cm rectangular source driven at 3 and 30 kHz.

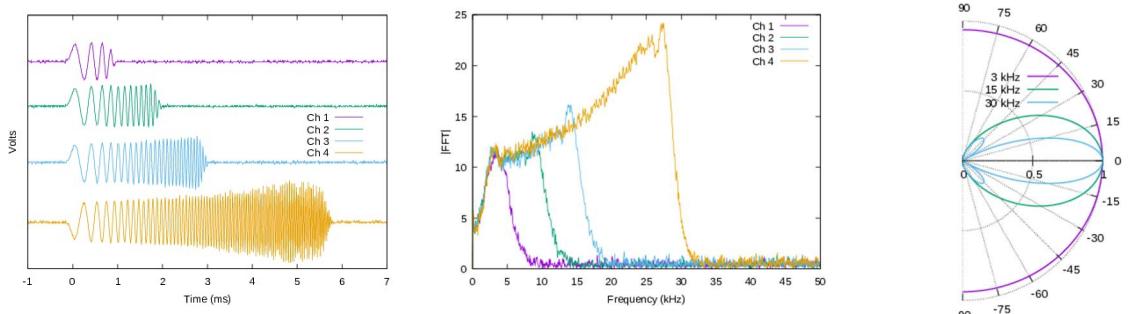

(a) Time signatures (b) Spectra of signals c) Beam patterns

Figure C1: (a) LFM signals applied to elements of the source array used in APL-UW experiments. (b) Fourier transforms of signals in (a). (c) Beam patterns for a 20-cm rectangular aperture.

The TIER model supports a number of beam patterns for a source or receiver within the models defined in Sec. 2. These include beam patterns for rectangular, circular, and omni-directional apertures as well as the capability to use a tabulated beam pattern from measurement. The beam patterns for rectangular and circular apertures have the general forms [35]:

$$B_{rect}(\omega) = \frac{\sin(kl_h \sin\theta_h)}{kl_h \sin\theta_h} \frac{\sin(kl_v \sin\theta_v)}{kl_v \sin\theta_v}, \tag{C1}$$

$$B_{circ}(\omega) = 2\frac{J_1(ka \sin\theta_c)}{ka \sin\theta_c}, \tag{C2}$$

respectively. Horizontal and vertical dimensions of a rectangular aperture are L_h and L_v where Eq. (C1) uses $l_h = L_h/2$ and $l_v = L_v/2$. The radius of a circular aperture is a. The wavenumber is $k = \omega/c_1$. With a Cartesian coordinate system centered in the aperture and the acoustic axis aligned with the $\hat{x}$ axis, the angles are found from $\sin^2\theta_h = y^2/(x^2+y^2)$, $\sin^2\theta_v = z^2/(x^2+z^2)$, and $\sin^2\theta_c = 1 - x^2/(x^2+y^2+z^2)$. For the TIER model simulations, an

aperture's Cartesian coordinate system is translated into a target-centered coordinate system, and an Euler-angle rotation is applied to give a properly oriented aperture.

Figure C2 depicts the magnitude of a 6-ms duration LFM pulse where a number of beam patterns are applied in a pitch and catch configuration. The source is fixed and centered on the left axis of each panel at 0°. A receiver is scanned along a path that is parallel to the left axis. In the sub-captions of Fig. C2, the abbreviations 'src', 'rcv', 'rect', 'circ' and 'omni', are used for 'source', 'receiver', 'rectangular', 'circular', and 'omni-directional', respectively. The separation distance of closest approach between the source and receiver is 10 meters and geometric spread is ignored. Figure C2(a)–(c) assumed a constant wavenumber at the carrier frequency, and Figs. C2(d)–(f) simply allows k to vary over the bandwidth of the LFM pulse. Comparison of the beam patterns in Fig. C1(c) with Figs. C2(d)–(f) can also elucidate the observed shape. It is clear from Fig. C2 that if apodization of an aperture in not applied to a physical source (and/or receiver), then the broad-band response affects the detected scattered pressure from a target.

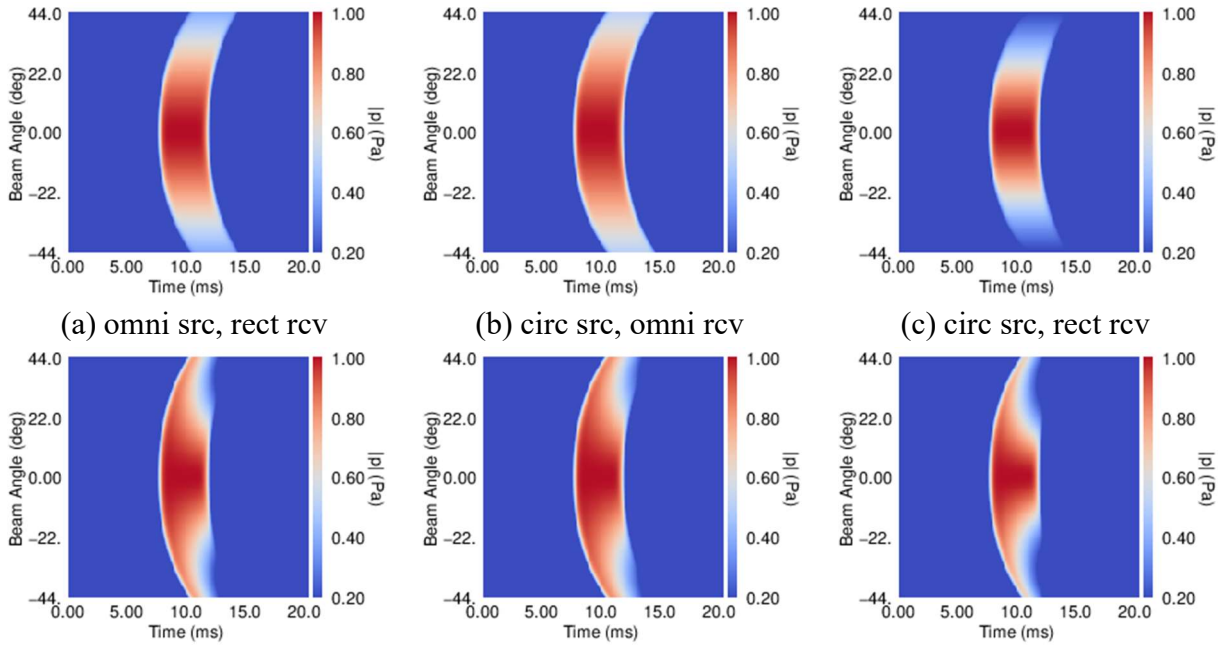

(a) omni src, rect rcv (b) circ src, omni rcv (c) circ src, rect rcv

(d) omni src, rect rcv (e) circ src, omni rcv (f) circ src, rectangular rcv

Figure C2: (a)–(c) Pulse envelops for frequency-independent beam patterns with $k = k_0 \approx 0.64$ m^{-1}. (d)–(f) Pulse envelops for frequency-dependent beam patterns with $0.32 < k < 3.2$ m^{-1}.

In the classification studies of previous SERDP projects (MR-2231 and MR-2505), APL-UW reduced measured SAS data to acoustic color (AC) templates. An AC template is the absolute target strength as a function of a target-centered aspect angle and frequency. Experimental AC templates were constructed from nine measurements where an isolated target was rotated from -80° to 80° in 20° increments. (Note, the axis of symmetry of a cylindrical symmetric object is parallel to the SAS rail for a 0° orientation.) Overlapping partial AC templates of $\pm 25^{\circ}$ at each pose angle were merged, where the central $\pm 20^{\circ}$ range is retained, to generate a full 360° AC template. Simulations have been performed to analyze these experiments. The four-element

source array of Fig. C1 was simulated by a source with a 10×10 cm^2 aperture. The physical receiver had the same dimensions. For fixed-frequency apertures, the magnitude of the pulse-compressed (PC) signals are depicted in Fig. C3(a), and the corresponding SAS image and AC template are shown in Fig. C3(b) and C3(c). The middle row of Fig. C3 are the results when Eq. (C1) is evaluated with its full frequency dependence. The bottom row shows the magnitude of the differences between the top and middle row. The differences in the PC signals and SAS images are nearly 20 dB down. More importantly, over the $\pm 15^{\circ}$ range for the AC template, there is no observed difference down to a -30 dB level.

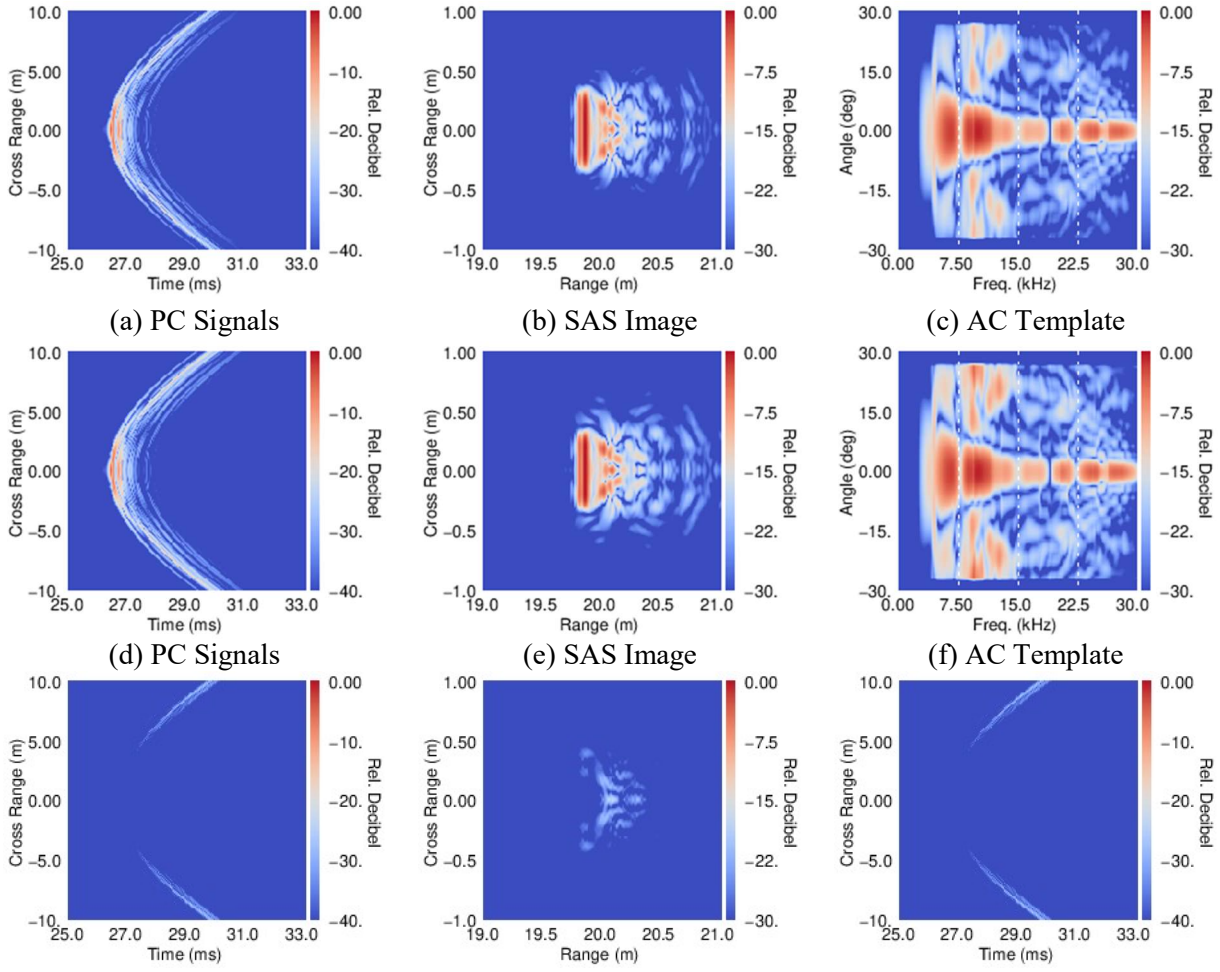

(a) PC Signals (b) SAS Image (c) AC Template

(d) PC Signals (e) SAS Image (f) AC Template

(g) PC Signals (h) SAS Image (i) AC Template

Figure C3: (a) Frequency-independent pulse-compressed signals with frequency of 15 kHz. (b) SAS image generated from time signatures in (a). (c) AC template generated from time signatures in (a). (d) Frequency-dependent pulse-compressed signals with frequency of 15 kHz. (e) SAS image generated from time signatures in (d). (f) AC template generated from time signatures in (d).